Author:
Koorikkat, Aswathi

Title:
Study of Surface Morphology and Microstructure of Electrodeposited Polycrystalline Cu Films

Study of Surface Morphology and Microstructure of Electrodeposited Polycrystalline Cu Films

By

ASWATHI KOORIKKAT

School of Physics
UNIVERSITY OF BRISTOL

A dissertation submitted to the University of Bristol in accordance with the requirements of the degree of DOCTOR OF PHILOSOPHY in the Faculty of Science.

DECEMBER 2022

Word count: 33745

Abstract

The applications of polycrystalline films range from interconnects in the electronics and semiconductor industry to solar cells and as corrosion protection. Despite their significance, factors that determine their microstructure and morphology remain largely unsolved. The surface and microstructure of electrodeposited polycrystalline Cu films were investigated. This involves looking at the later growth stages of Cu films using different surface and bulk characterization techniques.

The surface evolution of an electrodeposited Cu film was imaged in real-time using a High-speed Atomic Force Microscope (HS-AFM). This provides details about how the film structure coarsens with time. The high-resolution video showed accelerated local grain growth and grain overgrowth at different locations of the film. A combination of both of these mechanisms could drive structural coarsening. The microstructure could play a role in inducing faster growth in certain grains. How the local and large-scale roughness varies with film thickness is studied by scaling analysis. As a complement to scaling analysis, variation in the local slope with thickness is calculated using slope analysis. Rapid growth was observed in the regions where the HS-AFM tip was scanning. The removal of oxygen adlayer from the surface by the tip could promote faster growth in these regions.

Pulsed electrodeposition produced Cu films with hexagonal structures. They are known to be twinned which is a desirable feature in applications that require superior mechanical and electrical properties. The effect of electrode potential on grain size was studied. Using a watershed segmentation algorithm, the grain area was calculated from the AFM images. The grain area showed an increasing trend with increasing overpotential. Slope analysis on the 'hexagons' and the complete films electrodeposited at higher potential revealed higher slopes and distinct slope distribution. Cross-sectional Focused Ion Beam (FIB) milling confirmed that horizontal twins are present in the pulse-deposited Cu films. The hexagonal pyramids with twins could be produced by one of the two mechanisms, stress relaxation during the 'OFF' period of pulsing or driven by screw dislocation. We attribute the origin of the hexagons to spiralling screw dislocations.

A template matching algorithm was developed to try and correlate the surface and microstructural data of a Cu film grown on a microelectrode. It involved matching the AFM and Electron Back Scatter Diffraction (EBSD) data on the later FIB milled sample, thus relating surface topography to crystallographic orientation. The crystallographic orientation of the edge of the microelectrode and its centre showed different orientations, switching from (111) to (110). Twinning was investigated at the edge and the centre of the microelectrode revealing the presence of stacking fault twins in both of these regions.

I declare that the work in this dissertation was carried out in accordance with the requirements of the University's Regulations and Code of Practice for Research Degree Programmes and that it has not been submitted for any other academic award. Except where indicated by specific reference in the text, the work is the candidate's own work. Work done in collaboration with, or with the assistance of, others, is indicated as such. Any views expressed in the dissertation are those of the author.

SIGNED: .... DATE: ....

TABLE OF CONTENTS

Page

INTRODUCTION

Polycrystalline films are an essential component for various applications in the electronic and semiconductor industry. They are an integral part of many electronic, magnetic and optical systems and devices. Interconnects in microelectronics connecting components in Printed Circuit Boards (PCBs) are made up of polycrystalline metallic films [1, 2], HDDs (Hard Disk Drives) for data storage using magnetic means and SSDs (Solid State Drives) replacing HDDs contains conductive layers of polycrystalline materials. Solar cells[3], detectors[4] and sensors[4] are some other devices employing polycrystalline materials as essential elements.

The preparation of polycrystalline films can be achieved through different thin film growth techniques. This includes Chemical Vapour Deposition(CVD),[5], Physical Vapour Deposition (PVD)[6, 7], Atomic Layer Epitaxy (ALE)[8], electrodeposition [9, 10] etc. Among these techniques, electrodeposition is a simple process whereby metallic films can be deposited on a substrate from an electrolyte solution by applying a sufficient potential/current. Unlike other techniques, electrodeposition does not utilize a high vacuum environment and it is very cost-effective. There are several parameters that determine the properties of thin films prepared by electrodeposition. Electrode potential[11], electrolyte concentration[11], electrolyte PH[12, 13] and additive concentration[14] are some parameters that can be easily adjusted to prepare thin films of desired properties. Electrodeposition is employed in spintronics to produce multilayers exhibiting Giant
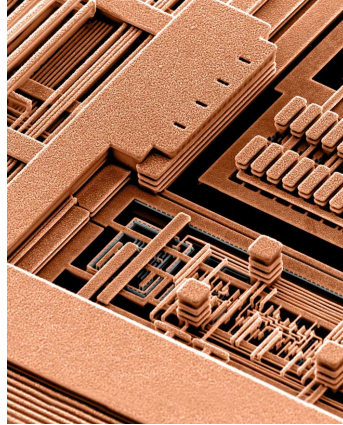
FIGURE 1.1. Cu interconnects fabricated by IBM[18].

Magneto Resistance (GMR)[15]. Electrodeposited coatings are used in the nuclear industry as they form the basis for the Electrosleeve process to repair nuclear steam generator tubing[16]. Because of its high conductivity, Cu has attracted special attention and has been the focus of extensive scientific research. Copper replaced aluminium as interconnects due to its better conductivity and electromigration resistance properties[17]. After the introduction of Cu interconnects by IBM in 1997[18], copper baths containing additives in millimolar to micromolar quantities are used to fabricate interconnects by the damascene process[19, 20]. Each additive plays a different role in the filling of the submicron-sized vias and trenches. PEG in synergy with chloride has an inhibition effect on copper deposition. PEG combines with Cl^- to form an intermediate PEG-Cl^-- Cu^+ that blocks the deposition of Cu outside this submicron features[21]. The curvature-enhanced accelerator coverage (CEAC) model states that the accelerator, for example, SPS [$Na_2(S(CH_2)_3SO_3)_2$] binds more towards the concave sections than the convex segments. This results in the adsorption of accelerators at the junction of the via sidewalls and the bottom region with significant curvature. The deposition rate is proportional to the coverage of these catalytic species. This leads to accelerated deposition there and facilitates the 'bottom-up' filling process[2, 21, 22]. Levelers are used for inhibiting the deposition of copper at the opening of the vias and preventing the formation of bumps at the top of the feature. A commonly used leveler is JCB(Janus Green B)[23].

The challenges in using Cu interconnects include the absence of a passivation oxide layer, which
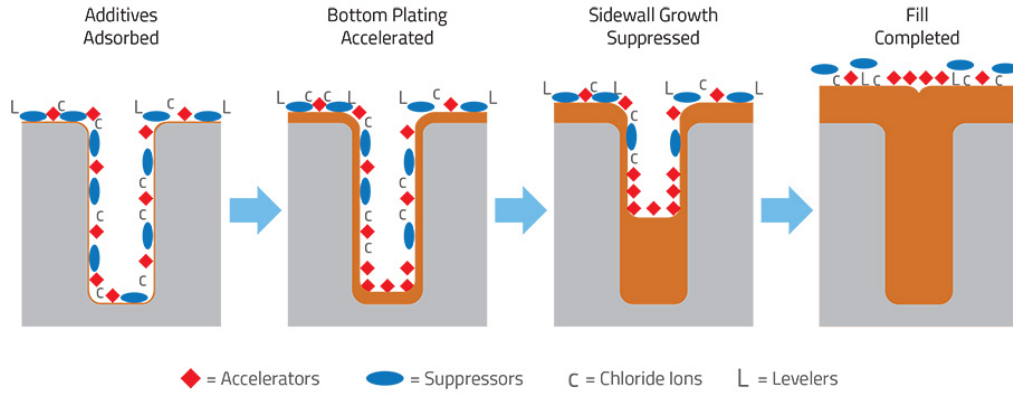
FIGURE 1.2. Schematics of superconformal filling during Cu electroplating in the dual-damascene process[24].

can lead to Cu corrosion or diffusion into Si-based insulating layers. To overcome these problems, new barrier materials like Ta/TaN can be introduced during production [25]. Thin films of graphene [26] or hexagonal boron nitride [27] are barrier layers used to prevent the corrosion of Cu in an electrolyte. Figure 1.1 and 1.2 show copper interconnects and the superconformal filling process involved in the damascene process respectively. Copper is also used for corrosion protection and decorative purposes[28].

The surface morphology and microstructure of a polycrystalline film can influence its mechanical properties like toughness, ductility, and wear resistance. Grain boundaries and other defects can scatter electrons affecting the electrical resistance[29]. The onset of corrosion is known to begin from grain boundaries[30]. Surface features are known to scatter electrons, affecting electron transport, hence the conductivity of a material. Despite their significance, the mechanisms determining the microstructure and surface morphology are still largely unsolved. The main reason for this is that the later stages of polycrystalline film growth are poorly understood owing to a lack of detailed in-situ studies. A polycrystalline film growth proceeds via nucleation, coalescence, coarsening and thickening stages. The previous studies about nucleation during electrocrystallization involved understanding the thermodynamic concepts of heterogeneous nucleation[31]. Avrami discussed the overlapping of the growth centres involved in the process of nucleation and its subsequent growth[32]. Later different growth modes on a foreign substrate were proposed by Stranski and Krastanov[33], Frank, and Vander Merwe[34]. Volmer and Erdey-Gruz formulated

the relationship between supersaturation and overpotential in electrodeposition[35, 36, 37, 38]. They also came up with the relationship between steady-state current density and overpotential for 2D and 3D nucleation[39]. Studies on the problem of surface diffusion, propagation, and dendritic growth of metals were conducted by Bockris, Damjanovic, and Despic[40, 41, 42]. Many studies currently use tools like Transmission Electron Microscope (TEM), Scanning electron microscope (SEM), Atomic force microscope(AFM), and scattering techniques like X-ray diffraction (XRD) and Small-angle X-ray Scattering (SAXS) for direct observation of nucleation and growth[43, 44, 45, 46]. While early stages like nucleation and coalescence[47, 48] are well understood, the later stages remain less explored.

The central aim is to try and understand the evolution of surface morphology of Cu films as well as to study the post-growth microstructure of the electrodeposited films. The surface morphology of the film is heavily dependent on the underlying grain structure, it is impossible to try to account for one without considering the other. Combining both morphology and microstructural information can help us get a clear understanding of how the film evolves. This information is useful to tune the film properties according to their desired application, as well as to understand why certain features or structures form or are dominant during growth. Linking morphological features to the microstructure requires qualitative and quantitative information about both. The topographical information is extracted using state-of-the-art High-Speed AFM (HS-AFM) and conventional AFM, for microstructural measurement Focused Ion Beam (FIB) and Electron Backscatter Scatter Diffraction (EBSD) are used. This thesis is concerned with the study of the morphology and microstructure of copper films at the later stages of growth prepared by electrodeposition from acidic electrolytes.

1.1 Aims of the thesis

A list of the main aims of this thesis is as follows:

- To investigate the morphological evolution of an electrodeposited Cu polycrystalline film using an in-situ real-time surface probing technique.

- To study the influence of electrode potential on the morphology, grain size and crystallographic orientation of pulsed electrodeposited Cu films.

- To develop a technique to correlate the surface topography to the underlying crystallographic orientation of an electrodeposited Cu film.

1.2 Chapter descriptions

Chapter 2 gives the theoretical background of electrochemistry. Sections describing the quantitative descriptive techniques of scaling and slope analysis are also discussed.

Chapter 3 introduces the experimental and characterization techniques used in this work. This includes the working principle of each experimental technique, the preparation of the sample and a description of how data was acquired.

Chapter 4 contains the results from the experiments performed in situ real-time on a Cu electrodeposited film. A microelectrode was used to observe a Cu film using the HS-AFM technique, producing high-resolution images. This chapter also includes a qualitative description of the growth process combined with quantitative scaling and average slope analysis.

Chapter 5 introduces a different electrodeposition technique, pulsed electrodeposition to grow highly twinned Cu films. The pulsed films grown from different electrode potentials are studied. Grain sizes are calculated and compared using a watershed algorithm. Along with average slope analysis of a whole Cu film, local slope analysis on specific surface features is carried out. The textures of the grown Cu films are studied using XRD and EBSD techniques.

Chapter 6 looks at Cu films grown from an electrolyte with a controlled addition of chloride. The AFM images of a Cu film electrodeposited on a microelectrode are attempted to be linked to EBSD information using a template matching process. Crystallographic orientation and twinning are carefully studied for selected grains.

Chapter 7 summarizes all the outcomes of each chapter. Suggestions for future work are given.

THEORETICAL BACKGROUND

T his chapter introduces the theoretical aspect of electrochemistry and gives a brief introduction to thin film formation. This chapter also describes the two quantitative analysis techniques, scaling and slope analysis. These two concepts are used as tools to calculate surface roughness and local slope from AFM images of the Cu films.

Electrochemical studies involve investigating the processes and changes occurring at the electrochemical interface with the application of electrode potential. The electrode\ solution interface, or electrochemical interface, is charged due to the presence of excess charge on the metal surface and an equal and opposite charge on the electrolyte solution side. Changing the electric potential at the interface can transfer charge across this region. Charge transfer usually results in a chemical reaction at the electrode surface.

2.1 Electrochemical cell and electrode reaction

Electrochemical cells are the ideal systems for studying electrochemical reactions. For this, two-electrode or three-electrode cells are commonly used. Apart from working and counter electrodes, the three-electrode cell includes a reference electrode. The applied potential of the working

electrode is always measured with respect to the reference electrode. These reference electrodes are constructed in a way that their composition remains unchanged. The concentration is fixed and their response remains stable over time; hence the changes in the cell are attributable to the working electrode. Silver/Silver chloride Electrode, Standard Hydrogen Electrode (SHE), and Saturated Calomel Electrode (SCE) are some of the commonly used reference electrodes during electrochemical experiments[49]. The overall electrode reaction in the cell is a combination of two half-cell reactions, also called redox reactions. The electron transfer reactions occur at both working and counter electrodes. Usually, the processes happening at the working electrode are of interest. When a negative potential with respect to the equilibrium potential is applied to the working electrode, charge (electrons) can flow from the electrode to the solute species in the electrolyte, generating a cathodic current. The reaction following this charge transfer is called reduction. The general case of a typical reduction reaction of metal M looks like this:

$$M^{n+} + ne- \rightarrow M \tag{2.1}$$

M^{n+} is the oxidant and M is the reductant. n is the stoichiometric number of electrons involved in the reaction. Similarly, applying a positive potential can transfer electrons from the neutral metal to the working electrode, producing a flow of anodic current and the oxidation reaction proceeds. A simple oxidation reaction of a metal M is given by:

$$M \rightarrow M^{n+} + ne- \tag{2.2}$$

The charge flow occurring at the electrode surface is categorized into two types, faradaic and non-faradaic processes. Faraday's law states that the amount of product generated during a chemical reaction is directly proportional to the amount of electricity passed. A reaction involving charge transfer across the interface, which follows Faraday's law, is called a faradaic reaction. Processes, where charge transfer does not occur, are usually referred to as non-faradaic processes. Charging a capacitor, and adsorption of certain species on metal surfaces are a few examples of non-faradaic processes. Measuring the current flow across the interface due to charge transfer is a determination of the rate of a chemical reaction[49].

$$\text{Rate (mols}^{-1}) = \frac{dN}{dt} = \frac{i}{nF} \tag{2.3}$$

where N is $\frac{Q}{nF}$ or the number of moles electrolyzed, Q is the charge passed and F is the Faraday constant F = 96485.4 C. Rate can be expressed in current density $j = \frac{i}{A}$ (current passing per unit area).

$$\text{Rate} \left(\text{mols}^{-1} \text{ cm}^{-2}\right) = \frac{i}{nFA} = \frac{j}{nF} \tag{2.4}$$

2.2 Electrode potential

The potential difference arising at the electrode-electrolyte interface is referred to as the electrode potential, E. It is not possible to measure the absolute value of the electrode potential directly. Instead, a reference electrode is used and the potential difference between the working and reference electrode is recorded as the electrode potential.

In metals, the highest filled energy level is the Fermi level, E_F and in solution species, it is represented as the orbital of the valence electron. Applying a potential can alter the Fermi level of the electrons in the electrode. Depending on the value of the applied potential and the change in the Fermi level, the electrode can lose or gain electrons[50]. This process is represented by figure 2.1. At equilibrium, the cathodic and anodic currents are equal and the potential measured in this state is referred to as the equilibrium potential, E_{eq}. Departure from the equilibrium electrode potential drives either reduction or oxidation. The difference between the electrode potential and equilibrium potential is the overpotential given by[49]:

$$\eta = E - E_{\text{eq}} \tag{2.5}$$

The standard equilibrium potential (standard electrode potential), E^0 is the equilibrium potential of an electrode reaction when all the reaction components are in the standard state (the standard state is 1M concentration for solutions, 1 atm for gases and a temperature at 25°C), measured against the Standard Hydrogen Electrode (SHE)[49, 51]. Nernst equation describes E_{eq} of a given reaction as a function of the relative activities of the species in the solution at equilibrium. The equation is given by [50]:

$$E_{eq} = E^0 - \frac{RT}{nF} \ln \frac{a_R}{a_O} \tag{2.6}$$
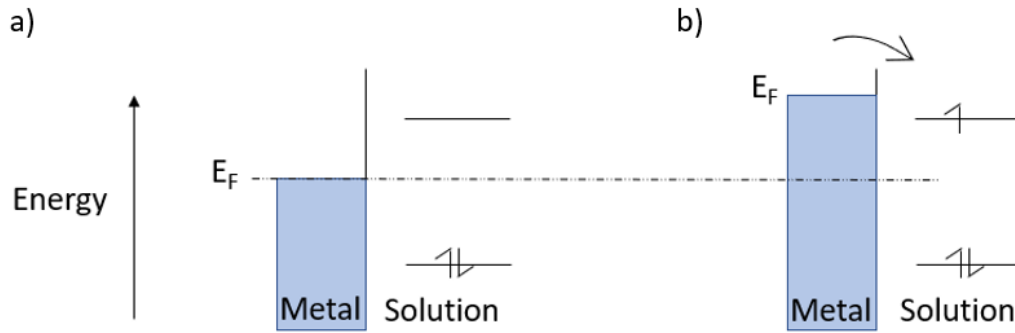
FIGURE 2.1. Energy levels of the electrode and electron transfer a) Electrode potential is insufficient to drive electron transfer from metal to solution b) Electrode potential is driven to a higher value to favour electron transfer. Adapted from [50].

R is the gas constant (8.314 JK-1 mol-1), T is the temperature, a_R and a_O are the activities (or effective concentration of species in non-ideal conditions) of reduced and oxidised species respectively. n is the number of electrons involved in the reaction. The activities are replaced by concentration as activities are almost always unknown[49, 52]. Then E^0 is replaced by $E^{0'}$ called the formal potential. This quantity depends on the specific experimental conditions. Then the Nernst equation is expressed as:

$$E_{eq} = E^{0'} - \frac{RT}{nF} \ln \frac{[\text{ C}_\text{R} \text{ }]}{[\text{ C}_\text{O} \text{ }]} \qquad (2.7)$$

C_R and C_O are the concentrations of the reduced and oxidised species respectively.

2.3 Electrical double layer

At a given potential the electrode\electrolyte interface bears a resemblance to a parallel plate capacitor. This arises due to the accumulation of electrons or holes on the metal electrode side and equal and opposite charges on the solution side. The solution side usually holds either anions or cations distributed close to the electrode surface. The charged species and present dipoles at the electrochemical interface form the electrical double layer, and at a certain potential, it acts as a capacitor. The electrical double-layer model is given in figure 2.2. The inner layer of the double layer is called the Helmholtz, or Stern layer, which is divided into two planes. The
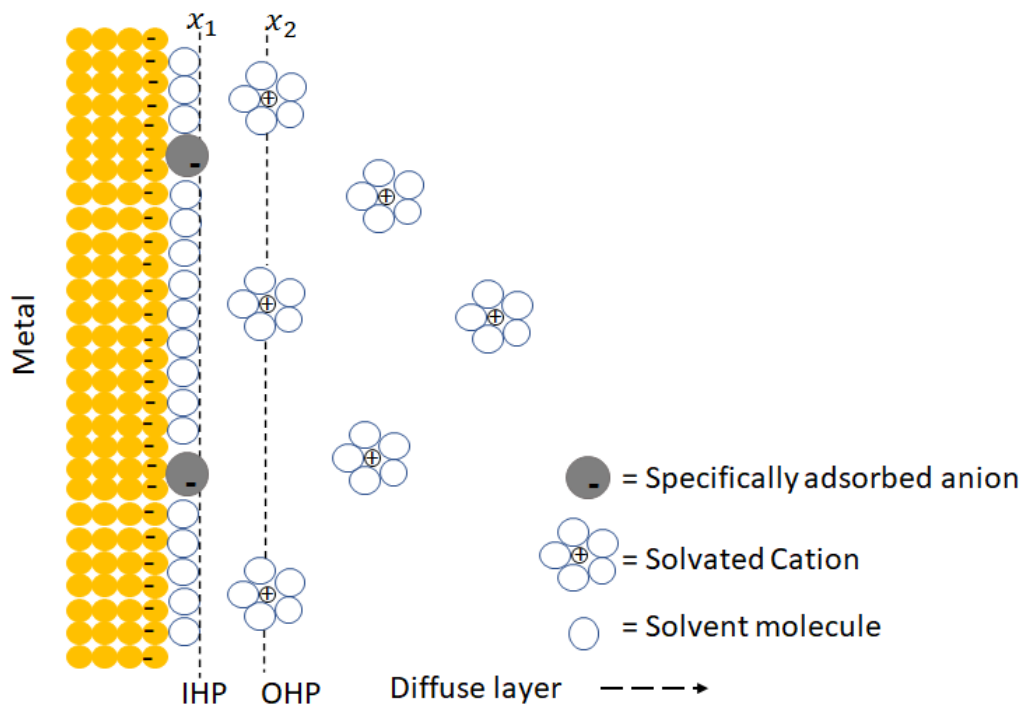
FIGURE 2.2. Model of the electrical double layer at the electrochemical interface with specifically adsorbed anions. x_1, x_2 represents the IHP and OHP planes respectively [49].

Inner Helmholtz Plane (IHP) is at a distance of x_1 from the electrode. Specially adsorbed ions are found in this region. The Outer Helmholtz Plane (OHP) exists at a distance of x_2 from the electrode[49]. This is the region up to which the solvated ions or non-specifically adsorbed ions are able to approach the electrode surface. The non-specifically adsorbed ions are present in a three-dimensional region called a diffusive layer. The diffusive layer stretches from the OHP to the bulk of the solution. A charging current can flow when the double-layer capacitor is being charged. For certain experiments, the charging current contribution is significant compared to the faradaic current passed.

2.4   Mass Transport

To move solute species from one location in the solution to another, three different modes of mass transport are possible.
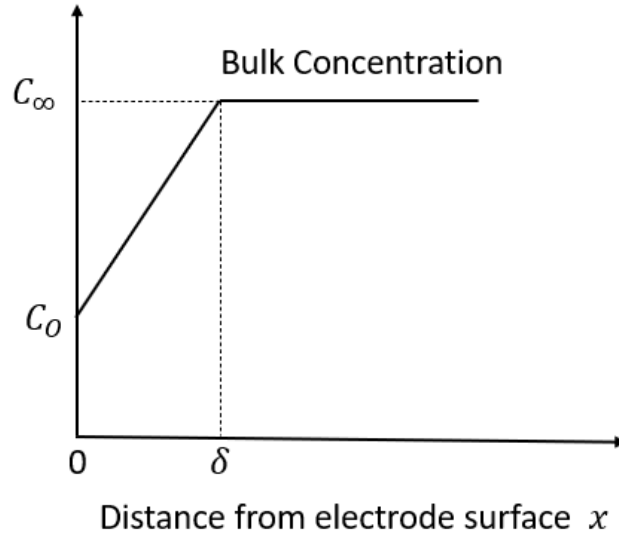
FIGURE 2.3. Concentration profile as a function of distance x from the electrode surface. In reality, there is no discontinuity in the gradient of the concentration.

Diffusion: Diffusion arises as a result of concentration gradients. During the electrodeposition process, the solute species move towards the electrode surface due to the concentration gradient developed at the interface through the depletion of the deposited metal ions. Diffusion is described by Fick's law. In 1D, Fick's law in the x-direction is given by[51]:

$$J_i = -D_i \frac{\partial C_i}{\partial x} \qquad (2.8)$$

J_i is the flux of species i of concentration C_i in the direction x and $\frac{\partial C_i}{\partial x}$ is the concentration gradient. D_i is the diffusion coefficient. A diffusion layer is formed at the close vicinity of the electrode surface as the concentration gradient develops, within the diffusion layer the concentration of the ionic species is different from that of the bulk value. Figure 2.3 shows the concentration gradient as a function of distance from the electrode surface. δ is the diffusion layer thickness.

Let the concentration of species at the electrode surface at $x=0$ be C_0, and the bulk concentration C_∞. If all the species arriving at the electrode surface are reduced, a maximum current will flow. It is equivalent to $C_0 = 0$ ($C_0 \ll C_\infty$, such that $C_\infty - C_0 \approx C_\infty$). This maximum current is called
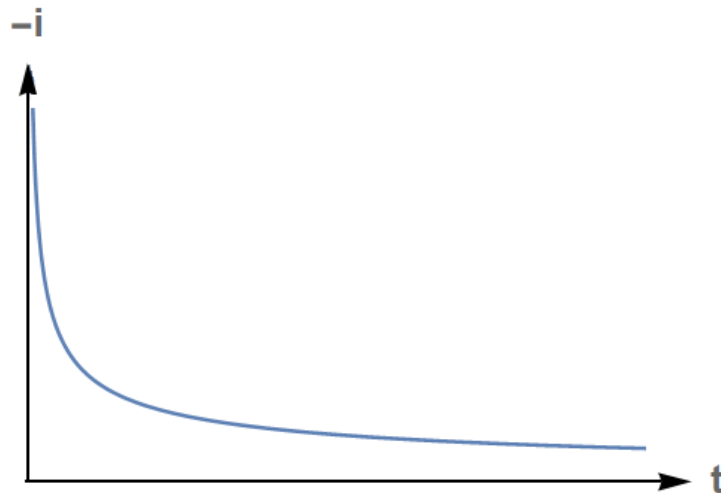
FIGURE 2.4. Current v/s time curve according to Cottrell equation (ref equation 2.10) when the electrode reaction is under diffusion control.

the diffusion-limited current i_l.

$$i_l = nFAm_OC_\infty \tag{2.9}$$

here $m_O = \frac{D}{\delta}$, δ is the thickness of diffuse layer. When i_l flows, mass transport is diffusion-limited. Fick's second law describes the variation of concentration with time due to diffusion and in 1D it is given by,

$$\frac{\partial C}{\partial t} = D_i \frac{\partial^2 C_i}{\partial x^2} \tag{2.10}$$

Solving the second law with proper initial and boundary conditions leads to a current–time response known as the Cottrell equation [49, 51]. For a planar electrode, this is given by:

$$i(t) = i_1(t) = \frac{nFAD_i^{1/2}C_\infty}{\pi^{1/2}t^{1/2}} \tag{2.11}$$

Figure 2.4 shows how the current to a planar electrode varies with time according to eq 2.10 for a reversible redox reaction. If the diffusion is spherical, the Cottrell equation has a spherical term correction[51]. At a spherical electrode of radius r_0 the Cottrell equation takes the form:

$$i_1(t) = nFADC_\infty \left[\frac{1}{(\pi D_i t)^{1/2}} + \frac{1}{r_0} \right] \tag{2.12}$$

There are two limiting cases here:

Small t: At short times, the diffusion layer is much smaller than the electrode radius r_0. To a

solute molecule at the edge of the diffusion layer, the spherical electrode appears like a planar electrode. In equation 2.11 the linear diffusion term dominates. The current behaves as given by equation 2.10. The current decays with time.

Large t: At large times, the current due to the linear diffusion term decay such that the spherical or radial term dominates and a steady state current flows. Unlike conventional spherical electrodes, microelectrodes can reach a steady state without natural convection. The steady-state current i_{ss} is given by:

$$i_{\text{ss}} = \frac{nFADC_\infty}{r_0} \tag{2.13}$$

The steady state is achieved when the electrolysis and diffusion of ions to the electrode surface occur at the same rate.

Migration: Migration affects the movement of charged solute species under the influence of an electric field. The migration-diffusion equation in 1D is,

$$J_i = -D_i\frac{\partial C_i}{\partial x} - z_i C_i D_i \frac{F}{RT}\boldsymbol{E} \tag{2.14}$$

Here $\boldsymbol{E}$ is $\frac{\partial \phi}{\partial x}$, the potential gradient. The second term in the equation represents the migration component. The current in the bulk solution is carried by migration, with diffusional transport occurring near close proximity to the electrode due to the concentration gradient developed as electrolysis proceeds. It is better to eliminate the migrational component ($\frac{\partial \phi}{\partial x}$) to the flux of charged species. This avoids the complicated mathematical treatments of the mass transport equation[49]. To avoid the contribution of migration, a supporting electrolyte with an excess of non-electroactive ions can be added to the electrolyte solution. The supporting electrolyte maintains electrical neutrality in all regions of the electrode-electrolyte interface except at the region adjacent to the electrode[50]. Apart from minimizing the migratory contributions, the supporting electrolyte can increase the conductivity of the solution and hence minimizing the iR drop arising due to the solution resistance. This improves the accurate measurement of the potential of the working electrode.

Convection: Convection can be natural or forced. An example of natural convection is convection created by a density gradient or a thermal gradient. Stirring is an example of forced convection.

Gravity as a driving force is applicable to natural convection. In the case of forced convection, like stirring, the main forces involved are centrifugal and viscous forces. The diffusion-convection equation is given by:

$$J_i = -D_i \frac{\partial C_i}{\partial x} + v(x)\frac{\partial C_i}{\partial x} \qquad (2.15)$$

Equations 2.7,2.13 and 2.14 together form the Nernst-Planck equation for 1-dimensional mass transfer along the x-axis [49].

$$J_i(x) = -D_i \frac{\partial C_i(x)}{\partial x} - \frac{z_i F}{RT}D_i C_i \frac{\partial \phi(x)}{\partial x} + C_i v(x) \qquad (2.16)$$

2.5 Microelectrodes

Microelectrodes/ultramicroelectrodes are characterised by having a size ranging from nanometres to micrometres. Commonly preferred geometries include spherical, disc, line etc. Even though the total current is small, high current densities can be achieved due to its small size. From equation 2.12, if the microelectrode is of a hemispherical geometry, the current at steady state is given by:

$$I = \frac{nFADC_\infty}{r_0} = 2\pi nFr_0DC_\infty \qquad (2.17)$$

$A = 2\pi r_0^2$ is the area of the hemisphere. The high rate of diffusion in microelectrodes creates a high current density that makes the mass transport contribution from convection negligible. In the case of a plane micro disc of radius a, radial diffusion needs to be considered. For large t, the current is numerically equal to that for a hemisphere of radius $r_0 = \frac{2a}{\pi}$, the current due to radial component is,

$$I = 4nFaDC_\infty \qquad (2.18)$$

The notable difference between a hemispherical and planar disc microelectrode is that the current density is not uniform due to the geometry of the hemispherical microelectrode. The advantages of using a microelectrode are several.

1. A double layer that has an equivalent behaviour to a parallel-plate capacitor is formed at the electrode-electrolyte interface as the metal(electrode) comes into contact with the electrolyte solution. The applied potential at the interface will attain the value only when
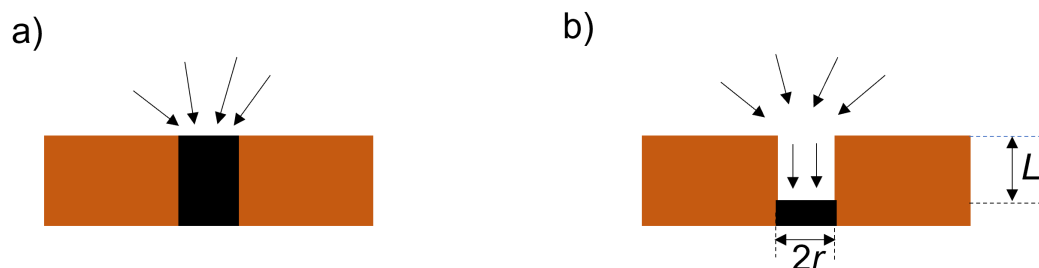
FIGURE 2.5. Diffusion fields at a) an inlaid microdisk electrode b) a recessed microdisk electrode of recess depth L.

the charging of the double layer is complete. Also, at short times, Faradaic and double-layer charging are entwined complicating the electrochemical measurement process. For a microelectrode, the steady state current is attained much faster than for a macroelectrode. Thus double-layer charging does not play a role as the measurements are undertaken in a steady state condition[53].

2. The ohmic drop is an unwanted phenomenon that reduces the applied potential at the WE by an amount of iR, where i is the current and R is the solution resistance. While using solutions of low conductivity, microelectrodes provide the advantage of small iR drops between the working and reference electrodes due to the small current observed.

3. Microelectrodes are ideal systems to perform voltammetry where the electrolyte volume is a few microlitres compared to the electrolyte volumes in millilitres to litres required for a typical electrodeposition experiment on a planar electrode.

4. Microelectrode arrays have many applications in the field of biology and medicine[54]. For example, microelectrodes are used in biological systems as chemical sensors to measure concentrations on the basis of potential changes across chemically selective membranes at their tip[55].

Microelectrodes fabricated by photolithography can be recessed. For an inlaid microdisk electrode, the mass transport is purely radial as shown in figure 2.5a. For a recessed microdisk, the current density is reduced due to the mass transport contribution from linear diffusion within the hole[56]. This is shown in Figure 2.5b.
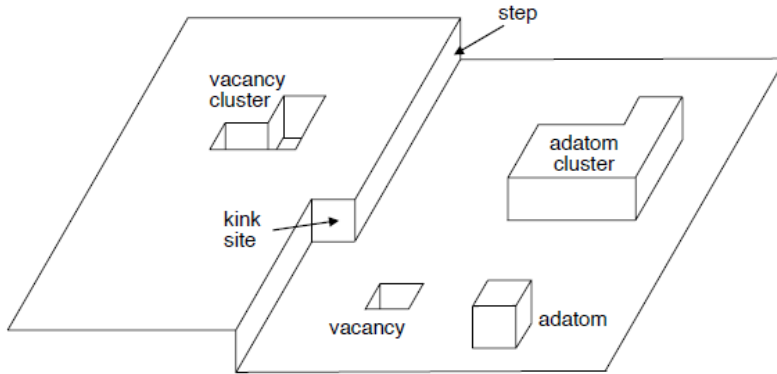
FIGURE 2.6. Different growth sites an adatom can encounter at a metal surface [53].

For a recessed disc electrode, the steady-state current is given by:

$$I_{ss}^{recessed} = \frac{4\pi n F C_\infty D r^2}{4L + \pi r}$$

(2.19)

The steady-state current depends on the recess depth L and opening radius r [57].

2.6   Thin film formation

2.6.1   Surface diffusion

A monovalent cation undergoing charge transfer in the vicinity of the metal electrode surface loses water molecules from its hydration shell and attaches itself to the electrode. The partially dehydrated metal ions are referred to as adions. These adsorbed species are mobile, randomly migrating along the electrode surface until they encounter a growth site where they lose their remaining hydration sheath and get incorporated into the metal lattice. Figure 2.6 shows different types of growth sites present on the metal surface. A kink can be considered an ideal growth site. The atom that is no longer an adion at a kink site would be surrounded by half of the number of atomic neighbours compared to the atom at the bulk of the metal. For that reason, a kink site can be called a half-crystal position. Metal deposition can take two pathways: adion formation or direct transfer of ions into growth sites. A combination of both could take place during metal deposition.

2.6.2 Nucleation and different growth modes

In the case of electrodeposition occurring on a foreign substrate. There are three types of growth modes[58, 53]. These modes are represented in figure 2.7.

Volmer-Weber type growth:

The adhesion energy or the interaction energy U for Volmer-Weber type growth or three-dimensional island growth is U(S-M) < U(M-M). S and M are substrate and metal deposit atoms respectively. For Volmer-Weber growth three-dimensional nucleation takes place. Further growth proceeds via the coalescence of the nucleated clusters and hence a continuous deposit is formed. Volmer - Weber growth is typically observed at high overpotential[53].

Two further important growth modes are observed. Stansky-Krastanov and Frank-Van-der-Merwe type growth.

Stansky-Krastanov type growth:

For Stansky-Krastanov type growth, the adhesion energy is U(S-M) > U(M-M). This type of growth forms a monoatomic layer on the substrate. On top of the first layer, new islands form and grow. Often the mismatch between the lattice of the deposit and substrate can cause the first layer to have an incommensurate structure. The stress generated by the misfit is relaxed as new atomic layers grow, finally reaching a relaxed state.

Frank-Van-der-Merwe type growth:

The relative misfit between the lattice of substrate and deposit is minimal. U(S-M) > U(M-M) and heteroepitaxial growth is observed.

The real substrate possesses active sites, where nucleation is favoured. For an electrode of unit surface area, by first-order kinetics

$$M(t) = M_0 \left[1 - \exp(-k_N t)\right] \tag{2.20}$$
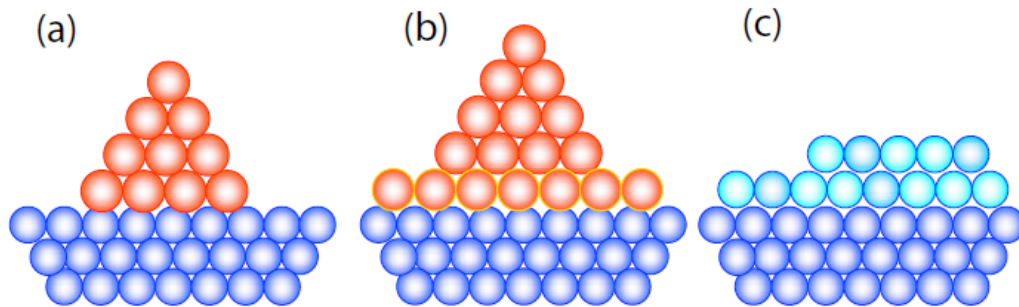
FIGURE 2.7. Different growth modes a) Volmer-Weber growth (island-like growth) b) Stranski-Krastanov growth c) Frank-Van-der-Merwe growth[53].

Here $M(t)$ is the number of growing nuclei, M_0 is the active sites and $k_N t$ is the rate constant for the formation of the nucleus. Two limiting case arises here.

1. $k_N t \gg 1$: represents instantaneous nucleation.

$$M(t) = M_0 \qquad (2.21)$$

2. $k_N t \ll 1$: represents progressive nucleation.

$$M(t) = k_N M_0 t \qquad (2.22)$$

In case 1, all the active sites are occupied by nuclei in a short period of time.

In case 2, the number of nuclei evolves during the observation period. i.e., the number of nuclei is smaller than the active sites. During progressive nucleation, new nuclei are created on the foreign substrate and also on the previously existing nuclei during the deposition process[59].

The nucleation phenomenon is described by different mathematical models. The widely used Sharifker-Hills (SH) model for 3D-nucleation studies the current density-time transients of potentiostatic deposition of metals[60]. The SH model considers diffusion-limited growth and assumes the nucleus formed on the electrode is hemispherical in shape. In this model, instantaneous and progressive nucleations are the two limiting nucleation mechanisms deduced from the current density-time transients. The treatment of the transients considers current density and time in non-dimensional forms $(i/i_{max})^2$ and (t/t_{max}) respectively. Here i_{max} is the maximum current density and time t_{max} corresponds to i_{max}. The relationship between current density and time for instantaneous and progressive nucleation respectively is given by[60]:
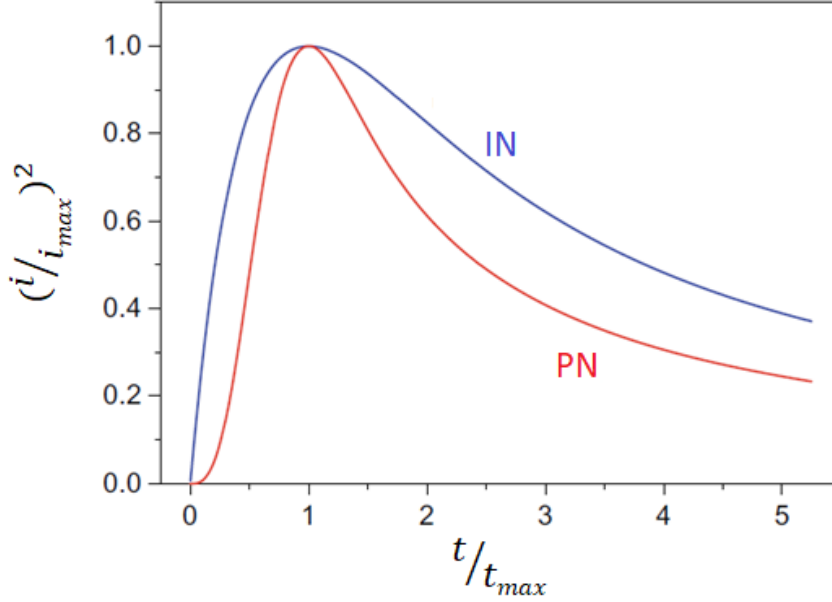
FIGURE 2.8. Current density-time transients for instantaneous nucleation (IN) and progressive nucleation (PN), if the deposition is under diffusion-limited conditions[58].

$$\left(\frac{I}{I_{\max}}\right)^2 = \frac{1.9542}{\left(\frac{t}{t_{\max}}\right)}\left[1 - \exp\left(-1.2564\left(\frac{t}{t_{\max}}\right)\right)\right]^2 \tag{2.23}$$

$$\left(\frac{I}{I_{\max}}\right)^2 = \frac{1.2254}{\left(\frac{t}{t_{\max}}\right)}\left[1 - \exp\left(-2.3367\left(\frac{t}{t_{\max}}\right)^2\right)\right]^2 \tag{2.24}$$

The transients for instantaneous and progressive nucleation according to the theoretical model are shown in figure 2.8.

By comparing the experimental plots to the theoretical plots given in figure 2.8, the nature of nucleation can be predicted as either instantaneous or progressive or follows both. Kinetic parameters like diffusion coefficient and density of active sites can be calculated from the nucleation model data[61].

Several studies have observed experimental data deviating from the SH model[12, 62, 63]. This deviation could be due to the nucleus shape deviating from the hemispherical form, which was

one of the assumptions made by the SH model[64]. Other factors include the kinetics of deposition being under mixed control or due to complexities during the kinetics of deposition [65, 66, 67]. The SH model provides qualitative information about the nucleation process. For quantitative analysis fitting the current density-time transient is necessary which was done by Heerman and Tarallo. The Mirkin-Nilov and Heerman-Tarallo (MNHT) model was one of the models introduced to improve the SH model[68].

2.6.3 Microstructure development

When deposition proceeds, atoms arrive at the surface of the substrate and undergo the process described in section 2.6.1. When a stable cluster of adatoms is formed and they continue to grow nucleation occurs. This stable cluster must reach a critical nuclei size n^* in order to grow without dissolving back to a smaller cluster or to a single adatom. Then the nuclei formed on the foreign substrate surface grow into islands. The islands are surrounded by spherical diffusion zones, which are the areas of the substrate surface from which the adatoms get added to the islands. The zones from which ions diffuse in the electrolyte are spherical, and the zones from which adions diffuse on the surface are circular. As the growth proceeds the diffusion zones overlap. As they overlap, the spherical shapes take a planar form. As the islands grow into points of contact, an energetic driving force promotes the formation of grain boundary, eliminating the surface free energies $2\gamma_f$ and is replaced by a lower grain boundary energy γ_{gb}. This happens by elastic distortion of islands as they coalesce through grain boundary formation. GB energy is the excess energy arising from the misfit of atoms across the GB. According to Mullins,[69] $2\gamma_f$ is the work done for the creation of two free surfaces. $2\gamma_f$ is higher than the γ_{gb} due to the binding energy (B) attained during forming of bonds as two surfaces come together creating a GB. The GB energy is then given by the following expression[70]:

$$\gamma_{gb} = 2\gamma_f - B \tag{2.25}$$

 After coalescence, through the motion of grain boundaries, a process called coarsening commences. Figure 2.9 shows the nucleation, coalesce and coarsening stage of islands. During coarsening small grains are eliminated and the average size of the remaining grains increases reducing
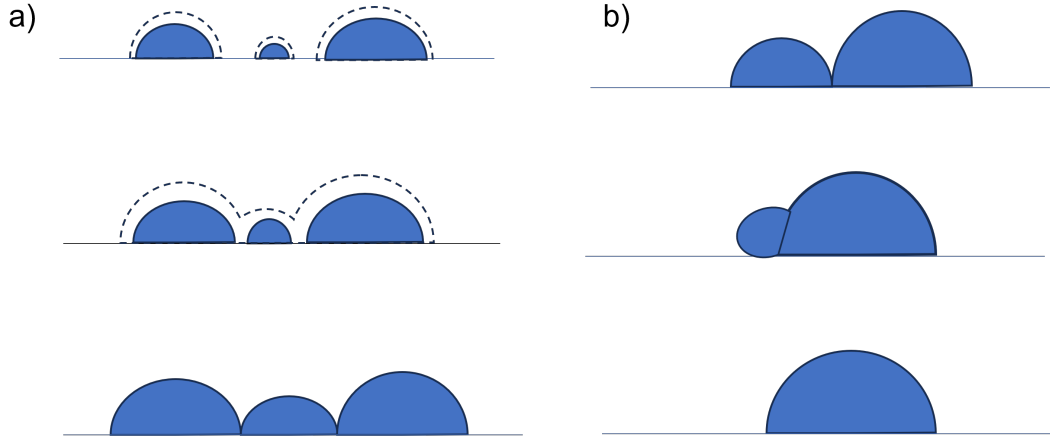
FIGURE 2.9. a) Grains are surrounded by diffusion zones (dashed lines) that overlap as the grains grow in size. Grains with spherical zones transform into a planar geometry with the increase in grain size b) The coalesced islands coarsen by shrinkage and disappearance of certain grains.

the total grain boundary energy. This phenomenon is referred to as grain growth. During the growth process, a dominant texture of the film emerges due to surface and interface energy minimization. This leads to a preferred crystallographic orientation in polycrystalline films. Grains in polycrystalline films are under intrinsic or extrinsic stresses. The crystallographic texture is also determined by strain energy minimization [48].

2.7 Scaling Analysis

Roughness can arise during the addition or removal of materials from the surface. It is known to affect electron transport by scattering electrons from certain features on the surface. Roughness can also obstruct domain wall movement, affecting the magnetic behaviour of materials[71, 72]. Hence roughness is a property that needs to be tuned for different ranges of applications. Scaling analysis serves as a standard tool to understand growing surfaces. Here scaling analysis is used to study the roughness of electrodeposited Cu films.

Roughness is a quantity that is known to depend on the length scale over which it is measured. Figure 2.10 demonstrates the dependence of roughness on the length scale. As illustrated in figure 2.10, at length scale l_1, roughness is w_1 and for length scale l_2, roughness changes to w_2.
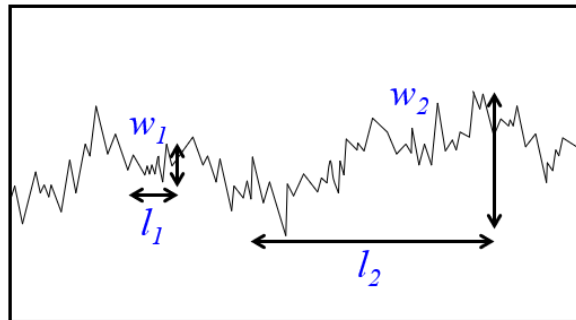
FIGURE 2.10. Surface roughness measured over different length scales[73].

It is possible to measure the surface width $w(l)$, a quantity which is an experimental measure of roughness. Surface width $w(l)$ is defined as:

$$w(l) = \sqrt{\left\langle (h - \langle h \rangle)^2 \right\rangle} \tag{2.26}$$

Here $w(l)$ is the root mean square deviation of the surface height h from its mean value $< h >$. l is the length scale over which w is measured. w can be measured as a function of thickness t or the deposition time for a constant deposition rate.

2.7.1 Normal Scaling

For a film exhibiting normal(Family-Vicsek) dynamic scaling [74] , the roughness measured as a function of t is given by[73]:

$$
\begin{aligned}
w(l,t) &\propto l^H \quad \text{for } l \ll l_{\text{c}} \\
w(l,t) &\propto t^\beta \quad \text{for } l \gg l_{\text{c}}
\end{aligned}
\tag{2.27}
$$

where,

$$l_{\text{c}} \propto t^{1/z} \tag{2.28}$$

For consistency,

$$z = H/\beta \tag{2.29}$$

H is called Hurst exponent, l_c is the cross over length and β is the growth exponent. β predicts how fast the surface becomes rougher. The higher the value of β, the faster the surface will become rough. Figure 2.11 shows a log w v/s log l plot illustrating normal scaling behaviour for a
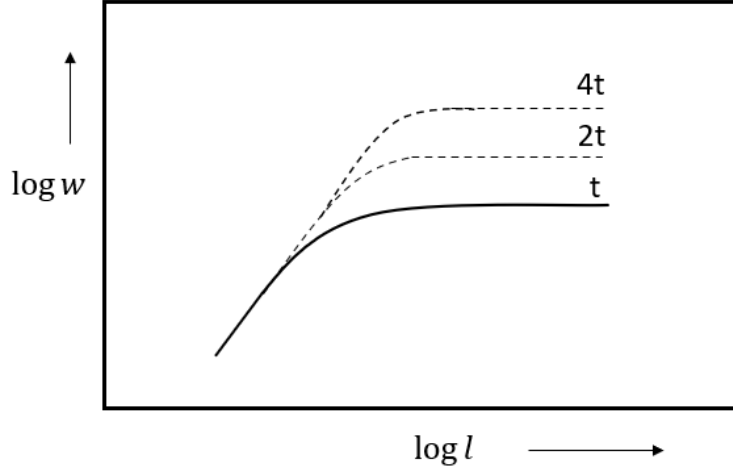
FIGURE 2.11. Logarithmic plot of surface width w v/s the length scale l over which the roughness is measured. The films exhibit normal scaling behaviour at different average thicknesses t,2t and 4t [73].

film at different average thicknesses t. Normal scaling has been reported in numerous systems including Fe [75] and evaporated Ag [76].

2.7.2 Anomalous scaling

Anomalous scaling postulates that $w(l,t)$ obeys a power law in the following form[77, 78]:

$$
\begin{aligned}
w(l,t) &\propto l^H t^{\beta_{\text{loc}}} \quad \text{for } l \ll l_{\text{c}} \\
w(l,t) &\propto t^{\beta+\beta_{\text{loc}}} \quad \text{for } l \gg l_{\text{c}}
\end{aligned}
\tag{2.30}
$$

Here, the new exponent β_{loc} is called the local growth exponent as it measures how local roughness changes with film thickness. Comparing equations 2.22 and 2.25, it is clear that normal scaling is a unique case of anomalous scaling with β_{loc}=0. Figure 2.12 represents anomalous scaling behaviour. The roughness exponent α is defined by:

$$
w_{\text{sat}} \propto l_{\text{c}}^{\alpha}
\tag{2.31}
$$

From equations 2.23,2.24 and 2.25:

$$
\alpha = H\left(1 + \beta_{\text{loc}}/\beta\right)
\tag{2.32}
$$
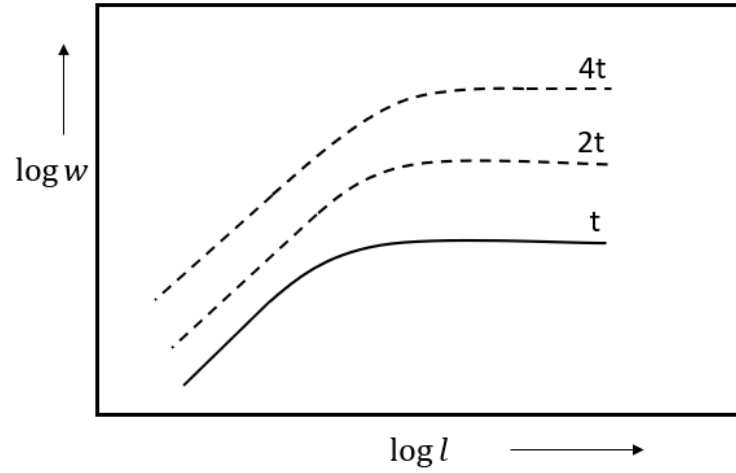
FIGURE 2.12. Logarithmic plot of surface width w v/s the length scale l over which the roughness is measured. The films exhibit anomalous scaling behaviour at different average thicknesses t,2t and 4t[73].
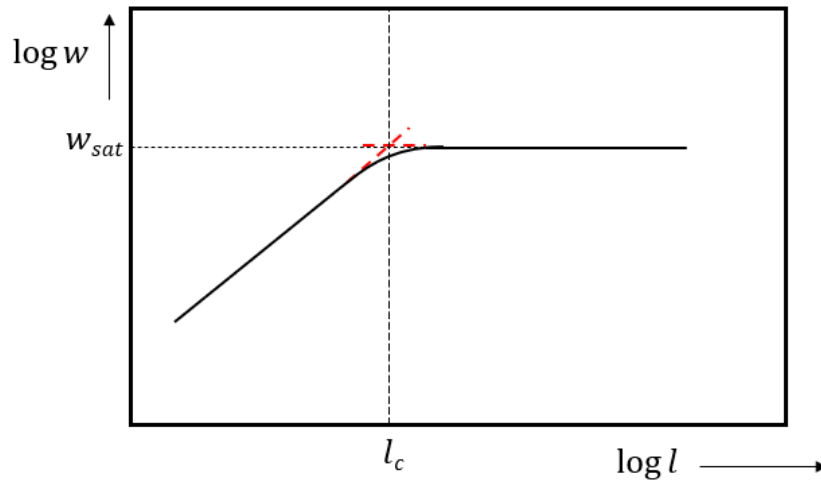
FIGURE 2.13. Logarithmic plot of the surface width w as a function of time t. Roughness saturates at w_{sat} for a length scale larger than cross-over length l_c [73].

In the case of normal scaling β_{loc}=0, implying α is equal to H. Figure 2.13 shows an example of the log w v/s log l curve of a single roughness scaling data. This curve can be divided into two regions. The first region is where the gradient is positive and the second region is where w saturates to a value w_{sat} with zero gradients. $l=l_c$ is called the cross-over length where the

transition between constant slope and constant w takes place. l_c depends on the feature size. As the surface structure coarsens, l_c must change.

Anomalous scaling behaviour is observed in a variety of systems, such as biological samples [79], metal films [80] and vapour-deposited polymer films [81].

2.8 Slope Analysis

For characterising the surface morphology of a thin film, it is possible to calculate the local slope θ from an AFM image [82]. In this thesis, the slope θ is defined to as the angle between the local surface normal and the film normal. AFM data, unlike SEM data, consists of surface height information (z_{ij}). Corresponding to the height $z_{i,j}$ values are the x and y coordinates $x_{i,j}$ and $y_{i,j}$ respectively. For a point on the AFM image $(x_{i,j}, y_{i,j}, z_{i,j})$, there are four neighbouring data points. Linking two neighbouring points, for example $(x_{i,j+1}, y_{i,j+1}, z_{i,j+1})$ and $(x_{i-1,j}, y_{i-1,j}, z_{i-1,j})$ to this point defines a plane. Four such planes can be constructed by linking all the immediate neighbouring points to $(x_{i,j}, y_{i,j}, z_{i,j})$. Figure 2.14 shows such a construction of four triangles generated by linking a data point to its neighbours. The angle between the normal to the triangle and the z-axis can be calculated using equation [82]:

$$\cos\theta_A(i,j) = \Delta l / \sqrt{\Delta l^2 + \left(z_{i-1,j} - z_{i,j}\right)^2 + \left(z_{i,j+1} - z_{i,j}\right)^2} \tag{2.33}$$

Here Δl is the pixel size (scan area/number of pixels) and θ_A the angle between the z-axis and the normal to the triangle marked A. All slopes θ of the remaining triangles can be calculated similarly.
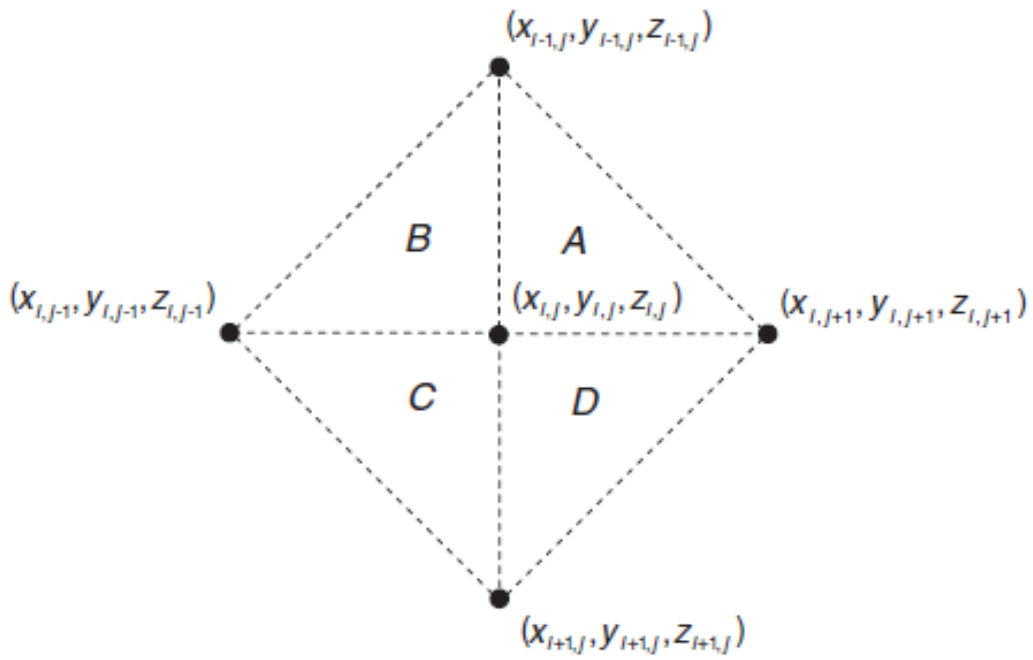
FIGURE 2.14. Illustration of the four triangles (A, B, C and D) constructed around the data point (x_{ij}, y_{ij}, z_{ij}) to calculate local slope θ [82].

Experimental Techniques: Principle and setup

I n this chapter, a description of the experimental methods used in the thesis to analyse Cu films is introduced. The experiments include electrochemical studies and morphological and microstructural characterization techniques. Electrochemical studies were performed using two methods, cyclic voltammetry and chronoamperometry. The concepts are briefly explained. Characterization involves looking at the surface, which is the topography and then looking at the bulk of the material, which is the microstructure. For the study of topography, AFM, HS-AFM and SEM were used. Their principle and setup are given. For microstructural data, FIB, EBSD and XRD were utilized. Their experimental details are also given here.

3.1   Electrochemical cell setup

Electrodeposition was carried out in an electrochemical cell setup. A typical cell consists of three components, a working electrode (WE), a reference electrode(RE) and a counter electrode(CE). The electrochemical cell is connected to a potentiostat which is capable of applying a potential or current. The working electrode for copper electrodeposition was gold deposited onto a non-conducting glass/silicon substrate. The gold coating was prepared in a thermal evaporator kept at a base pressure of 2×10^{-6} Pa and the thickness of the deposited Au was 200nm. Before depositing
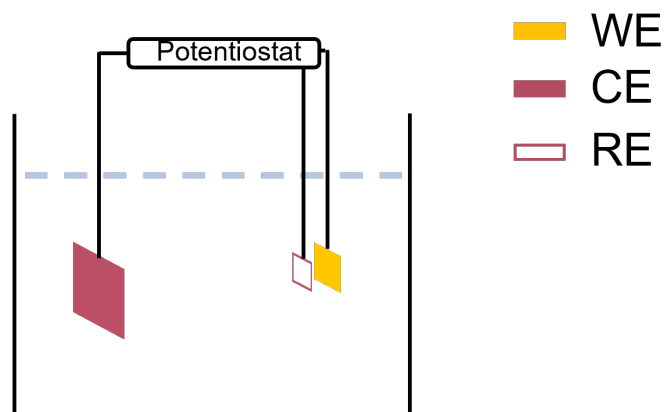
FIGURE 3.1. Diagram of electrochemical set-up. WE is the working electrode, CE is the counter electrode and RE is the reference electrode.

the Au, an adhesive layer of Titanium of thickness $\approx$2nm was deposited on top of the glass/silicon substrate. Strips of copper acted as both RE and CE. Special attention was given to ensure that the reference electrode was kept close to the WE surface to minimize the iR drop arising as the current i passes between the electrodes in an electrolytic solution of resistance R. iR or voltage drop can decrease the effective potential applied across the electrode-electrolyte interface. CE was placed parallel to the WE, with its area much larger than the WE to minimize polarization at the counter electrode. If reduction proceeds at WE, oxidation occurs at CE and vice-versa. The cell setup used for electrodeposition is given in figure 3.1.

3.2 Cyclic voltammetry

Cyclic voltammetry or CV is an electrochemical technique used to investigate the redox properties of a particular electrochemical species. Typically while performing a CV, the potential of the working electrode is cycled between the initial electrode potential and the final potential and the corresponding current is measured. The sweep is reversed upon reaching the final potential.

In Figure 3.2a, for a planar electrode, a forward scan towards positive potential results in an anodic current to flow, indicating the oxidation of the solute species. Then, as the potential is swept to a negative value, a cathodic current flows due to the solute species undergoing reduction. Figure 3.2b for a microelectrode shows that the anodic and cathodic currents reach a limiting value,
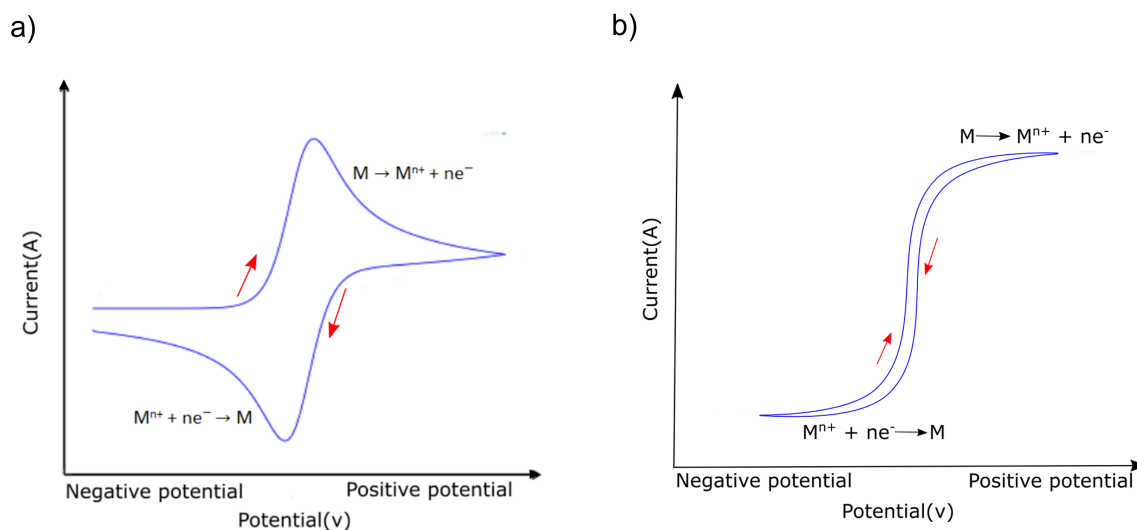
FIGURE 3.2. Cyclic voltammogram of a fully reversible reaction of a solute undergoing a simple electrochemical transition a) CV of a planar electrode b) CV of a microelectrode. The cathodic and anodic current peaks are absent in the sigmoid curve.

and the peak currents observed in a planar electrode are absent in the CV of the microelectrode. This electrochemical behaviour of microelectrode is due to enhanced mass transport by radial or spherical diffusion towards the electrode, driving the current to a time-independent steady-state value.

The CVs in Figure 3.2 involve both the reactant and product in solute form. However, when considering metal deposition on a foreign substrate and its dissolution, the obtained CV is different. Figure 3.3 corresponds to the CVs of the metal deposition and dissolution process on a planar and a microelectrode. From Figure 3.3a, the cathodic current starts to flow when the potential is moved away from the equilibrium potential value and reaches a peak value of I_c, indicating metal deposition. After the peak, the current plateaus as the deposition takes place in a diffusion-controlled regime. Upon reversing the cathodic current decreases. As the sweep continues, after passing 0, the anodic current reaches a peak value of I_a. After that, the current decreases and reaches 0, indicating the completion of the oxidation process. The peaks during metal deposition and dissolution are well separated compared to a reversible redox reaction. The CV produced during the deposition and dissolution of a metal on a microelectrode is shown in Figure 3.3b. The current reaches a limiting value upon the reduction of metal ions. The metal
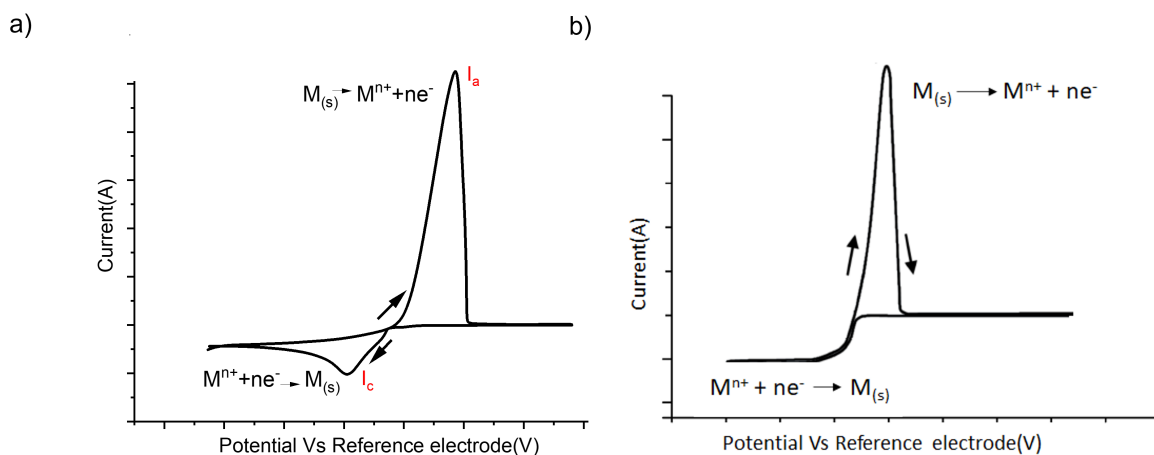
FIGURE 3.3. Cyclic voltammograms of metal deposition and dissolution a) CV of a planar electrode b) CV of a microelectrode [83].

dissolution peak can be seen upon sweep reversal.

The scan rate controls how fast the applied potential sweep is scanned. The scan rate has a profound effect on the thickness of the diffusion layer. The higher the scan rate, the smaller the thickness of the diffusion layer and the higher the current observed. Randles-Sevcik equation for a reversible reaction shows how peak current i_{pc} increases with the square root of the scan rate v (V/s) linearly. This equation considers planar diffusion and is given as [52, 84]:

$$i_{pc} = 0.446nFAC_{\infty} \left(\frac{nFvD_i}{RT} \right)^{1/2} \tag{3.1}$$

where n is the number of electrons transferred in the redox event. A is the geometric surface area, D_i is the diffusion coefficient of species i and C_{∞} is the bulk concentration of the analyte.

Chronoamperometry or CA is a potential step technique where the potential of the WE is changed to a fixed value away from equilibrium potential such that a current flows. Figure 3.4 shows the potential step and the response of the system. During CA, the current-time response of a soluble redox species under diffusion control is recorded as shown in figure 3.4b.

The CA represents the I-t behaviour when reactants and products are soluble in the solution. While considering phase change, e.g. metal deposition, the system exhibits an I-t transient shown in Figure 3.5. The rising portion in the current is due to the involvement of nucleation.
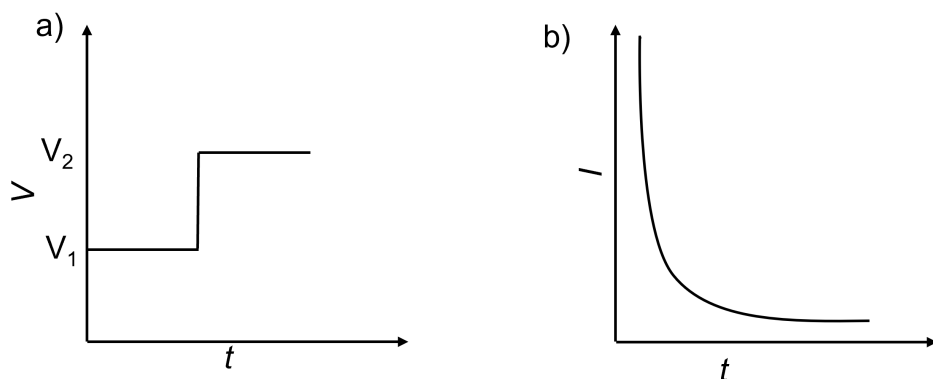
FIGURE 3.4. a) Potential response of stepping the potential from V_1 to a higher potential V_2 b) Current response of a soluble redox species if the potential V_2 value is chosen to be under diffusion control.
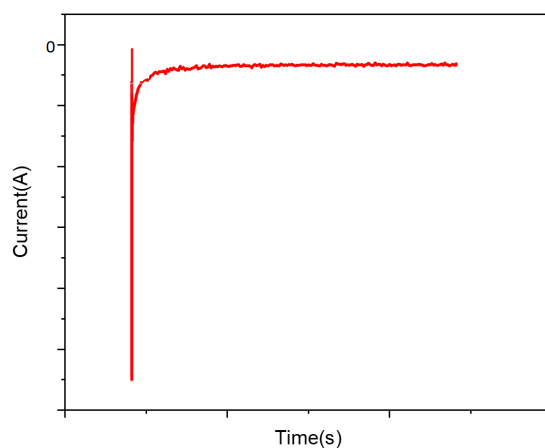
FIGURE 3.5. Current transient response during metal deposition. The potential is switched to a higher value away from the equilibrium potential where deposition occurs.

In this work, all the Cu films are electrodeposited using the CA technique using a Biologic potentiostat, modal SP-150.

3.3 Photolithography

Microelectrodes are the best systems for experiments performed using the High-Speed AFM technique. During HS-AFM measurement, the same area of the gold substrate is imaged during
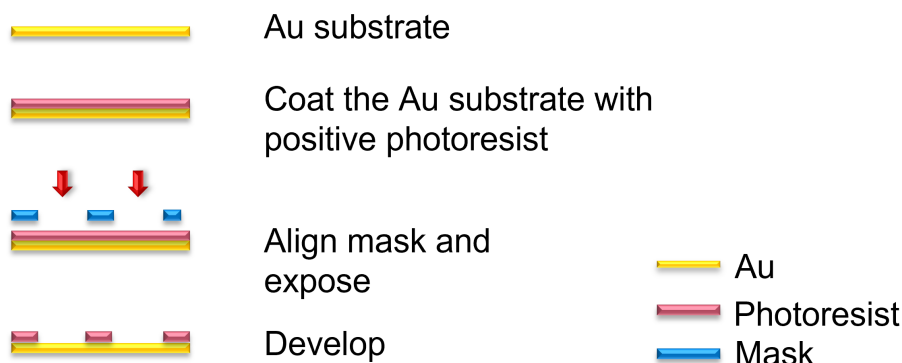
FIGURE 3.6. Schematics of the process during photolithography technique.

the electrodeposition process, to observe the real-time evolution of the Cu film surface. This experiment requires a small area to be imaged. In our experiment, the probe of the HS-AFM was immersed in the electrolyte solution. The liquid forms a meniscus between the probe and the substrate surface. The electrolyte must be contained without spilling over the electrochemical cell. For imaging a small Cu deposited area and to prevent the electrolyte from spilling, a small volume of electrolyte must be used. As discussed in section 2.5, microelectrodes are ideal when electrolytes in small volumes are present. Microelectrodes also give the flexibility of using a two-electrode system for the electrodeposition process as the current observed in microelectrode is small. Fabrication of these microelectrodes was carried out using photolithography patterning. In photolithography, the desired pattern, in this case, a microelectrode of diameter 30μm can be transferred onto the substrate by exposing the microelectrode bearing a hard mask to a UV emitting light source. We used gold of thickness 200nm evaporated onto the glass as the substrate, and for patterning, a positive photoresist S1805 was used. Figure 3.6 shows the schematics of the process involved in lithography. The photoresist was spin-coated evenly on the Au surface followed by baking for 1 minute at 115^0C. A mask aligner from MIDAS was used to produce patterned samples. The hard mask containing the desired pattern is placed in close proximity to the photoresist. The resist is then exposed to UV light, emanating from a UV lamp (energy = 150mJ). The UV-exposed photoresist is then developed using a solvent called the developer (MF-319) for a minute. The developer strips away the exposed region of the photoresist, leaving behind the desired pattern.

Au substrate

Deposit SiO$_2$ on the Au substrate

Coat with positive photoresist

Expose

Develop

Au
SiO$_2$
Photoresist

Etch
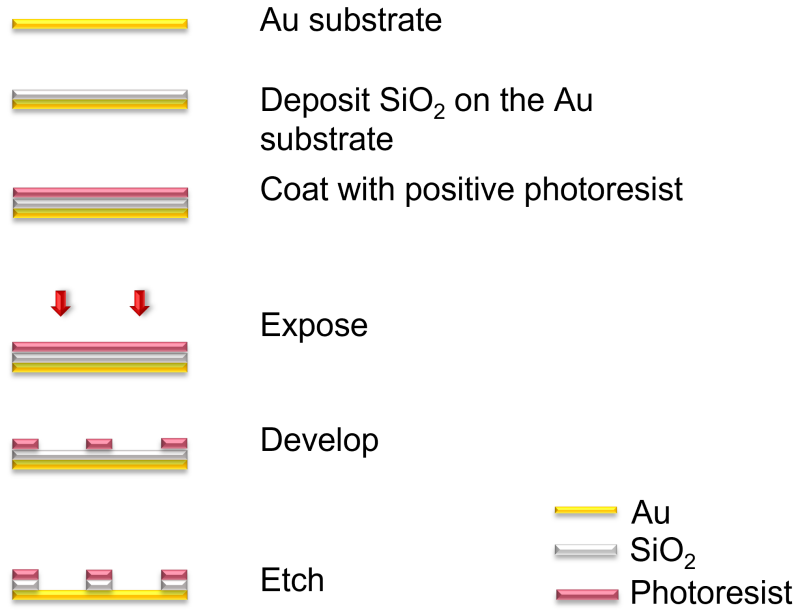
FIGURE 3.7. Schematics of the process during mask-less lithography technique.

3.4 Mask-less lithography: Laser-Writer

Mask-less lithography or direct-write lithography is very similar to photo-lithography, the main difference being that in mask-less lithography a digital pattern file is utilised, and designed by the user in a special software called Klayout. The laser is scanned across the sample to only illuminate those regions specified in a digital pattern file, and the resist is removed from the illuminated regions following the same principles as standard photolithography. The advantage of using mask-less lithography is that it is easy to design or redesign a new digital mask at our convenience, whereas, with a hard mask, the designs need to be patterned in chrome and on a quartz plate. The hard mask was purchased commercially from Compugraphics. Here μPG 101 model laser writer from Heidelberg instruments was used to pattern microelectrodes of size 50μm with photoresist as thick as 1μm. Figure 3.7 shows the schematics of mask-less lithography. Gold of 200nm thickness was evaporated onto a silicon wafer using a thermal evaporator. By using PECVD (Plasma Enhanced Chemical Vapour Deposition) 200nm of SiO$_2$ was deposited onto the gold. On top of the SiO$_2$ layer, S1813 positive resist was spin-coated. After illumination, this is developed using MF-319 developer to strip the exposed region of the resist, which leaves

behind the desired pattern, a microelectrode in this case. The next step is to etch away the non-conductive SiO_2 from the microelectrode surface. For etching the SiO_2, BOE (Buffered Oxide Etch) was used. It has an etch rate of 30-80 nm/min for SiO_2. Keeping the SiO_2 in BOE removes the non-conductive layer from the surface leaving behind the gold microelectrode surface.

3.5   Atomic Force Microscope

Atomic Force Microscopy or AFM is a scanning probe technique used to image the sample surface on an atomic scale. For an AFM, the probe is a cantilever\tip assembly. The probe is made of silicon or silicon-nitride and the tip is usually a few nanometers in diameter. Figure 3.8 shows the schematics of the functioning of the AFM and probe. The probe scans over the surface of the sample in a raster pattern. A laser beam is reflected off of the top of the cantilever and this beam monitors the vertical as well as the lateral motion of the tip as it scans along the sample surface. The reflected beam is detected by a position-sensitive photodetector. There are several modes of operation in AFM. Contact mode and tapping mode are two of the common ones used to extract topographic information. The AFM operates using a feedback loop. Depending on the mode, the AFM will consider a certain parameter as the set point (desired value).

In contact mode, the tip is in contact with the sample surface. The force exerted on the sample is controlled by monitoring the cantilever beam and maintaining a set-point deflection value. Contact mode is suitable for scanning the surface of hard materials.

In tapping mode or intermittent contact mode, the cantilever oscillates at a very high frequency, but slightly less than its resonance frequency. The amplitude of the oscillation is the feedback parameter. The probe slightly taps the sample surface, which is less damaging, especially for softer samples. The oscillation amplitude changes as the tip moves closer or away from the sample surface. The feedback circuit adjusts the probe height to maintain the amplitude set-point.

For highly sensitive measurements non-contact modes are ideal. They are similar to tapping mode except the tip is made to oscillate at a much lower amplitude (between 10-100 nm)[85]. Non-contact mode exerts less normal and lateral force compared to tapping and contact modes.

a)

Feedback Loop

Laser light source

Detector

Z-scanner

Cantilever with tip

Sample

AFM stage with XY-scanner

b)

Contact mode

Repulsive

Force

0

Tapping mode

Attractive

Non contact mode
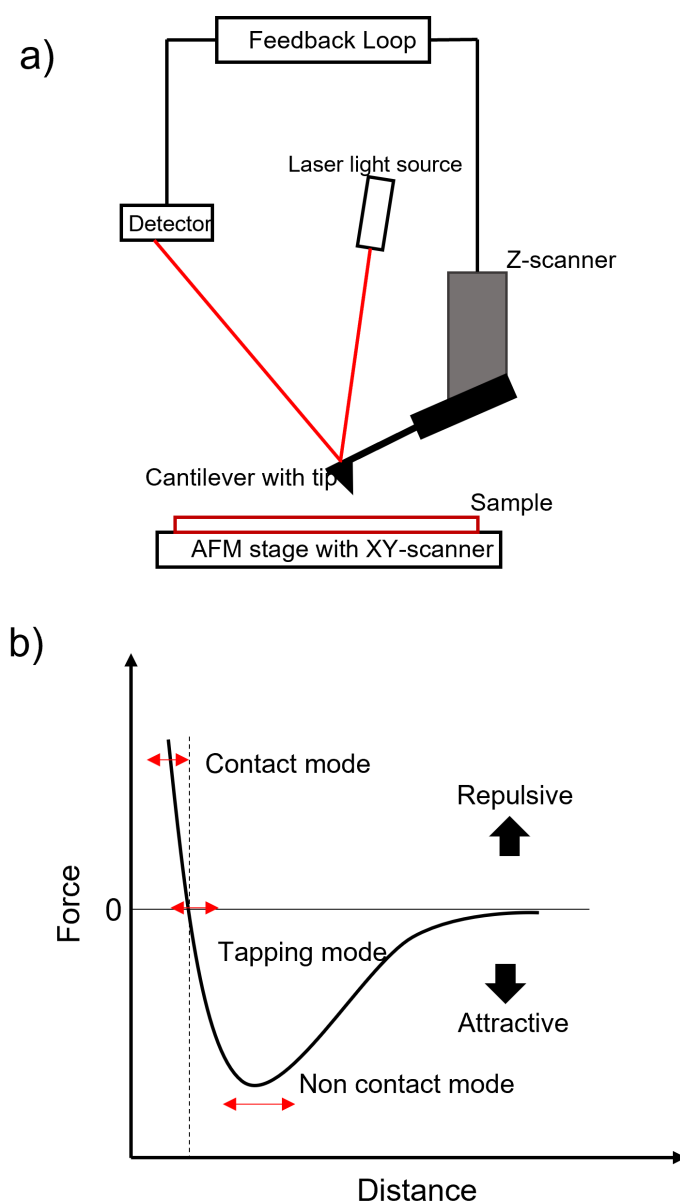
Distance

FIGURE 3.8. a) Schematics of a simple AFM set-up b) Force-distance curve of tip-specimen pair.

The oscillation amplitude is considered the feedback parameter for non-contact mode.

For imaging samples, a Veeco dimension 3100 series AFM system was used in this work. General-purpose tapping mode tips with a resonant frequency of 350kHz were used. The tips were commercially bought from AppNano and NuNano.

3.6 High-speed AFM

High-Speed AFM or HS-AFM follows the same principle as the conventional AFM mentioned in section 3.5, the distinction comes from the fast data collection ability of the HS-AFM. It is capable of imaging an area of dimension ranging from millimetres to centimetres in seconds. For comparison, a 4x4μm image of pixel size $\approx$ 8nm takes up to 10 minutes to be imaged on a conventional AFM. Meanwhile, the HS-AFM can measure 4x4μm size image in 500ms with a pixel size of 4nm[85]. The HS-AFM was developed in 2004 by Bristol Nanodynamics as a part of research carried out at the University of Bristol. The system has developed since and is now commercially sold by Bristol Nanodynamics.

To move the cantilever across a sample surface with precision, piezoelectric materials are used in AFMs. The home-built HS-AFM stage design consists of ceramic piezoelectric actuators and metal supports called flexures, enabling the sample to be scanned up to a rate of 64μm^2 /sec [86]. The flexure mechanism and piezoelectric actuators can decouple both the x and y-axis motions separately and retain structural rigidity[87]. In this design, the tip will remain stationary while scanning and the sample surface is translated under the cantilever by the stage. Displacement of the cantilever as it undergoes deflection while scanning the sample surface is measured by an interferometric detection system. A laser Doppler vibrometer detects the laser beam reflected off of the cantilever then helps to measure z-displacement accurately. The displacement data can be converted into topographic maps of the surface which is done by custom-made software by Bristol Nanodynamics.

 In-situ real-time observation of processes is possible with the HS-AFM in both air and liquid environment with a high rate of data acquisition. Figure 3.9 shows the Bristol Nanodynamics contact mode HS-AFM. Figure 3.10 shows the 3D version of the HS-AFM mentioned in Figure 3.9.

Commercially available AFM cantilever 'C' on AFM probe (Bruker MSNL) was used for all measurements. The probe consists of a silicon nitride cantilever and a silicon tip with a spring constant of 0.01N/m^{-1}. All the image processing was carried out using Bristol Nanodynamics proprietary software and Gwydiyyon.
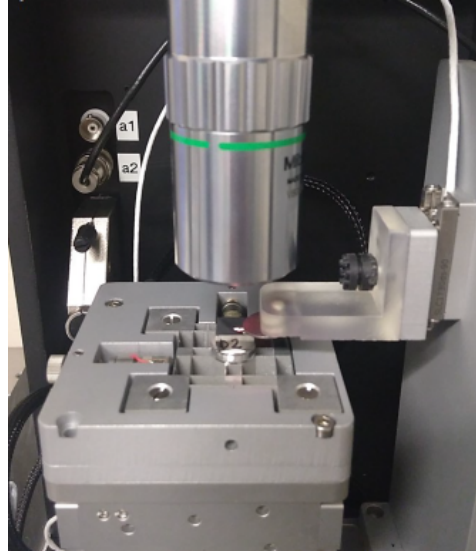
FIGURE 3.9. The contact mode HS-AFM instrument developed by Bristol Nanodynamics[88].
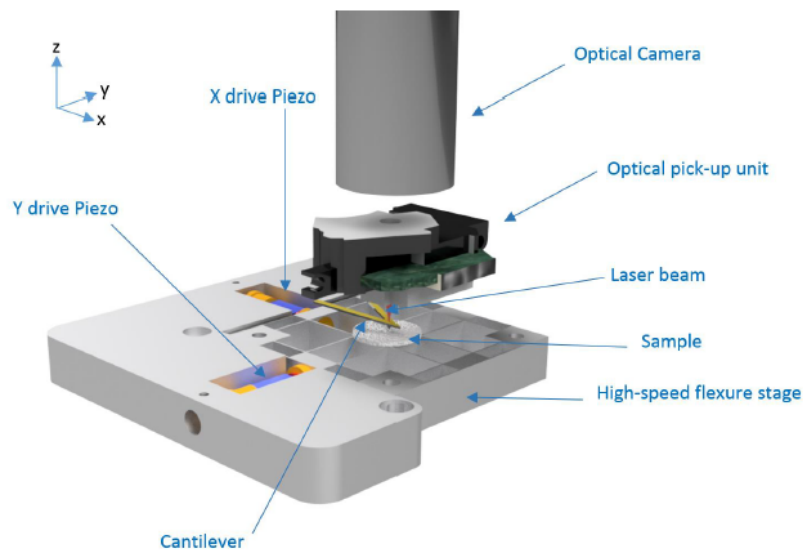
FIGURE 3.10. A simplified 3D- model of the fast-moving home-built flexure stage of the contact mode HS-AFM from figure 3.9. The flexures maintain the structural rigidity and the piezoelectric actuators control the X and Y motion [86].

3.7 Scanning Electron Microscope

Scanning Electron Microscopy is a non-destructive technique used for imaging the surface of non-biological and biological samples. The microscope works by raster scanning the sample surface using high-energy electrons (5-60KeV). The primary electrons interact with the atoms in the
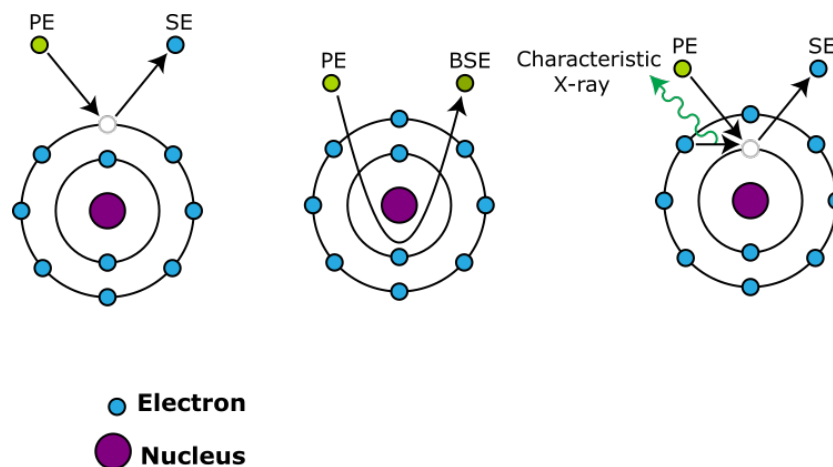
FIGURE 3.11. Different signals generated from atoms of the sample as they interact with primary electrons(PE). The signals are secondary electrons(SE), backscattered electrons(BSE) and characteristic X-rays[89].

sample causing various signals to be emitted. Among those signals are secondary electrons(SE) ejected from the sample atoms through inelastic scattering. The quantity of electrons emitted is directly related to topographical features, thus making it possible to construct an image of the sample surface. Electrons have a larger momentum and smaller de Broglie wavelength revealing structures as small as 5nm using a well-configured, minimal interference SEM machine. Other signals due to the primary electrons are backscattered electrons (BSE) produced by elastic scattering and X-rays emitted by the removal of inner-shell electrons by the incoming electron beam. BSE is produced by elastic scattering of the primary beam of electrons after interacting with the nucleus of the atoms. BSE originates from the deeper interaction volume of the sample. Atoms with higher atomic number(z) and density efficiently generate BSE and this dependence of BSE on atomic number helps to detect different phases in the sample. BSE can also provide information about the chemical composition, crystallography and topographic information. Samples imaged under SEM must be made conductive to avoid the charging effect on the specimen. Figure 3.11 and 3.12 show the type of signals emitted from the sample and volume for electron-matter interaction.
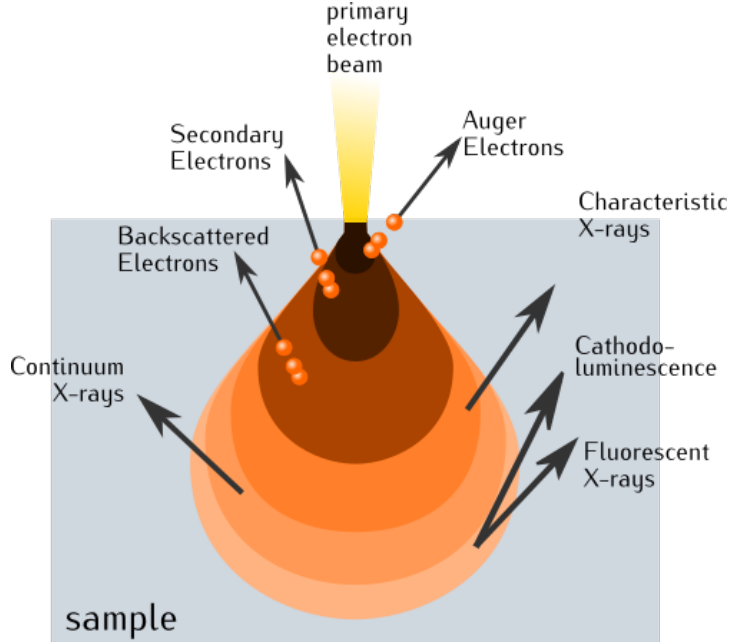
FIGURE 3.12. Volume for electron-matter interaction [90].

3.8 X-ray Diffraction

X-rays typically have a wavelength between roughly 0.1Å and 100Å, which is comparable to the inter-atomic distances of crystals. When X-rays are incident on a sample, they are scattered by the electrons of the atoms in the sample. This makes X-rays perfect for studying crystallographic structures and identifying phases by matching data from known structures. When X-rays are diffracted by atoms, they interfere constructively. Figure 3.13 shows the scattering of X-rays from atomic planes. The condition of constructive interference is that when X-rays scatter from two adjacent planes, their path difference must be an integer multiple of the X-ray wavelength λ. The path difference is given by,

$$n\lambda = 2d sin\theta \tag{3.2}$$

where n is an integer, the order of reflection, d is the spacing between the adjacent planes in the atomic lattice, and θ is the angle between the incident ray and the diffracted plane[58]. The angle between the transmitted and diffracted ray is 2θ.

The experimental setup usually consists of an X-ray source. For the experiments mentioned in this thesis Cu K_α served as the source, and Ni foil acted as a filter to block out K_β x-rays.

39
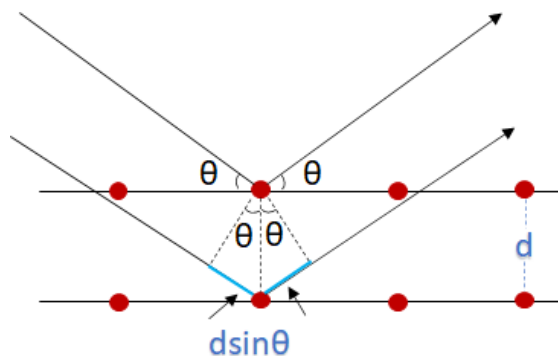
FIGURE 3.13. X-ray diffraction from atomic planes obeying Bragg's law of diffraction.

3.9 Focused Ion Beam

A Focused Ion Beam(FIB) is a versatile instrument that is very similar to a Scanning Electron Microscope. The difference comes from using focused ions (Ga^+) instead of electrons for probing the surface. Ions being heavier in mass, sputters the surface, cutting into the sample by etching away atoms from the material. Figure 4.2 illustrates the sputtering process involved during FIB milling. Sputtering involves momentum transfer between the primary ions and the target atoms. As the ions strike the surface of the material, a collision cascade 10-25nm into the target material is created. The knock-on effect of the cascade results in several mechanisms causing the sputtering of the atoms at the target surface. The etching rate is controlled by varying the beam current. Before imaging the surface using the FIB, the area of interest is polished using a small beam current which produces smooth surfaces. The primary ion beam of FIB produces both secondary electrons and secondary ions as shown. FIB secondary electrons give excellent grain contrast, which makes FIB a good tool to study the microstructure of a material. To protect the top surface from the destructive beam when making a trench, a metal is locally deposited on the surface, for instance, Pt in our case. This is achieved through FIB-assisted chemical vapour deposition. A gas such as $C_5H_5Pt(CH_3)_3$ is introduced to the vacuum chamber and is allowed to chemisorb onto the sample. By performing a raster scan with Ga^+ ions around this area, the precursor gas will be decomposed to a non-volatile component, Pt in this instance. This Pt remains as the top layer on the sample, protecting the surface underneath it.
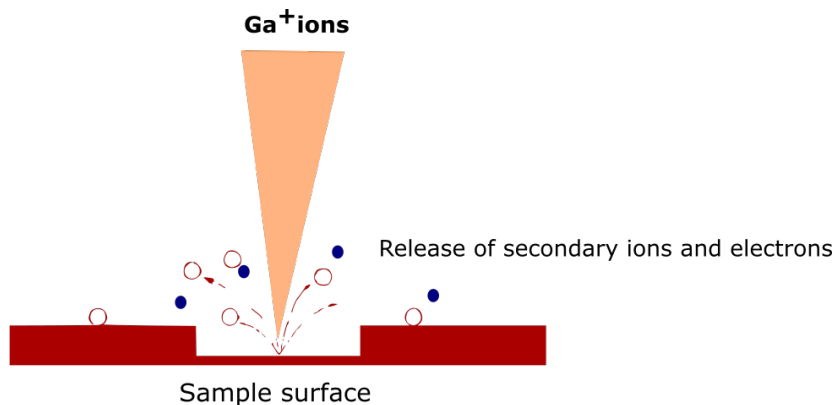
FIGURE 3.14. Schematic diagram of FIB sputtering effect.

3.10 Electron Back Scatter Diffraction

EBSD is an SEM-based diffraction technique that has the ability to provide microstructural information. EBSD includes crystallographic orientation, grain size, phase or strain of material. This setup requires a polished\flat sample slanted to 70^0 using a pre-tilted holder, a phosphor screen that shows the pattern from the sample, and a sensitive camera for visualizing the pattern formed on the screen. The EBSD setup is shown in figure 3.15. When the electron beam from the SEM is focused on the slanted crystalline sample, some electrons are diffracted satisfying Bragg's condition referred to in section 3.8. The diffracted electrons produce a group of paired large-angle cones, which represent each diffracting atomic plane. The enhanced electron intensity crosses the phosphor screen creating Kikuchi bands as shown in figure 3.16. The Kikuchi bands can be indexed by the Miller indices of the diffracting planes. The diffraction pattern is tied to the crystal structure. Thus changing the orientation of the crystal can change the diffraction pattern. The position of Kikuchi bands will therefore give the orientation of the diffracting crystal.
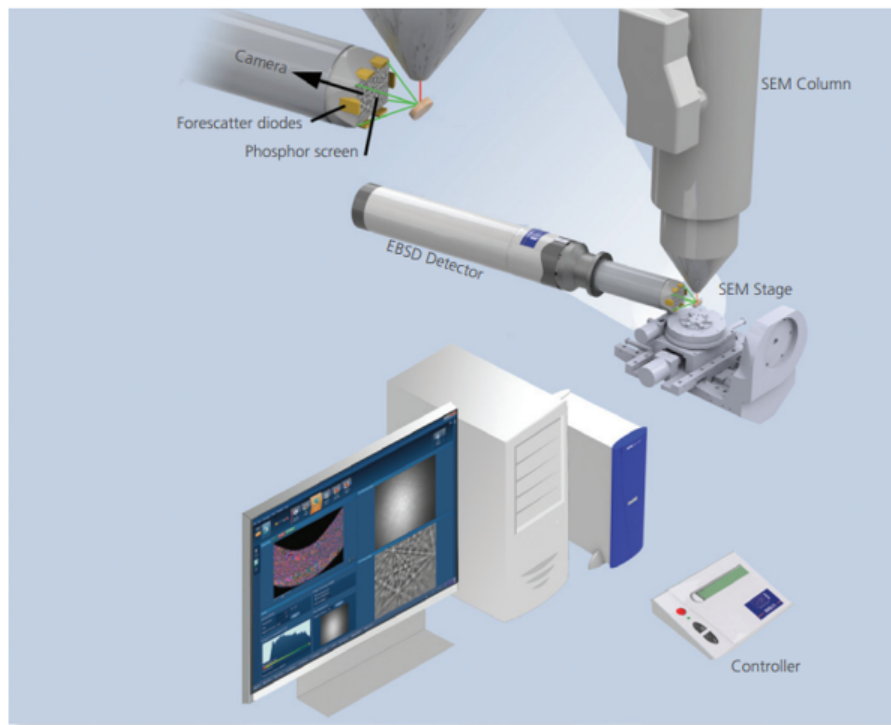
FIGURE 3.15. Schematic of an EBSD system showing the principle components[91, 92].
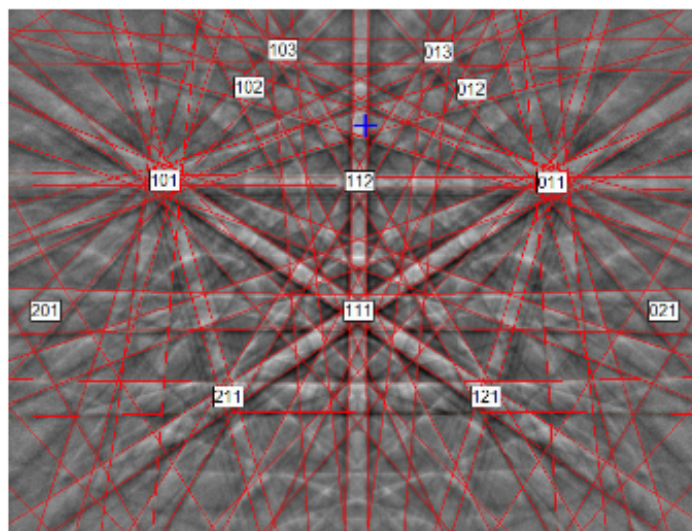
FIGURE 3.16. Example of Kikuchi pattern observed during an EBSD measurement[91]. The indexed planes are marked on the bands.

IN-SITU IMAGING OF CU FILM USING HS-AFM

I n this chapter, the HS-AFM was used for direct observation of a polycrystalline Cu film growing from an additive-free electrolyte solution. In situ probing techniques can provide insight into the atomistic processes involved during the growth mechanism of thin films. The direct observation of polycrystalline film growth can give information about the structural coarsening happening during film growth, which remains a poorly understood phenomenon. In situ STM can provide high-resolution images at a rate of 1.18 Hz[93]. Unfortunately, these experiments were limited to relatively slow deposition rates. For example, an in situ STM study of gold evaporation on a quartz substrate was carried out at a deposition flux as slow as 7.8A^o per hour[94]. The in situ AFM previously used, for example, to study electrodeposited Zn films was of relatively low speed, often requiring interruption of the deposition process to image the surface. During this study, a holding time of 10 minutes was reported for capturing an image consisting of 512 pixels per line (pixel size $\approx$ 8nm)[95]. The few previous HS-AFM studies conducted were mainly on Au(111) single-crystals, mostly focusing on the nucleation mechanism of Cu grown from a solution of 3mM copper sulphate with 50mM sulfuric acid. The experiments were conducted for a time of up to 20s, with the HS-AFM scanning an area of 375-1000 nm^2 with a scan speed of 1 frame/sec[96, 97].

In our work, we used contact-mode HS-AFM to image a growing Cu film during electrode-

position to study the later stages of film growth. This is the first work to obtain high-resolution images of a polycrystalline thin film grown at a high rate (up to ≈0.5nm/s) to understand the surface evolution processes involved during the growth process of a metallic polycrystalline film. For quantitative description, scaling analysis and slope analysis were performed on the AFM images to understand the surface roughness evolution.

The work discussed in this chapter has been published [98]. Some contents and figures are taken from the paper. This paper was written by the author of this thesis with only limited contributions from her co-authors.

4.1 Experimental set-up for HS-AFM and growth rate determination

A 3D-printed electrochemical cell specially designed for in-situ HS-AFM was used to conduct the experiments. The cell design is in such a way that the potentiostat can be connected to the conducting pins on the electrochemical cell without tugging or pulling on the cell. The metal arm on the electrochemical cell contacts the WE and CE/RE can be fixed in place by a screw without touching the WE. This cell is also capable of holding a small volume of electrolyte without spilling. The liquid forms a perfect meniscus between the AFM cantilever and the working electrode. The electrochemical cell setup is shown in figure 4.1.

The Au substrates used for measurements were cleaned using sulphuric acid, then rinsed with DI water, and blow-dried using nitrogen before conducting experiments. All the substrates used in this study were imaged using AFM multiple times at different regions of the sample. Figure 4.2a shows the morphology of the Au imaged using AFM. The RMS roughness of the substrate was measured to be ≈ 2.86 nm. The microstructure of the polycrystalline Au was characterized using XRD. Figure 4.2b shows the θ-2θ measurements of the bare Au substrate. The Au, with a thickness of 200 nm, exhibits (111) orientation. The Cu films grown on the Au substrates are polycrystalline with predominantly (111) texture. The Cu film could inherit the texture of the polycrystalline substrate. In the later chapters of the thesis, as the thickness of the Cu increased
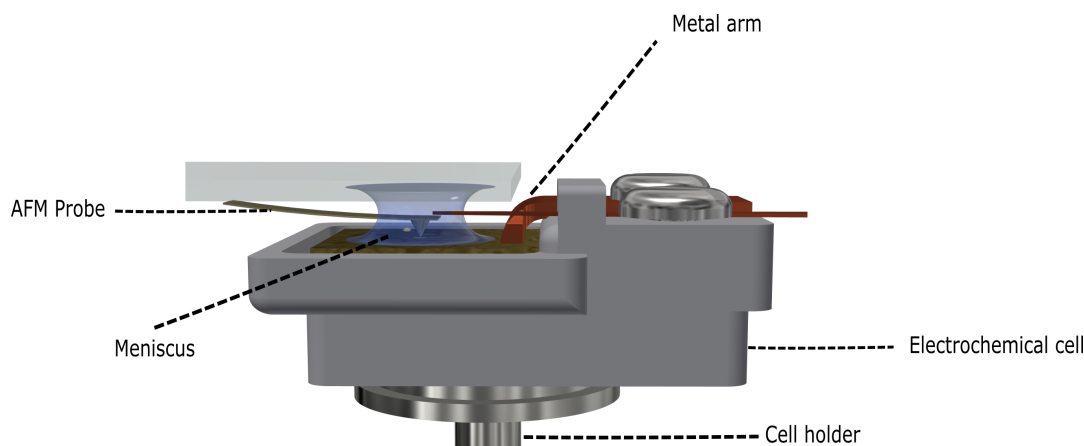
FIGURE 4.1. 3D view of the electrochemical cell set-up used for the HS-AFM experiment.

significantly, the film developed a texture of different orientations.

A two-electrode system consisting of an Au microelectrode of diameter 30μm was fabricated using photolithography, served as the working electrode (section 3.3) and a Cu strip acted both as a reference and the counter electrode. Compared to macroelectrodes, small currents are observed in microelectrodes, almost six orders of magnitude smaller than that of a macroelectrode[99]. By using a microelectrode the iR effects can be reduced making measurements on microelectrodes using a two-electrode arrangement meaningful. Also, the CE is much bigger than the WE. So the polarization of the CE is minimized (as the current density on an electrode of large surface area is low). The electrolyte solution was 0.01M $CuSO_4$+0.1M H_2SO_4, deaerated for 30 minutes. A potential of -200mV versus Cu/Cu^{2+} was applied for 120s. From the CV taken on the microelectrode, the deposition is expected to be under the mixed regime. Figure 4.3 shows the CV taken on the microelectrode with Cu as the reference electrode. Depending on the potential applied, the electrode reactions could belong to three regimes. Kinetic control (rate determining step is charge transfer) for small applied potential, mass transport control(rate determining step is mass transport of materials towards the electrode from the bulk of the electrolyte) for higher applied potential and the mixed kinetic-diffusion control regime for the potential in-between. From the CV, the region where the cathodic current recorded is very small has a concentration of reactants not much different from the bulk. This is the kinetic control regime and the current depends on the rate of charge transfer. The region where the cathodic current plateau (from -0.4V

a)

b)
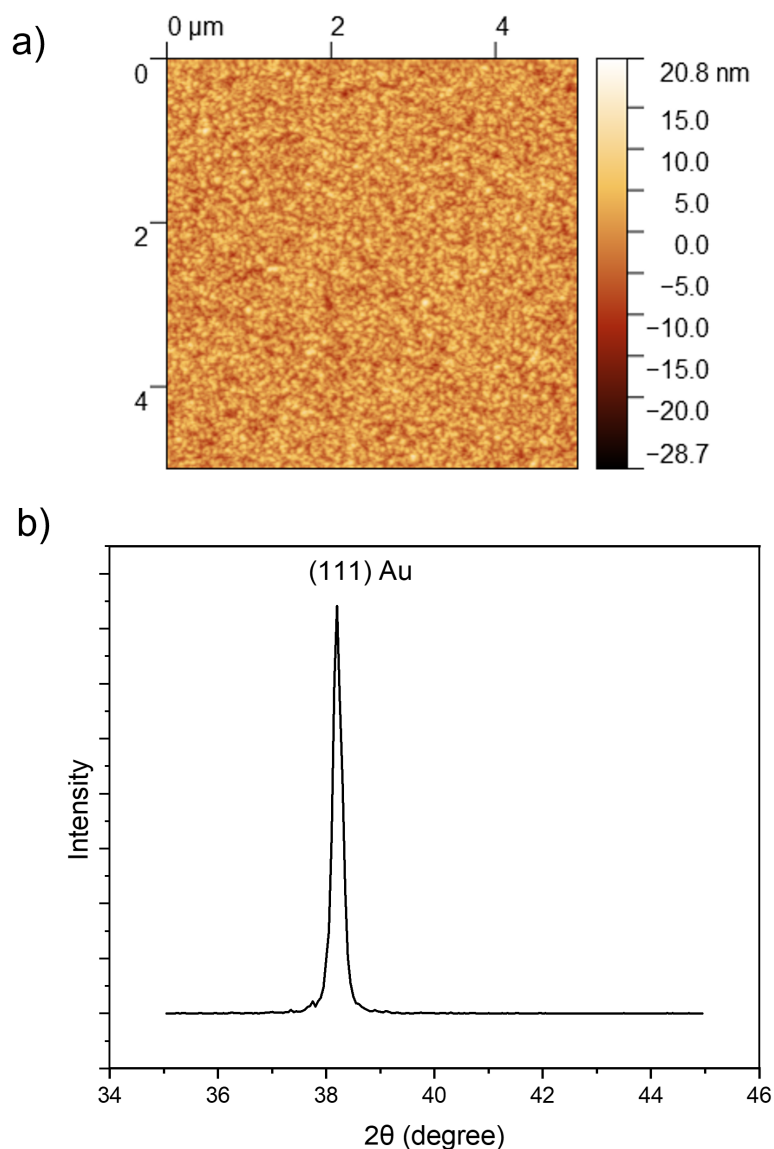
FIGURE 4.2. a) AFM image of the Au substrate before Cu deposition b) $\theta - 2\theta$ measurements of the bare Au substrate showing (111) orientation.

in figure 4.3) is the mass transport control regime. The rising part of the cathodic current before the mass transport regime is considered the mixed control regime. At the chosen potential, the deposition is not too fast or slow and the coarsening stage of film growth can be observed using the HS-AFM. To study the influence of deposition potential on growth in the future, -200mV was chosen as a reasonable starting point.
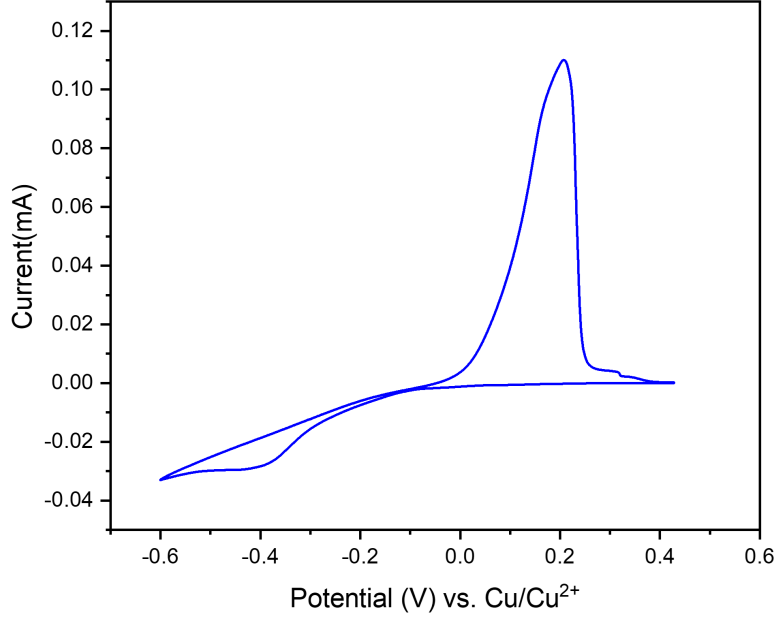
FIGURE 4.3. CV performed on the Au microelectrode measured at a scan rate of 100mV/s.

For a standard cathode reaction:

$$Cu^{2+}(aq) + 2e^- \rightleftharpoons Cu(s) \tag{4.1}$$
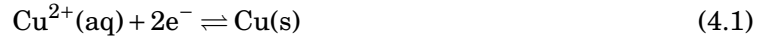
the E^0 of Cu/Cu^{2+} relative to SHE is +0.34V[100]. By calculating the area under the curve of the cyclic voltammogram and dividing this value by the scan rate, it is possible to determine the total charge involved during the reduction ($Q_{cathode}$) and oxidation (Q_{Anode}) processes. $Q_{cathode}$ and Q_{Anode} are found to be 2.2×10^{-5} C and 1.3×10^{-4} C respectively. The steady-state current was calculated using the equation 2.18 and 2.19 from section 2.5. For a microelectrode of radius 15μm, diffusion coefficient 0.78×10^{-9} m^2/s [101] and for the total number of 2 electrons involved in the reaction to reduce Cu^{2+}, the current I_{ss} is 0.90 pA and for a microelectrode of recess depth 1μm, $I_{ss}^{recessed}$ is 0.83 pA. The difference between the current of inlaid and recessed microelectrode is small. This is because the recess depth is much smaller than the diameter of the microelectrode.

The deposition rate was determined by making a line cut across the edge of the photoresist and the Au microelectrode surface from the HS-AFM images taken before and after deposition on a sample deposited under the same condition. The line cut gives the vertical profile of the height

47
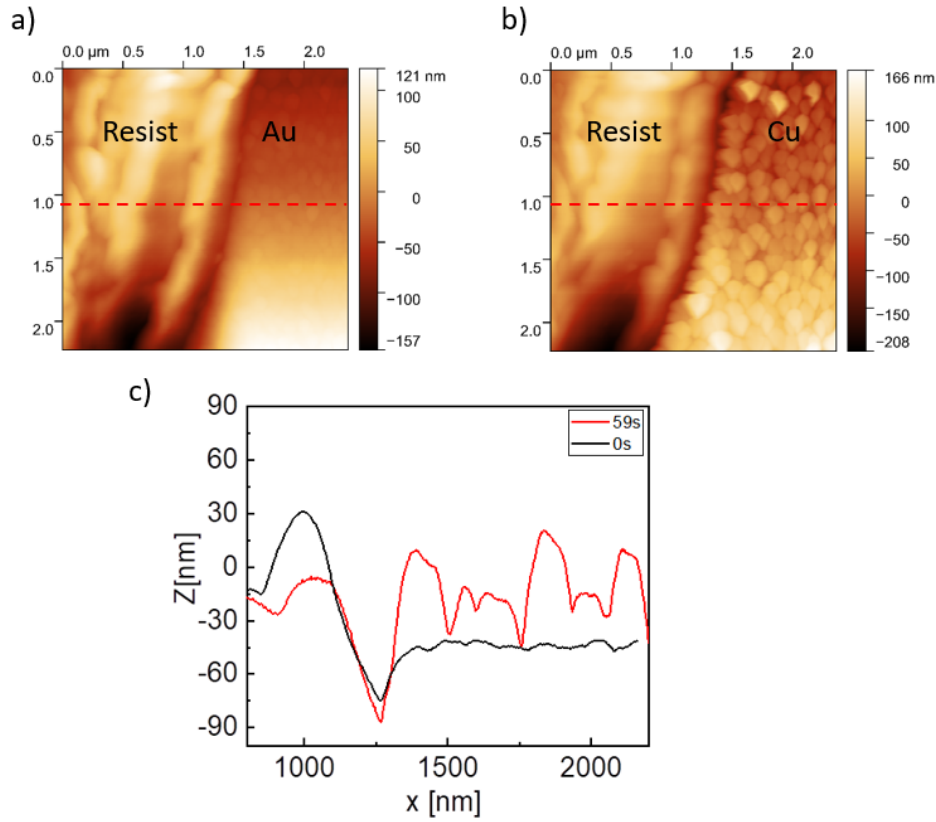
FIGURE 4.4. HS-AFM images of the sample surface. The red dashed line represents the region across which the vertical profile was taken a) HS-AFM of the photoresist-Au surface at deposition time $t \sim 0$s b) HS-AFM image of photoresist-Cu surface at time $t \sim 59$s c) Vertical profile of figure 4.4a and b.

of the Cu deposit after 1 minute of deposition. Figure 4.4a shows the HS-AFM image before the commencing of electrodeposition. Figure 4.4b shows the HS-AFM image after the deposition of Cu for one minute. Figure 4.4c represents the vertical profile of figures 4.4a and b. A total thickness of ≈ 30nm was deposited in 1 minute. From this, the deposition rate was determined to be ≈ 0.5nm/s.

4.2 Accelerated local grain growth and grain overgrowth

The HS-AFM experiment involves scanning a fixed area, in our case 2x2 μm, and observing the growth of the Cu film. Instead of generating a single image, HS-AFM produces a video of the whole process, from the onset of deposition to the end of deposition at a frame rate of 2
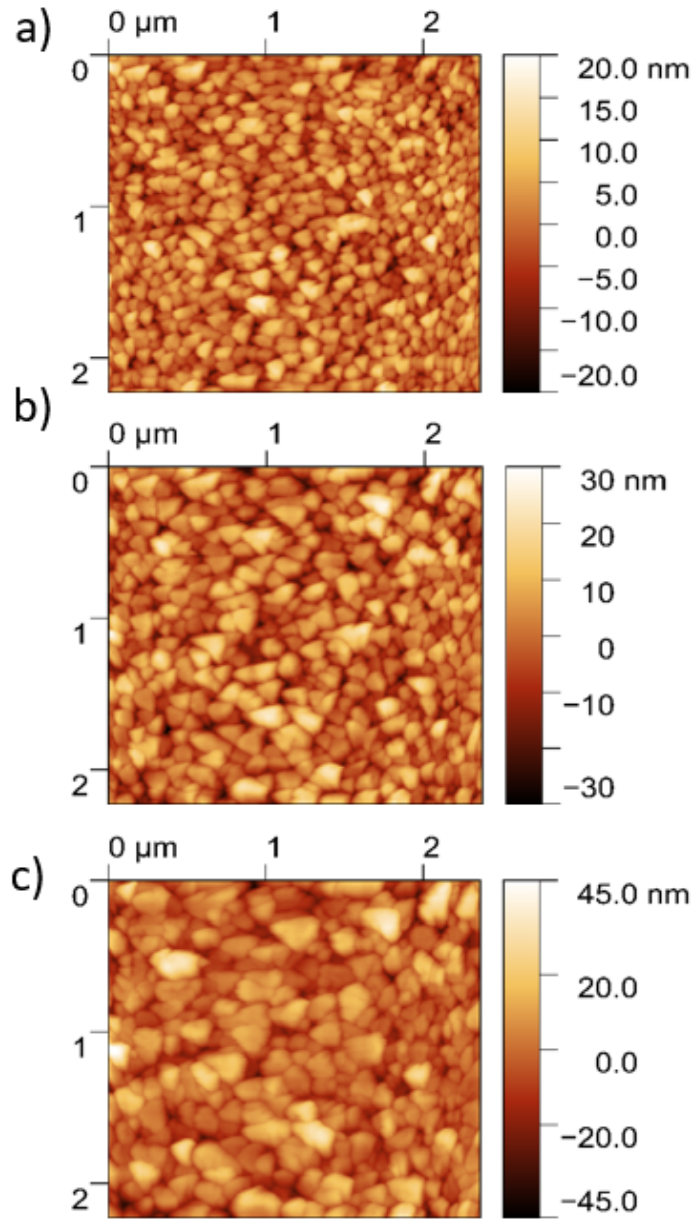
FIGURE 4.5. AFM images of Cu film at different stages of growth i.e. at different times. a) $t \sim 24s$ b) $t \sim 68s$ c) $t \sim 119s$.

million pixels per second. Figure 4.5 shows the Cu film at different times during deposition,i.e., at different stages of growth. It is clear from figure 4.5 that the size of the grains increases with deposition time. 'Grains' in this thesis refers to topographic features that may consist of multiple crystallites. A triangular bias to the shape of the grains is likely due to tip convolution effects,

49
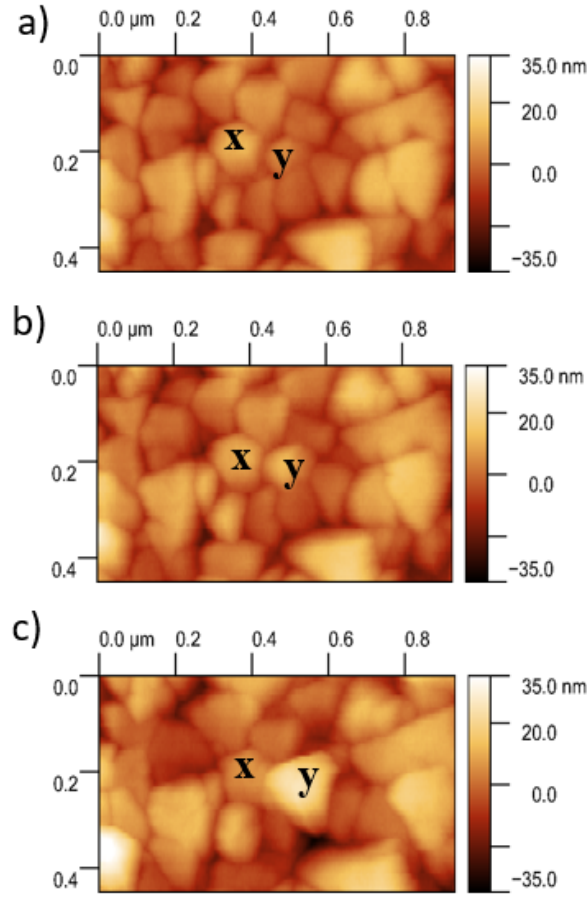
FIGURE 4.6. High magnification AFM images of Cu film with grains exhibiting accelerated local growth. a) $t \sim$ 68s b) $t \sim$ 77s c) $t \sim$ 101s.

this didn't interfere with any of the results obtained. During the HS-AFM experiment, the tip scans a dynamic environment where the height of the sample surface is constantly changing. This sudden change in tip-sample distance could lead to the tip having close contact with the sample surface, affecting tip quality, and causing a triangular bias to the shape of the grains. Similar events were recorded by Esaki et.al during the HS-AFM observation of PEG adsorption on Au(100). In their studies, the tip-sample force was modified, reaching a maximum value of 0.54 nN. After that, the images became distorted once the tip-sample force was modified to a higher value[102]. How to reduce the tip convolution effects prominent during HS-AFM experiments needs to be investigated in the future. The formation of new Cu grains on the bare Au substrate was visible during the commencement of the deposition process compared to the growth stage.
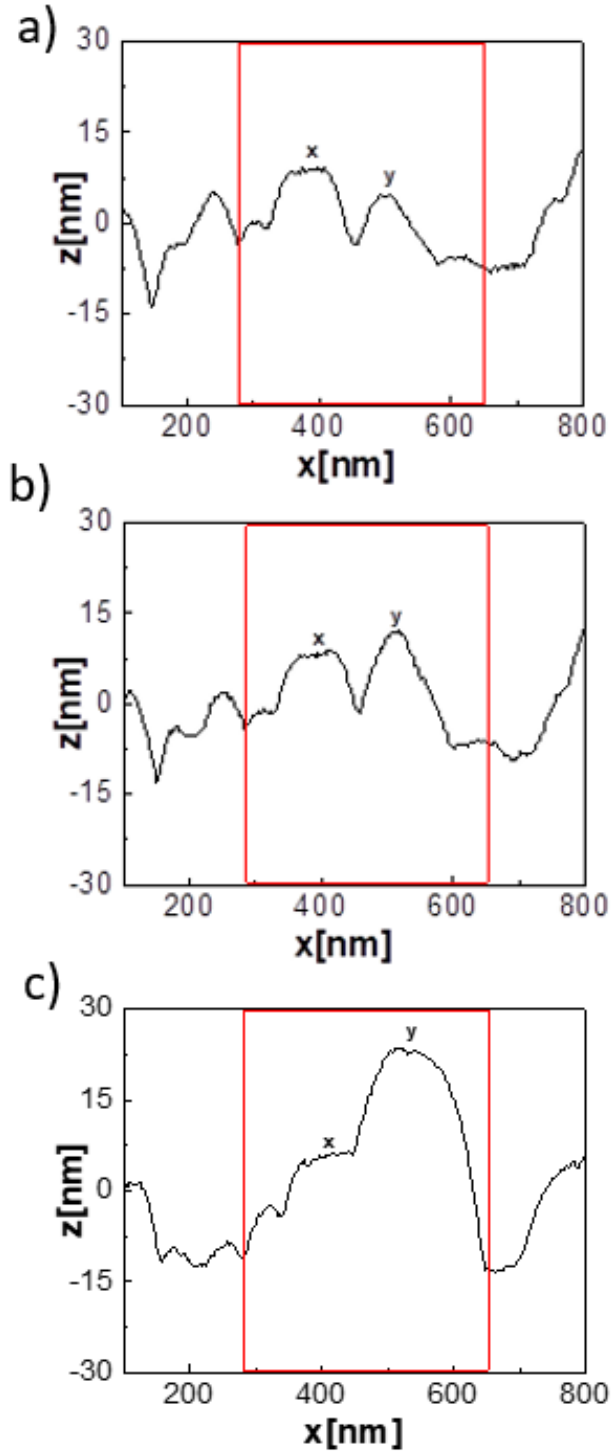
FIGURE 4.7. Vertical height profiles of the high magnification AFM images in figure 4.6. Cross-section of AFM images of figure 4.6a-c.
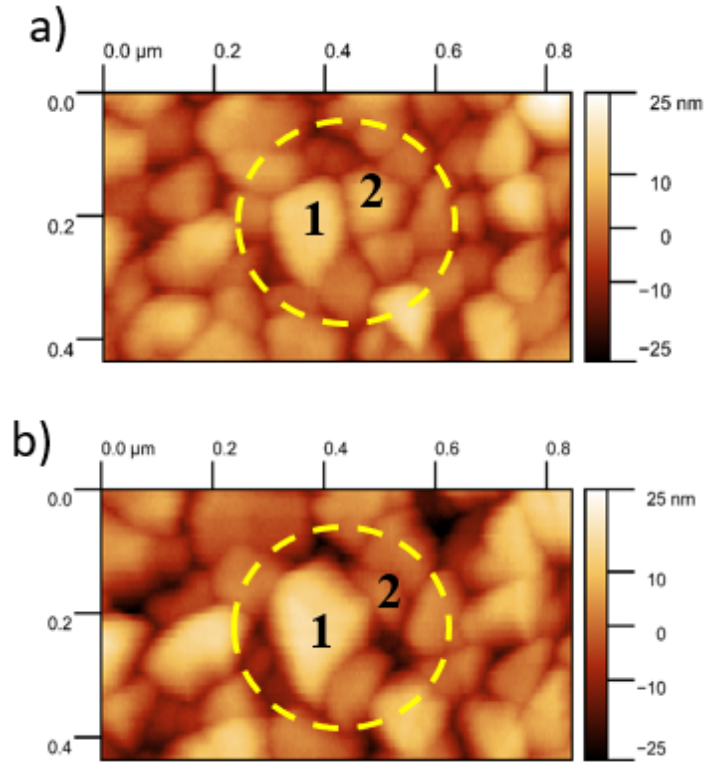
FIGURE 4.8. High magnification AFM image of grain '1' over growing its neighbour marked '2' a) $t \sim 45$s b) $t \sim 89$s.

The tip convolution effect is much more significant in the early stages of film growth. Due to this reason, obtaining information about individual nucleation is impossible from our experiment. For HS-AFM studies involving nucleation, a small area of 200-1000 nm is ideal for scanning.

Direct observation of the film growth enabled us to identify different phenomena taking place on the film surface as the thickness of the film increased. Accelerated local grain growth was identified at different locations on the Cu film. Accelerated local growth in this thesis is defined as a non-uniform growth pattern where certain grains grow faster than their neighbours at different rates. An example of accelerated growth is given in figure 4.6. In figure 4.6 two grains are of interest, marked 'x' and 'y'. The AFM images were taken at different times during the growth process. From figure 4.6b, it is clear that grain 'y' is gradually growing faster than its neighbour 'x'. This is truly evident in figure 4.6c, where grain 'y' has grown significantly higher than 'x'. By taking a cross-section across grains 'x' and 'y', the height difference is immediately apparent.

Figure 4.7 corresponds to such a vertical profile taken across the AFM images represented by figure 4.6. From figure 4.7a, the height of grain 'y' is lower than 'x' at the deposition time $t \sim$ 68s. As the growth proceeds, around $t \sim$ 77s, 'y' starts to grow faster than 'x'. With increasing thickness, the height of 'y' overtakes 'x' as shown in figure 4.7c.

Non-uniform growth rates sometimes result in one grain growing over its neighbouring grain. An example of overgrowth is when grain 'y' from figure 4.7c overtakes its neighbour and laterally overgrows 'x'. Figure 4.8 also is an example, demonstrating grain marked '1' overgrowing its neighbour '2'. The non-uniform growth rate of grains could be due to the influence of the microstructure of the film.

4.3 Quantitative description of surface morphology

Quantitative information on surface topography can be obtained by using scaling and slope analysis on the HS-AFM images. This is possible because the HS-AFM images consist of 1000x1000 arrays, with row and column defining the position on the image and the corresponding array element being the height at that position. Scaling analysis gives values of global parameters associated with morphology changes like H, β_{loc} and β, and slope analysis gives the local slope θ values.

4.3.1 Scaling analysis of AFM images

Scaling analysis was performed on different frames taken at different times during the deposition. Figure 4.9 shows the experimental surface scaling w as a function of length scale l. Scaling data in Figure 4.9 can be fitted using the following function[73]:

$$w(l) = w_{sat}\left(1 - \exp\left[-(l/l_c)^H\right]\right) \tag{4.2}$$

Here w_{sat} is the value at which the roughness saturates in the scaling data. l is the length scale over which the roughness is measured. l_c is the cross-over length, the point where the transition between the constant slope and constant w occurs and H is the Hurst exponent. The values obtained by fitting equation 4.1 are given in table 4.1. Instead of fitting two separate straight lines to the data, a single function in equation 4.1 gives the best fit to the scaling curve in figure
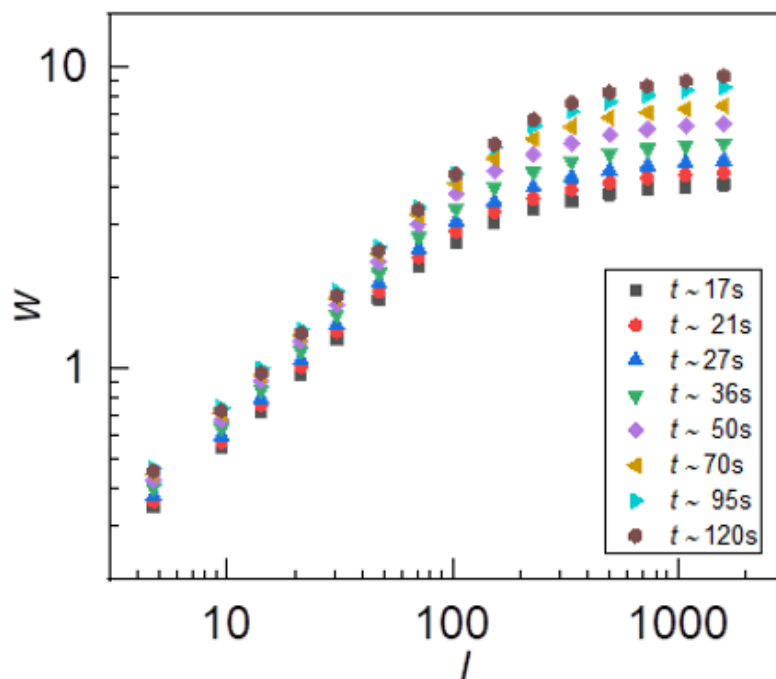
FIGURE 4.9. Logarithmic plot of surface width w at different times t, plotted against log l, the length scale over which it is measured.

4.9. The gradient of log w v/s log t plot for small length scale is β_{loc}. The gradient of log w_{sat} v/s log t gives the value of $\beta + \beta_{loc}$. Figure 4.10 indicates that a plot of log w_{sat} v/s log t is linear and

H	$\beta + \beta_{loc}$	β_{loc}
0.82±0.01	0.43±0.04	0.23±0.01

Table 4.1: Calculated values of the scaling exponents for the Cu film.

equation 2.25 holds. For small values of l, from Figure 4.9, w v/s t curves are separated indicating that w increases with t. This is consistent with anomalous scaling. The increase in w with t also for small l, is evidence of the slope of the film increasing.

4.3.2 Slope analysis of AFM images

As a complement to scaling analysis, slope analysis was performed on AFM images. Slope analysis involves calculating the local slope θ as a function of position. Section 2.8 describes how θ can be calculated from AFM images. Figure 4.11 shows the measured probability distribution for θ as
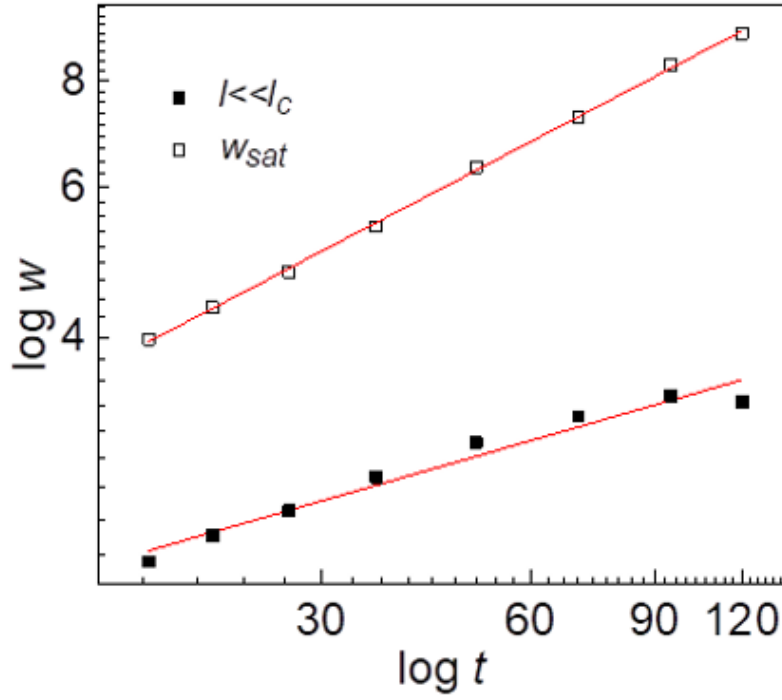
FIGURE 4.10. Logarithmic plot of surface width w as a function of time t for $l \ll l_c$ (l=70nm) and w_{sat} v/s log t.

Time (sec)	$\theta_{mean}(rad)$
17	0.27
21	0.28
27	0.29
36	0.30
50	0.31
70	0.32
95	0.33
120	0.32

Table 4.2: Mean θ values.

the thickness of the film varies. In the previous studies on thick films, the maximum probability distribution shifted to higher values with thicker films[82]. For our film, the trend to increasing θ is noticeable from the change in high θ 'tail'. Table 4.2 shows the mean θ values for different thicknesses for the data in Figure 4.11. From table 4.2, it is clear that the mean θ values are increasing with time except for 120s. A similar trend is also seen in scaling data in figure 4.9.
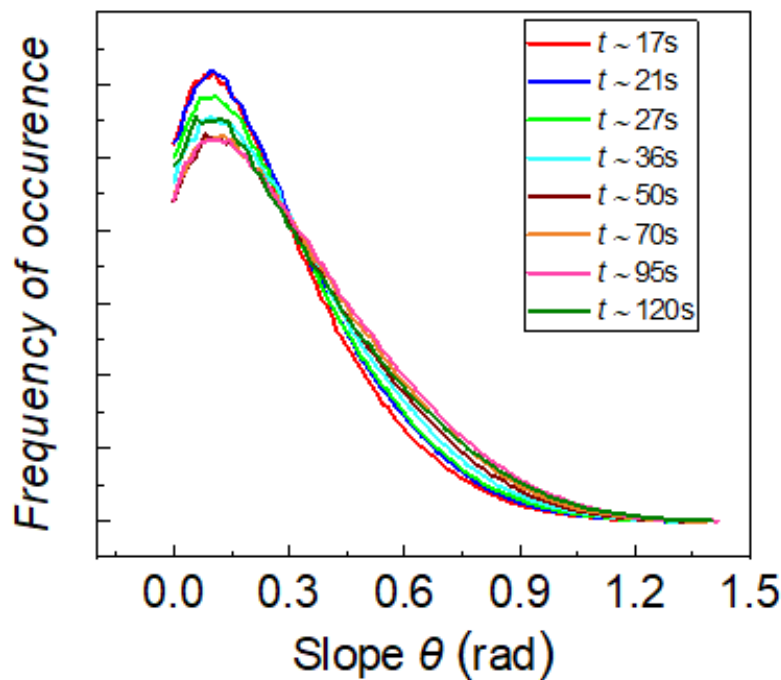
FIGURE 4.11. Plot of frequency of occurrence v/s the local slope θ at different times t.

The scaling curve of 120s and 95s are overlapping indicating that the surface roughness of 120s is not higher than 95s. This would lead to the mean θ value being low for 120s.

4.4 Structural coarsening of Cu film

After nucleation and coalescence, the grains of a polycrystalline film undergo coarsening. The term coarsening referred to in this thesis describes the surface features\grains growing in size with time. We look at the HS-AFM images to understand what drives the grains to grow laterally or if a grain is growing at the expense of others. Quantitative evidence of surface coarsening comes from the increasing value of l_c with changing deposition time. Figure 4.12 shows l_c as a function of time t. The values of l_c are obtained by fitting equation 4.1. l_c depends on the feature size. As the film thickness increases, the feature size also increases as shown in figure 4.12. This has been shown in other studies[80]. Two growth mechanisms were observed during the Cu film growth as discussed in section 4.2, namely accelerated local growth of certain grains with or without grain overgrowth. The discussed pattern of growth could be responsible for structural
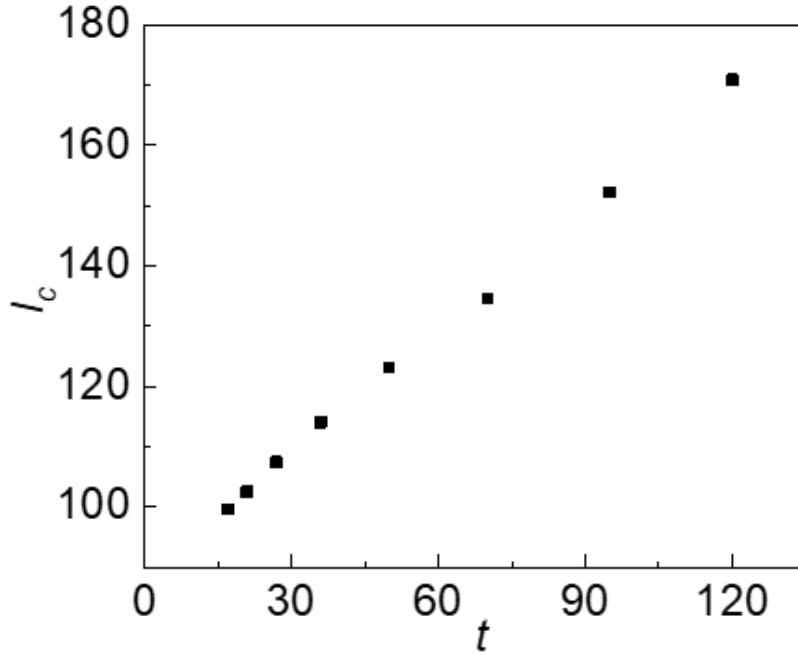
FIGURE 4.12. Plot of l_c as a function of time t. The gradient of log l_c v/s log t gives $\frac{\beta}{H}$.

coarsening. Figure 4.13a-d illustrates these two growth mechanisms. The particular fast-growing grains dominate the topography so that λ is the separation between the features rather than the feature size as shown in Figure 4.13b. Due to the constraints imposed by geometry, the mean slope of the protruding grains increases. Figure 4.13c-d shows an example of overgrowth without change in the mean slope. The slope moves outwards, growing above its neighbours and partially overgrowing them. A combination of these two growth mechanisms shown in 4.13 can take place. An example of this is demonstrated by the cross-section in Figure 4.7c. The grain labelled 'y' has both partly overgrown its neighbour and increased its slope (on the right-hand side of the profile). Figure 4.11 showing the change in θ is direct quantitative evidence of change in slope with deposition time.

Tip convolution effects caused by the tip-sample interaction can reduce the lateral resolution of the AFM. It might have slightly affected the details of the shapes of the profile such as in figure 4.4, 4.9 and 4.11. This does not interfere with the observation of grain growth with time as seen in 4.5. Since the observation of grain growth is a real phenomenon, the arguments of scaling and slope analysis about changes in feature size and slope still stand. So the link between the scaling
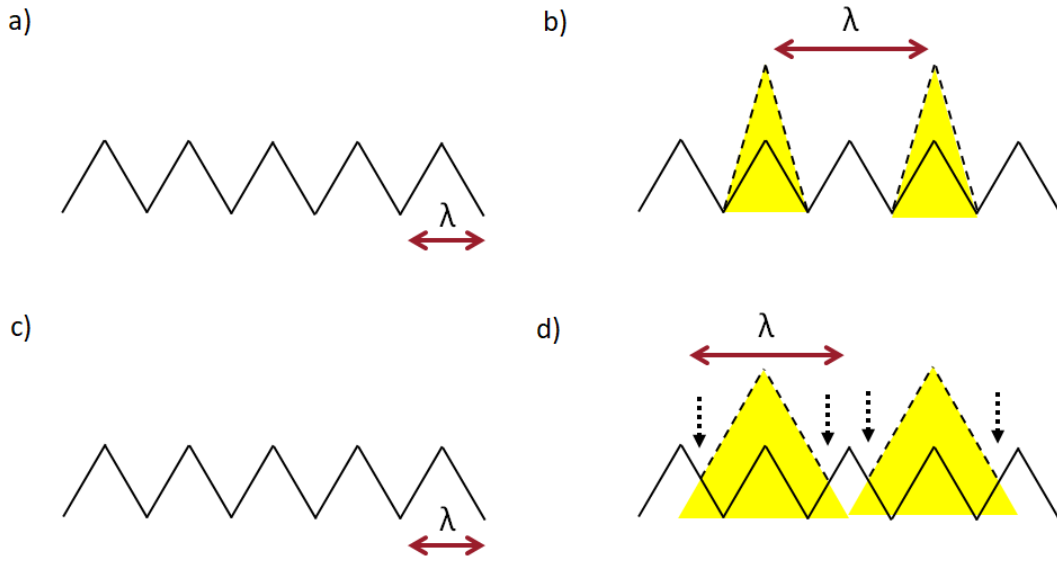
FIGURE 4.13. Schematics showing the structural coarsening mechanism due to different growth rates of adjacent grains. a-b) structural coarsening in the absence of grain overgrowth c-d) in the presence of overgrowth. The arrows in (d) represent the new apparent position of the grain boundary.

and the local slope is valid. The tip convolution effect doesn't alter the observation of accelerated local growth and certainly not the argument of figure 4.13.

The coarsening mechanism of thin films involves the increase in the average size of the grains. Studies focusing on the coarsening mechanism of non-epitaxial film growth are rare. Most works focus on post-growth surface characterization. The in-situ STM study conducted by Rost on polycrystalline Au took place at a very slow deposition flux (7.8Å per hour)[94] during evaporation. For most applications, the film deposition rates are much higher. The HS-AFM enabled us to study the surface evolution of a Cu film at a higher deposition rate. The processes observed during the deposition of the Cu film showed that accelerated local growth of certain grains along with grain overgrowth plays a major role in the coarsening mechanism of the evolving film. This observation of how certain grains dominate the film topography has not been observed in real

time before. The widely accepted model, the Van der Drift model predicted that the structural coarsening results from the evolutionary selection of certain crystals as they grow [44]. The model was proposed under the assumption that the crystals are facetted and that all facets are growing at a uniform rate. Our Cu film does not contain any flat facets and this could indicate that microstructure contributes to the non-uniform growth rate-driven coarsening mechanism.

The overpotential η has three components, activation overpotential, mass transport overpotential and incorporation overpotential[103]. Mass transport or concentration overpotential arises when a concentration gradient develops. Activation overpotential exists when there is a hindrance of charge transfer reaction at the electrode\electrolyte interface. Incorporation overpotential develops when the process of incorporation of atoms into the crystal is hindered. During diffusion-limited growth, if there is a protuberance on the surface, less transport overpotential is required towards this structure resulting in high metal deposition. In our study, the growth is under the mixed diffusion-kinetic regime and the grains with higher growth rates don't initially seem to protrude relative to their neighbours. One example is the grain 'y' in Figure 4.6. For this reason, we don't believe that the enhanced local growth is due to mass transport. We attribute the intermittent rapid growth of certain grains to the presence of half-crystal sites which in turn is a function of microstructure. An atom at a half-crystal site would make contact with half of the number of atomic neighbours compared to a position in the bulk of the crystal[104]. Because of this, the binding energy of an atom at a half-crystal position is half the total energy of an atom in the bulk of the crystal[105]. They are preferred sites for the incorporation of atoms due to the minimum energy at this position. A kink position is considered a half-crystal site.

The five-fold twin structures studied on silver by Pangarov and Velinov could be one possible microstructural feature inducing faster growth among certain grains[106]. These structures contain a 'seam' like region. They host dislocations that promote faster adatom incorporation. Another candidate favouring non-unform growth among grains is stacking faults with atomic steps[107]. Microstructural information on these special growth sites could be extracted by performing FIB and EBSD. These techniques can give deeper insights into the microstructural information like the type of grain boundaries present or the crystallographic orientation of the film.
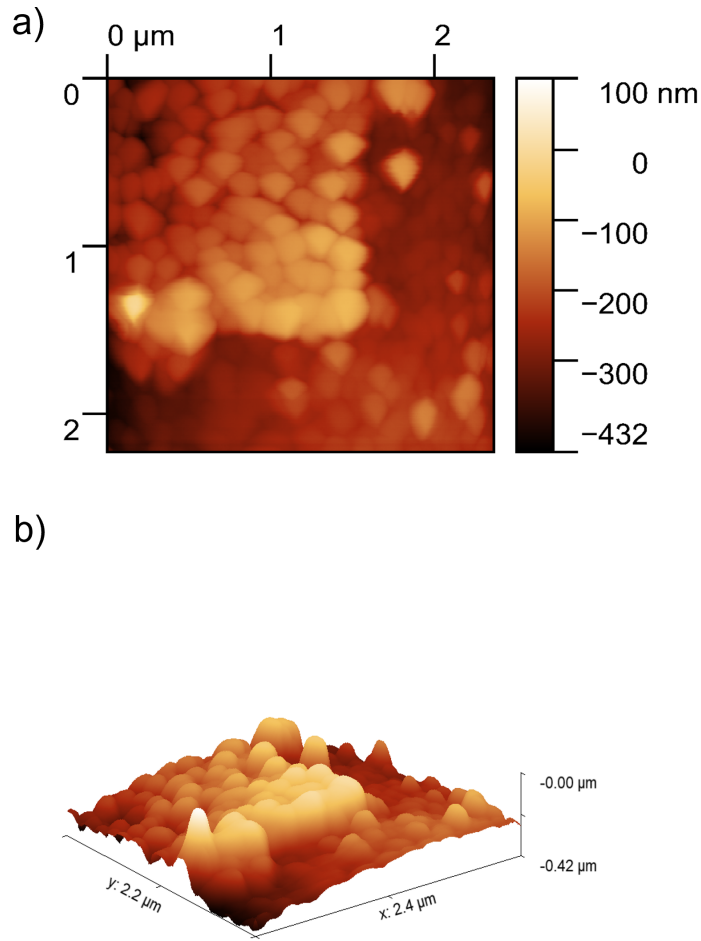
FIGURE 4.14. a) AFM image of a region recorded immediately after the scanning window was moved to a different region during electrodeposition b) 3D representation of the image in (a).

4.5 Observation of tip-enhanced growth

One of the advantages of using the HS-AFM is the ability to move to a different area while scanning without interrupting the deposition process. Figure 4.14 shows an area after such a move as the deposition was continuously proceeding. The brighter region represents the area where the tip was scanning and corresponds to a greater height. The step height between the two regions was estimated to be ≈ 200nm, by taking the vertical profile along the line marked in figure 4.14 is shown in 4.15. It was evident from the vertical profile and 3D image that the tip was able
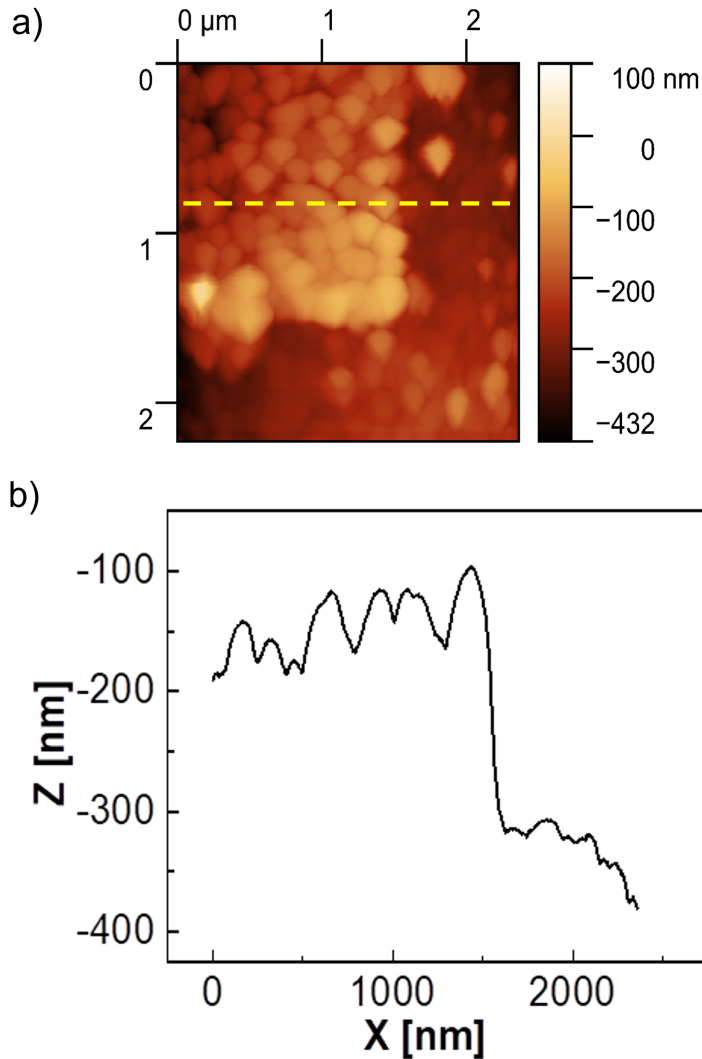
FIGURE 4.15. Vertical height profile taken across the region marked by the yellow dashed line in figure 4.15a. The vertical profile shows a height difference of ≈200nm between the two regions.

to enhance the growth under the region it was scanning. The rapid growth phenomena caused by the AFM tip have been studied before. Lagraff and Gewirth demonstrated the physical local influence of the AFM tip on Cu films grown on single crystal surfaces[108, 109]. They scanned a small window (100x100nm) and later abruptly changed to a bigger window (850x850nm). During measurements, they changed the tip-sample force from 5±2 nN to 25±5 nN followed by a potential step. After increasing the tip-sample force, enhanced deposition was confirmed by the observation of larger features within the small window they were previously scanning. The localized rapid growth under the tip could be due to the removal or modification of a passivating oxygen adlayer

on the Cu surface. The role of the AFM tip is to disrupt this oxygen layer, creating active sites for Cu adsorption. Their work involved studying the influence of dissolved oxygen concentration, amount of Cu added and electrolyte anions. Among those, the tip-sample force was the critical factor initiating the enhanced deposition effect.

In our experiment, the tip-sample force was 0.12 ± 0.02 nN. In this study, the tip is brought into contact with the sample such that the imaging is performed with minimal possible force. The enhanced deposition was only observed in the regions where the HS-AFM tip was scanning. This could indicate that the tip-sample force could be getting modified as the surface height keeps changing then disrupting the passivating oxygen adlayer leading to faster growth.

4.6 Chapter discussion

HS-AFM was used for direct observation of the growth of a Cu film. This study enabled us to qualitatively and quantitatively understand the structural coarsening mechanism of the Cu polycrystalline film. This work focused on the later growth stages of the Cu film.

Qualitative data comes from carefully looking at the images generated by the HS-AFM. The results obtained were:

(1) Accelerated local growth of certain grains and grain overgrowth. This was observed at different locations in the same film shown in figure 4.6 and 4.8. This growth pattern led us to propose a structural coarsening model that involves slope changes in grains during growth and grain overgrowth.

(2) Quantitative information comes from finding the roughness through scaling analysis at different deposition times given in figure 4.9. Slope analysis confirmed an increasing local slope θ with increasing deposition time as shown in figure 4.11.

(3) The HS-AFM study affirmed the conclusion of earlier work that the AFM tip has significant effects in enhancing local deposition. The tip-enhanced growth can be seen in figure 4.15.

Topographical information is insufficient to conclude that the non-uniform grain growth is caused by microstructural features. In situ, observation of Cu deposition at a high growth rate ($\approx$ 0.5nm/s) was achieved through this study. The observation of grain coarsening of a polycrystalline

Cu film at a high growth rate has never been done before using in-situ HS-AFM.

4.7 Chapter Summary

In situ HS-AFM was used to observe the growth of Cu film in real time to understand how the surface morphology evolves during growth. HS-AFM can scan several microns of an area within a few seconds at high resolution. A microelectrode of diameter 30 μm served as the working electrode, ensuring good mass transport while using a small volume of electrolyte. The study revealed details on how certain grains grow faster than others. We established that the non-uniform grain growth could contribute to the structural coarsening of a thin film. Scaling and slope analysis were in good agreement with the non-uniform grain growth pattern. We also observed that the AFM tip can enhance the local deposition rate. In future studies, HS-AFM has the potential to reveal new information about the growth mechanism of thin films when combined with microstructural information.

PULSED ELECTRODEPOSITION OF CU

I n this chapter, electrodeposited Cu films are produced using pulsed electrodeposition (PED). The form of PED studied here involves repeatedly switching the potential between a cathodic and open circuit potential (OCV). Cu deposits produced by employing PED grew special hexagonal features that are found to be linked to structures known as nanotwins in other studies[107]. (111) Textured nanotwinned Cu (nt-Cu) has attracted wide interest due to its superior mechanical and electrical properties. Usually, there is a trade-off between strength and ductility: for ultra-high strength, ductility is sacrificed and vice versa[110]. This can be eliminated by growing desirable structures like coherent nanotwins[111, 112, 113]. The remarkable strength originates from the twin boundaries (TBs) effectively obstructing the motion of dislocations[114, 115].

With the miniaturization of electronic and semiconductor devices, there is a demand for the reduced dimension of Cu interconnects. Reduction in the dimension of Cu interconnects involves the manipulation of its microstructure, especially grain size. One way to reduce grain size is by grain refinement. This introduces more GBs and they act as a barrier for dislocation motion, providing resistance to plastic deformation, and improving the strength of the material. The introduction of more GBs can also deteriorate the conductivity by scattering electrons. One way to improve the material strength without reducing the conductivity is by preparing materials

with high-density TBs[116]. They can effectively block dislocation motion improving mechanical strength and reducing electrical resistivity by one order of magnitude lower than the scattering from the incoherent high-angle grain boundaries (GBs)[117]. Electromigration(EM) can adversely affect Cu interconnects due to high-angle GBs from ultra-fine grains causing the formation of voids. High-resolution transmission electron microscopy (HRTEM) by Chen et al. on grain boundary-modified copper film prepared by electron beam evaporation exhibited a reduction in the electromigration-induced atomic diffusion at triple points. A triple-point is where a TB meets a GB. According to their study, a long incubation time is needed for the nucleation of a new step at the triple point that arrests the EM-induced atomic transport process[118]. This can lead to improvement in the reliability of Cu interconnects by suppressing the electromigration effects. Thus nt-Cu could act as an excellent candidate for manufacturing advanced integrated circuit devices[119]. The surface and microstructural properties of the nt-Cu can be manipulated by changing the parameters involved in PED especially applied potential[120].

In our study, PED was used to prepare twinned Cu films. The influence of overpotential on grain size is studied. Local slope analysis was performed on AFM images of the Cu films and the slope distribution of twinned Cu films deposited at different potentials compared to coarse Cu films was studied. For microstructural information, FIB and XRD measurements were carried out on a twinned Cu film. A possible growth mechanism of the hexagonal columns driven by screw dislocation is briefly discussed.

5.1 Theory of Pulsed electrodeposition

Apart from DC electrodeposition, pulsed electrodeposition (PED) is another approach to produce thin films with nanocrystalline texture or to prepare alloys. A potential/current is applied as a function of time and is usually switched between two different values. The three characteristic parameters of pulse electrodeposition are pulsing potential/current, T_{ON} and T_{OFF} times. The time duration when the potential/current is applied is called the T_{ON} period and T_{OFF} is when the potential/current value is made to zero. Figure 5.1 represents a square waveform distinguishing the three different parameters. The value of these variables can be independently
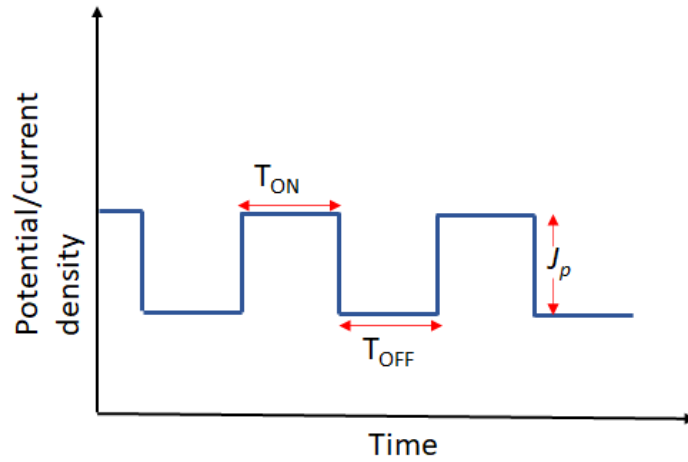
FIGURE 5.1. Typical square waveform with fixed pulse potential or current density.

chosen to produce deposits of sought-after properties. PED can produce high instantaneous current densities and hence a high overpotential by replenishing the metal ions during T_{OFF} time[121]. Charging the electrical double layer at the electrode-solution interface and mass transport are the limiting factors during pulse electrodeposition.

In order to raise the potential across the double-layer capacitor at the electrode-electrolyte interface, the charge must be provided. T_{ON} must be always chosen to be longer than the charging time of the capacitor. Similarly, T_{OFF} must be longer than the discharging time. If the charging and discharging times of the double-layer capacitor are longer than the pulse length, the faradaic current produced during the deposition(T_{ON}) does not reach the value of the total current during the T_{OFF} time, the faradaic current never drops to zero. In this limit, the situation approaches DC electrodeposition [122]. The time scale for double-layer charging can vary from ms to μs. However, the exact time depends on the applied potential at the electrode-electrolyte interface.

5.1.1 Mass transport: Duplex diffusion layer

When pulses are applied to the electrode surface, the concentration of reactants pulsates with the frequency of the applied pulsating potential. This pulsating layer is called the inner diffusion layer and has a thickness δ_{pp}[123]. A sharp concentration gradient develops during the pulse ON time in δ_{pp}. If the applied pulse is short, this diffusion layer does not extend to the bulk of
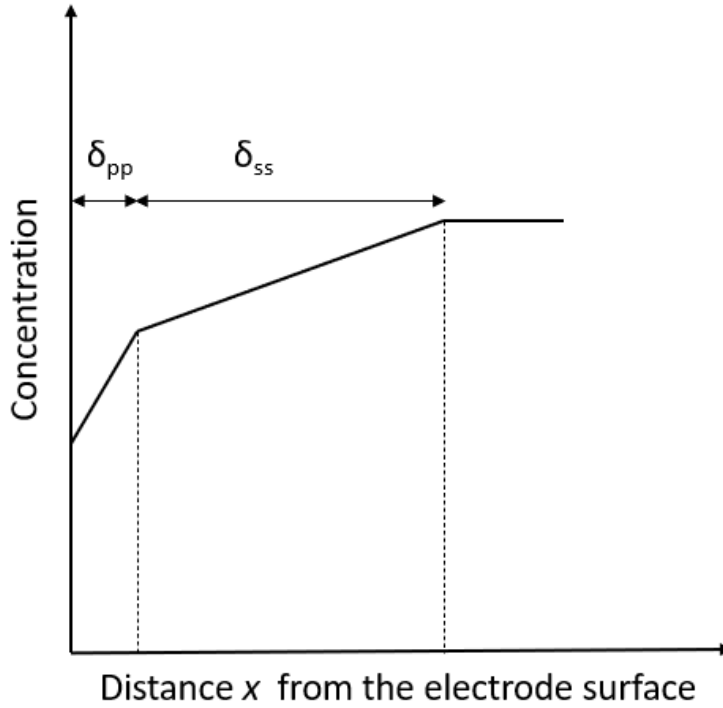
FIGURE 5.2. Schematics of the concentration profile of the two diffusion layers. In reality, there is no discontinuity in the gradient of the concentration.

the electrolyte solution. In order to transport reactants from the bulk towards the inner diffusion layer, a second diffusion layer called the outer steady-state diffusion layer with thickness δ_{ss} develops[123]. The concentration gradient in this diffusion layer extends to the bulk of the solution. Figure 5.2 shows the concentration profile of the two diffusion layers developed during pulse electrodeposition. During the OFF time, the reactants will diffuse from the bulk towards δ_{pp} due to δ_{ss}. Thus the concentration gradient developed during the ON time relaxes.

The pulse limiting current is defined as the maximum current when the concentration of reactants at the electrode surface reaches zero by the end of a pulse. During pulse plating, the reactant at the electrode surface is still supplied from the bulk of the solution. Hence the pulse limiting current density in the presence of pulse diffusion layer is given by [123] :

$$i_{\text{ppL}} = \frac{nFDC_\infty}{\delta_{\text{pp}}} \tag{5.1}$$

During the OFF time of the pulses, the reactant species are supplied from bulk by diffusion across δ_{ss} indicating that the pulse limiting current is always less than or equal to DC steady

67

state limiting current conditions. The duty cycle in PED corresponds to:

$$\text{duty cycle } = \frac{T_{\text{ON}}}{T_{\text{ON}} + T_{\text{OFF}}} \tag{5.2}$$

When the duty cycle is low, the current j_p must be high to match DC deposition rates. The value of the duty cycle is chosen carefully to avoid approaching the DC conditions.

The microstructural features of metallic deposits can be controlled by PED. For example, grain refinement can be achieved to produce better coatings compared to DC because of the high nucleation rate. PED offers three independent parameters that can be modified to obtain films with desired composition and porosity[124, 125, 126]. PRC(Pulse Reverse Current), a variant of the PED technique, switches alternatively between cathodic and anodic pulses. PRC can be utilized to dissolve away asperities on a surface to produce uniformly coated deposits. PED and PRC can produce alloys with improved properties like low residual stress and superior mechanical properties[127, 128, 129].

5.2 Experimental details

For PED, an electrolyte solution consisting of 0.01M $CuSO_4$+0.1M H_2SO_4 was used. A planar Au substrate of dimensions 1cmx1cm served as the WE. As a preliminary study before conducting in-situ HS-AFM experiments on microelectrodes, pulsed deposition was carried out on planar electrodes. Compared to microelectrodes, planar electrodes are easier to prepare. Therefore, as a starting point for investigating the deposition potential, T_{ON} and T_{OFF} times during pulsing, planar electrodes were the best choice before moving to microelectrodes.

A Cu strip acted as the RE and a Cu sheet, much larger than the WE served as the CE. The sample holder contained a Luggin capillary to ensure a constant distance and close proximity between the working and reference electrodes. Figure 5.3 represents the CV performed on a planar electrode. The sudden increase in the current after the current plateau is due to hydrogen evolution as the potential is increased to a higher value. Figure 5.4 shows the square pulses and the parameters used for the experiments. A T_{ON} time of 2.5s and T_{OFF} time of 10s was chosen for all the experiments. During T_{ON} a pulse or potential of duration 2.5s is applied to the WE and during T_{OFF} time the potential is switched to OCV (open circuit potential) for 10s. OCV is
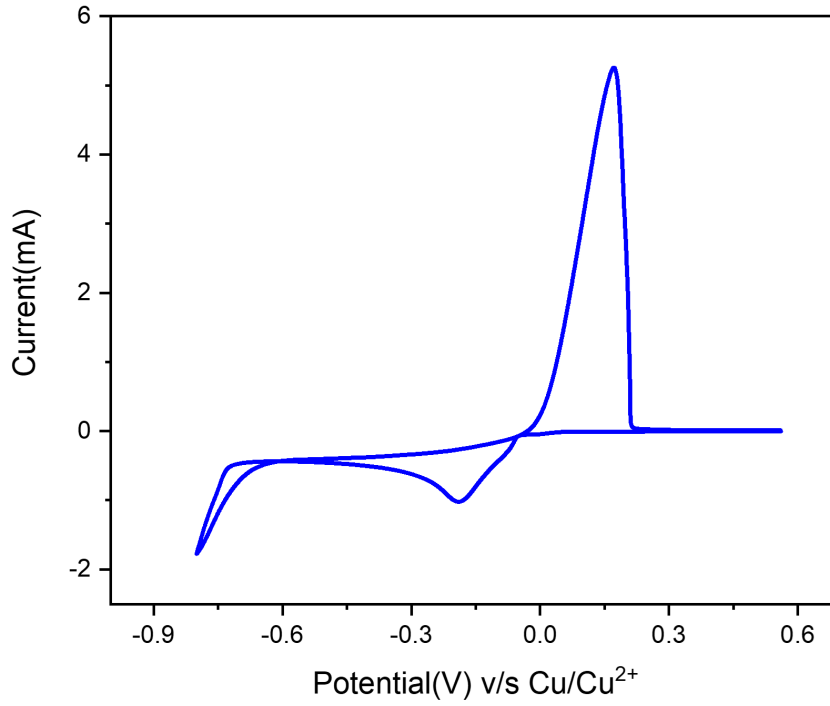
FIGURE 5.3. CV performed on a planar electrode at a scan rate of 20mV/s.
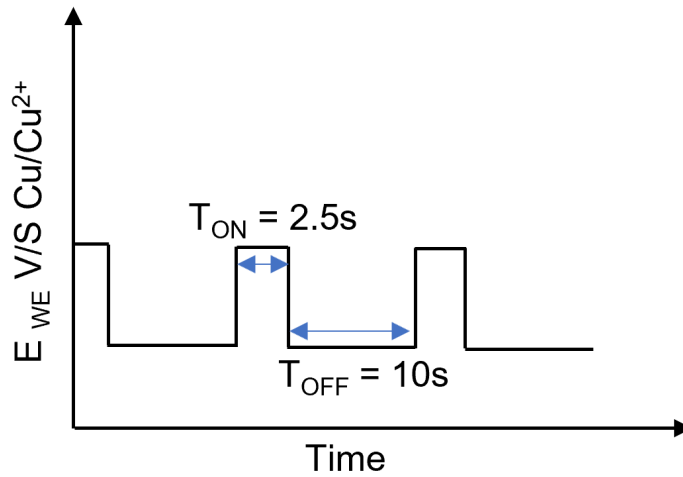
FIGURE 5.4. The square waveform with fixed potential. Here the T_{ON} = 2.5s and the T_{OFF} = 10s.

the potential measured when no current is flowing through the cell. The deposition is expected to take place only during the T_{ON} time. For all the experiments, the T_{ON} duration was 2.5s and

T_{OFF} duration was 10s. The ON and OFF time was chosen such that the films deposited under these conditions produced hexagonal pyramids on the surface. T_{ON} = 2.5s and T_{OFF} =10s time for different deposition potentials produced films with desired features which are hexagons in our case. The applied potential was changed to produce different Cu films of similar thicknesses. The surface morphologies of the deposited films were investigated afterwards using AFM and SEM.

5.3   Grain area determination using watershed algorithm

The surface of the pulsed deposited film was imaged using AFM. These images can be analyzed to locate grain boundaries and hence determine the grain size. In this thesis, watershed segmentation, a classical algorithm was used to determine the grain area from the AFM images.

Software like Gwyddion can be used to perform the same functions. The main drawback is that they fail to work on specific complex topographies and often fail to identify grains that are very small. Figure 5.5 shows such an example where the Otsu algorithm in Gwyddion was unable to recognize all the individual grains. Edge detection was implemented to locate the grain boundaries in the AFM images. This algorithm fails to recognize corners if a Gaussian filter is applied to the image. The images pass through a Gaussian filter to remove any unwanted details or noise in the image. This can blur the edges and make it difficult for Edge detection to detect grain boundaries. These issues have been overcome by implementing a watershed segmentation algorithm[130]. It is most accurate compared to other algorithms and gives the flexibility to perform various statistical analyses on the output data. The principle of this algorithm is simple. It starts from a user-defined marker. Our marker was the local maximum within an individual grain. The local maximum is the maximum value of pixels within a well-defined distance. The algorithm considers the pixels as the local elevations. This method "floods" valleys from the markers and moves outwards. This continues until the valleys of different markers meet each other. The region where they meet is considered a grain boundary. Figure 5.6 shows the grains identified by the watershed algorithm from the AFM image in figure 5.6a.
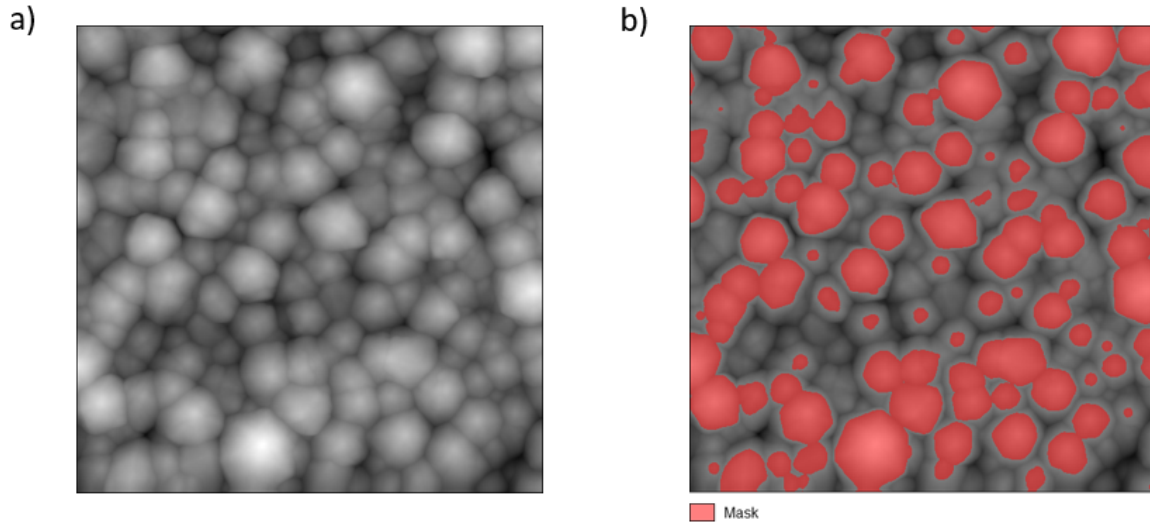
FIGURE 5.5. a) AFM image of a Cu film b) The red represents the mask over the grains identified by the Otsu algorithm in Gwyddion on the AFM image. It fails to identify all the grains in the AFM image.
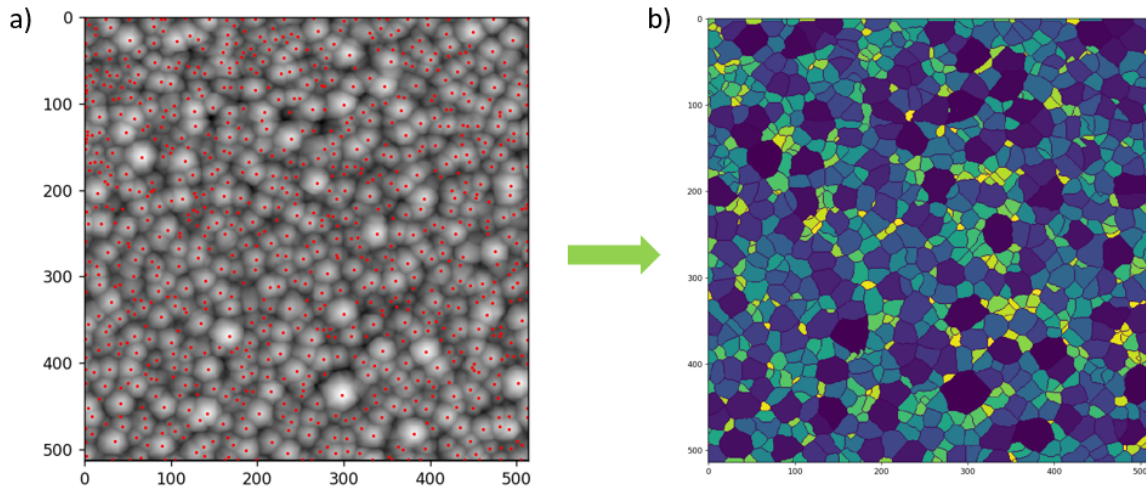
FIGURE 5.6. a) The AFM image of the pulsed Cu film with the local maxima marked in (•) identified for each grain b) AFM image after the watershed algorithm recognized the grain boundaries. Each individual grain has its own grain boundary and uniform colouring.

5.4   Grain area analysis of the Cu films deposited at different potentials

Electrode potential is known to influence the grain size of electrodeposited films. To investigate this, Cu films were pulse deposited following the protocol mentioned in section 5.2. The electrode potentials were -650mV, -612mV, -550mV and -300mV. All potentials are reported against Cu/Cu^{2+} reference electrode. In order to calculate the grain area, the surface of the Cu films needs to be imaged using an AFM. While imaging the sample using AFM, different locations on the sample were imaged to ensure uniformity. The AFM scanned an area of size 10x10μm with a pixel size ≈ 20 nm (scan size\number of pixels = 10μm/512). Figure 5.7 shows the AFM images of pulse-deposited films at different potentials.

Grain size is a function of film thickness, so all the films were grown to a thickness of $\approx 1.3\mu$m determined using a profilometer. The grain areas of each film were calculated from the AFM images using the watershed algorithm. Figure 5.8 shows the histograms of grain area at different potentials.

Total area is the sum of the area of all the grains within a range of values of the grain area. The histograms are fitted using the gamma distribution. Its probability distribution function[131] of the random variable X is:

$$f(x) = \frac{1}{\Gamma(k)\theta^k} x^{k-1} e^{-\frac{x}{\theta}}$$ (5.3)

$\Gamma(z)$ is defined as:

$$\Gamma(z) = \int_0^\infty t^{z-1} e^{-t} dt$$ (5.4)

where k and θ are known as the shape and scale parameters respectively. The cumulative distribution function is plotted for all potentials against grain area in figure 5.9. Table 5.1 shows the mean value of the grain area for each potential obtained by fitting the histogram using the Probability Density Function (PDF) of the gamma distribution.

From figure 5.7 it is clear that each of the Cu film surfaces looks very different from the other. Comparing Figures 5.7a and 5.7d, the Cu film deposited at -650mV has bigger, compact grains. From the histograms, in figure 5.8 and table 5.1, a clear trend of grain area increasing
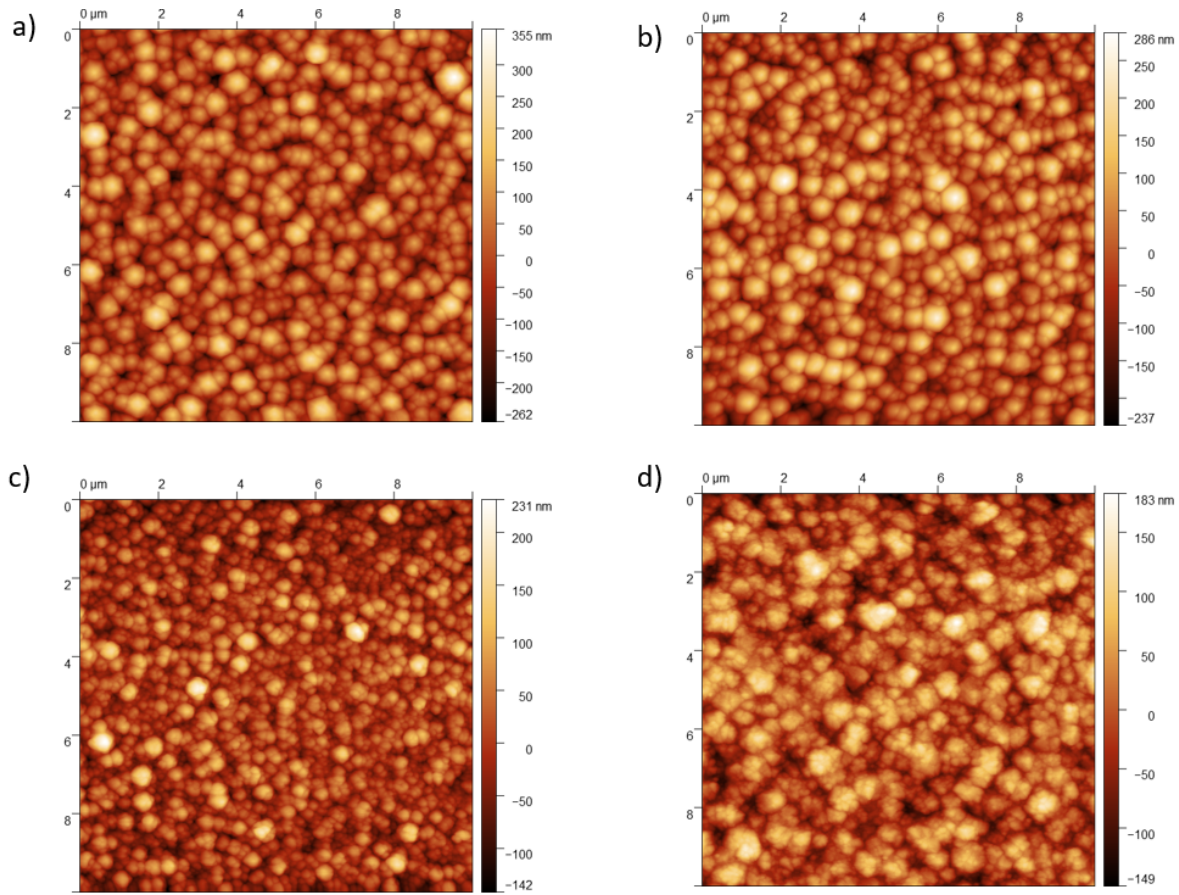
FIGURE 5.7. AFM images of pulse deposited Cu film at different potentials a) -650mV b)-612mV c)-550mV d)-300mV. All potentials are reported against $Cu\backslash Cu^{2+}$ reference electrode.

Electrode Potential(mV)	Mean area(μm^2)
-650	0.23
-612	0.23
-550	0.12
-300	0.08

Table 5.1: Electrode Potentials and their corresponding mean grain areas are calculated by fitting the distribution using equation 5.3.

with increasing electrode potential can be observed. From the CDF in figure 5.9 the grain area distribution of -550mV and -300mV is limited to a small range of grain area values, whereas -650mV and -612mV have grain area distribution over a broad range.

Other studies have observed that with increasing current density the grain size decreases. A study by Lui et al. involved pulsed current deposition of Cu from 0.5M CuSO$_4$ solution by
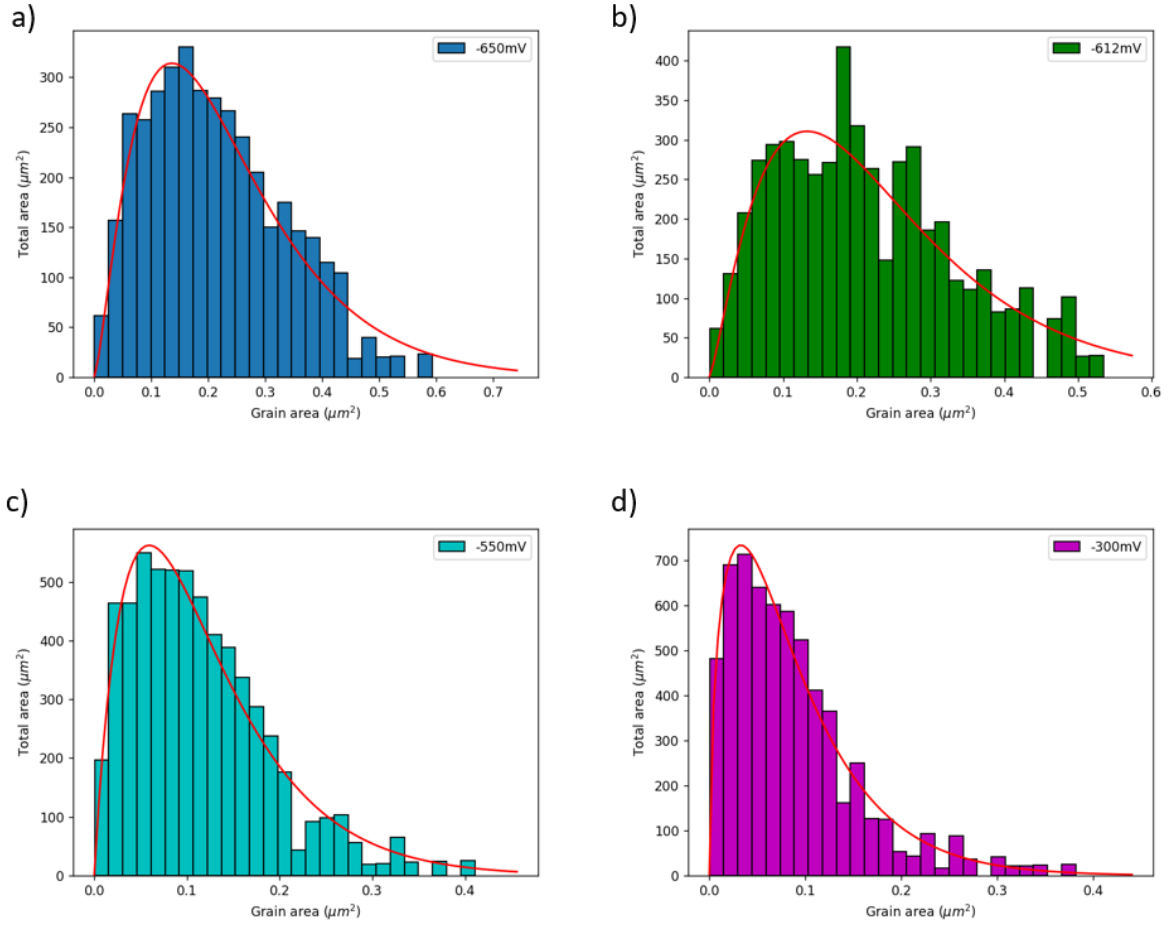
FIGURE 5.8. The grain area distribution of Cu films electrodeposited at different electrode potentials a) -650mV b) -612mV c) -550mV and d) -300mV. The histograms are fitted using equation 5.3.
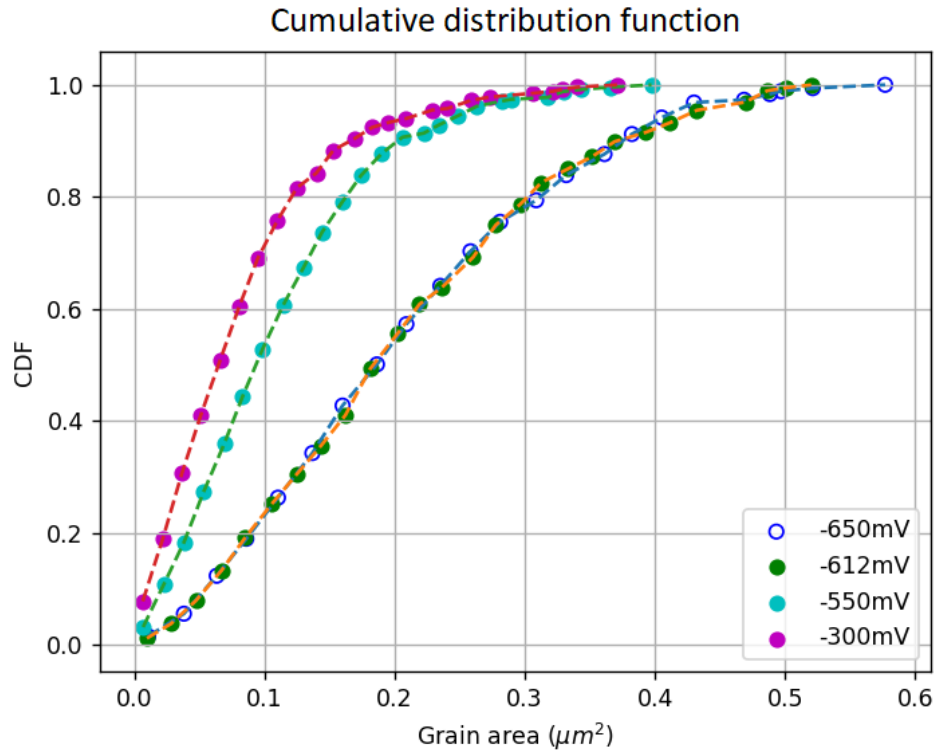
FIGURE 5.9. The cumulative distribution function of grain area of Cu films deposited at different potentials.

varying the current from $0.25 Acm^{-2}$- $1.50 Acm^{-2}$[132]. Meanwhile, a study by Xue et al. involved increasing the current density during direct current copper deposition, using a rotating disk electrode[133]. Both studies observed a decrease in grain size with an increase in current density. This behaviour could be attributed to the increase in nucleation rate with an increase in overpotential [53, 134]. Increasing the current density results in increased cathodic polarization leading to higher nucleation rate[132]. In our studies, the contrary is observed. The grain area has increased with increasing overpotential. Certain studies also addressed the trend of grain size getting larger with high overpotential[135]. Ge Yi was able to switch from polycrystalline growth to single crystalline growth of Pb nanowires by applying higher overpotentials. They claim that it's energetically favourable to form epitaxial clusters that coalesce into a single crystal forming bigger grains than forming a nucleus with a different orientation. The energy penalty for the misorientation could be much bigger compared to growing an epitaxial grain[136]. However, it is

75

crucial to point out that the above-mentioned studies are carried out at a higher concentration of reactants ($\geq$ 1M) so that the deposition is not limited by the mass transport of materials towards the electrode.

A polycrystalline film growth proceeds in two ways[137]: (i) either by the formation of new nuclei or (ii) by the growth of the existing crystals. These two processes compete against each other. Process (i) requires high overpotential, a high adatom population and a low surface diffusion rate and vice-versa for process (ii). Surface diffusion of adatom, unlike overpotential\adatom population, can't be controlled by changing the electrical parameters involved in the experiment[137]. unless the adatom retains a partial charge. It is a physical attribute of the adatom and is influenced by the presence of adsorbed species on the electrode surface. High overpotential and replenishing of reactants during T_{OFF} time can lead to a high population of adatoms on the surface during the pulsed deposition which in turn promotes a higher nucleation rate forming a large number of small nuclei. In our case, the concentration of reactants in the electrolyte solution is very low (10mM). If a high overpotential like -650mV is applied when the concentration of the reactants is low, then the kinetics of electron transfer will be very high, while the mass transport of reactants to the electrode surface is slow and it becomes the rate-limiting step. The initial part of the T_{ON} time during pulse may not be limited by mass transport, but with time the concentration of reactants reduces leading to a low adatom population, promoting the growth of existing crystals by incorporating adatoms to them rather than nucleating new ones. The incorporation of adatoms is favoured if the diffusion rate is high towards the terraces of the 'hexagons' at higher potentials. This could explain the increase in grain area with an increase in overpotential. From figure 5.9 the grain area of -650mV and -612mV looks very similar to each other. The reason for this could be that both the electrode potentials lie close to each other in values. Hence the areas of the grains are not much different from each other.

5.5 Investigating the morphology and microstructure of nt-Cu films

The morphology of pulsed electrodeposited Cu films is very different from DC electrodeposited Cu films. Other studies have revealed that the pulsed deposited Cu films exhibit twinned structures. These nt-Cu (nanotwinned Cu) films show a hexagonal pyramid-like geometry. In order to confirm the presence of hexagonal structures, the surface of the films was imaged using AFM first. To confirm the hexagonal structures are indeed twinned Cu, the microstructure of the film is investigated using the FIB technique.

As the Cu film gets thicker, the grain size gets larger, and the surface roughness increases. The limitation of the AFM is the inability to scan very rough films. The AFM images used here are of rather smaller thickness measuring 1.3μm. By passing the AFM images through a Laplacian filter, the hexagonal features are enhanced, showing the finer details of their grain boundaries. Figure 5.10 shows the AFM images and subsequent Laplacian filtered images of the Cu film, with or without hexagonal pyramids. In figure 5.10 some of the hexagonal structures are identified and marked in black circles. In figure 5.10b, the Laplacian filter reveals a large number of smaller grains that don't exhibit the hexagonal pyramid-like geometry. The other way to confirm the existence of the twinned Cu is by looking at the underlying microstructure. It is important to examine the crystallographic orientation of Cu films. XRD measurements were carried out on the four different Cu films deposited at different potentials. Figure 5.11 shows the intensity v/s 2θ plot of the film. It can be inferred that all the films exhibit a strong (111) texture, with -550mV and -300mV having a weak (200) texture along with a strong (111) orientation. Nanotwinned samples with or without the hexagonal sixfold symmetry prefer (111) orientation[132]. The (111) surface has the lowest surface energy compared to the other principle low indices planes[138]. This is due to the close-packed structure of (111) planes compared to other atomic planes.

The origin of these nanotwinned structures is still an ongoing study. Two different mechanisms are proposed for the generation of the twinned structures. One is stress relaxation during T_{OFF} in the pulse deposition. The second mechanism claims that the twinned structure originates from screw dislocations. At microscopic levels, real crystal surfaces are not perfect, as they contain
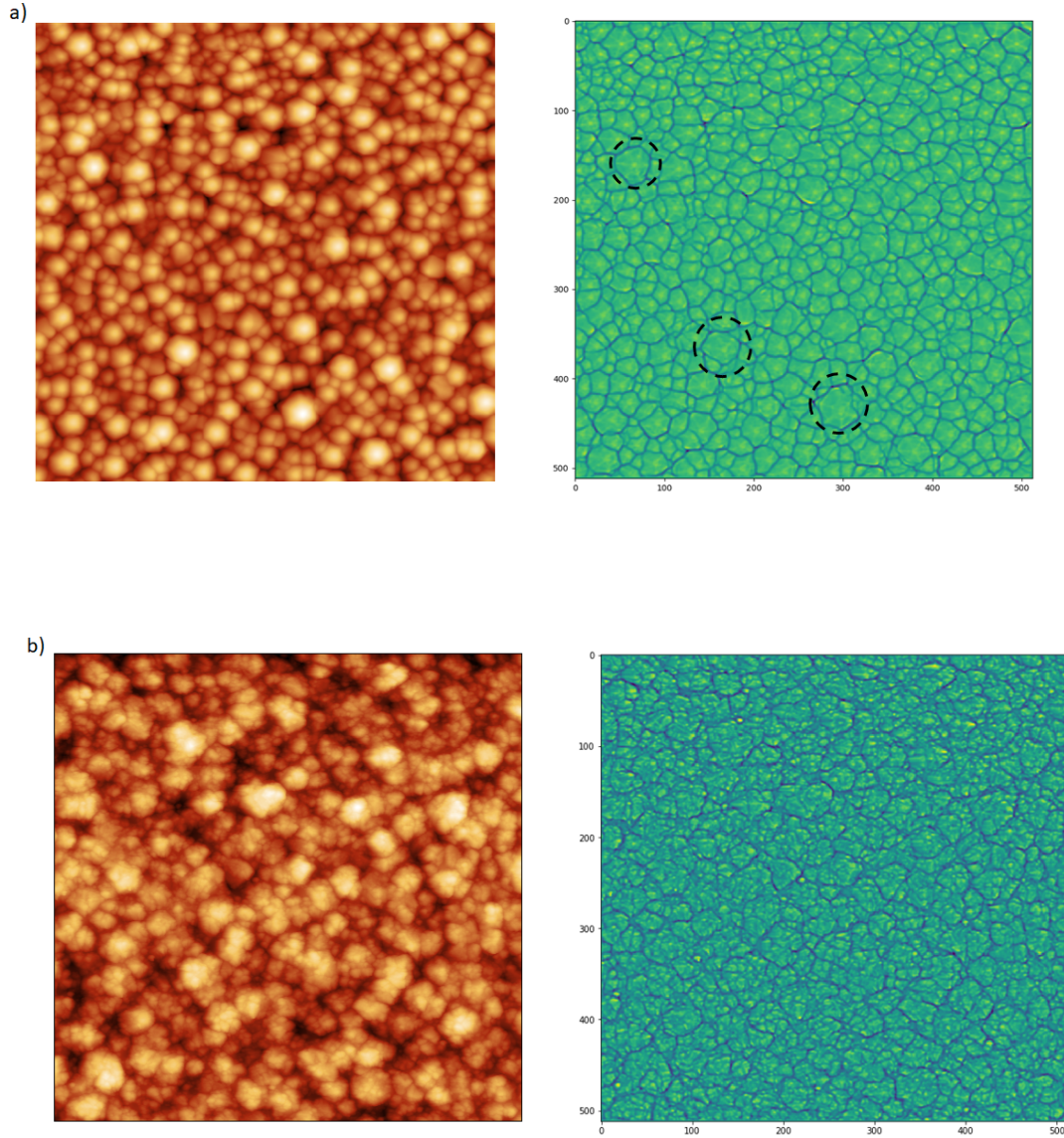
Figure 5.10: AFM images and their corresponding Laplacian filtered images a) AFM image of Cu film deposited at -650mV and its corresponding Laplacian filtered image (right). Few of the hexagonal structures are marked in the filtered image b) AFM image of Cu film deposited at -300mV and its corresponding Laplacian filtered image (right).

structural defects. Screw dislocations are very common in solid surfaces, including the surfaces of single crystals. Screw dislocations are formed by the displacement of atoms, creating an edge
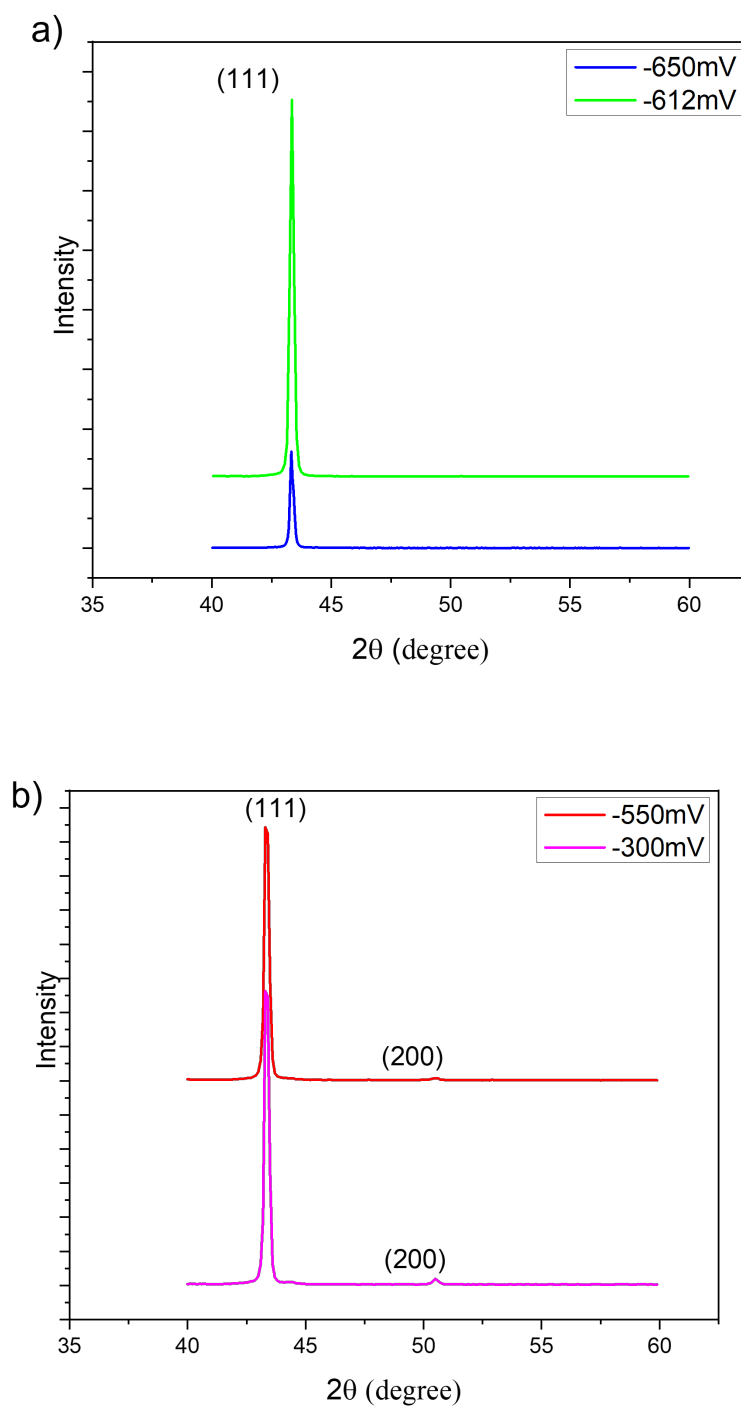
FIGURE 5.11. XRD $\theta - 2\theta$ measurements of samples deposited at different potentials a) XRD plots of -650mV and -612mV b) -550mV and -300mV. The thickness of the films was ~ 1.3 μm.

where adatoms get incorporated. This edge then propagates and winds itself to form a pyramidal cone-like feature.

As a preliminary study, the FIB becomes a useful tool to look at the microstructure of the twinned film. The principle of working of FIB is described in section 3.9. It is necessary to use a
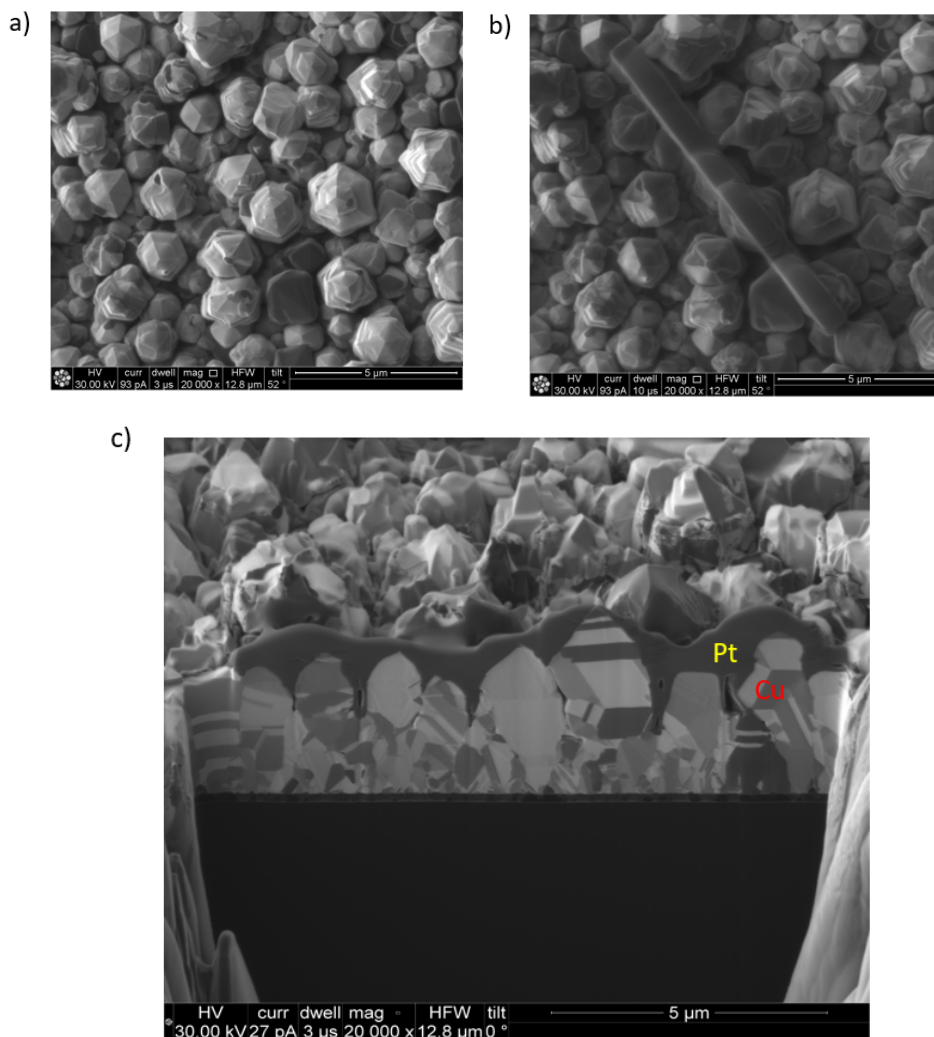
FIGURE 5.12. The twinned Cu film before and after FIB milling a) top-view of the twinned Cu film showing hexagonal pyramidal grains b) A strip of Pt laid on top of the region of interest as a protective layer c) Cross-sectional image of the FIB milled sample showing horizontal lamellas.

thick film to ensure the grains are big enough for the SEM to resolve and give a distinguishable grain contrast. For FIB measurement a Cu film pulsed deposited at -550mV with respect to a Cu\ Cu^{2+} reference electrode according to the conditions explained in section 5.2 was studied. The
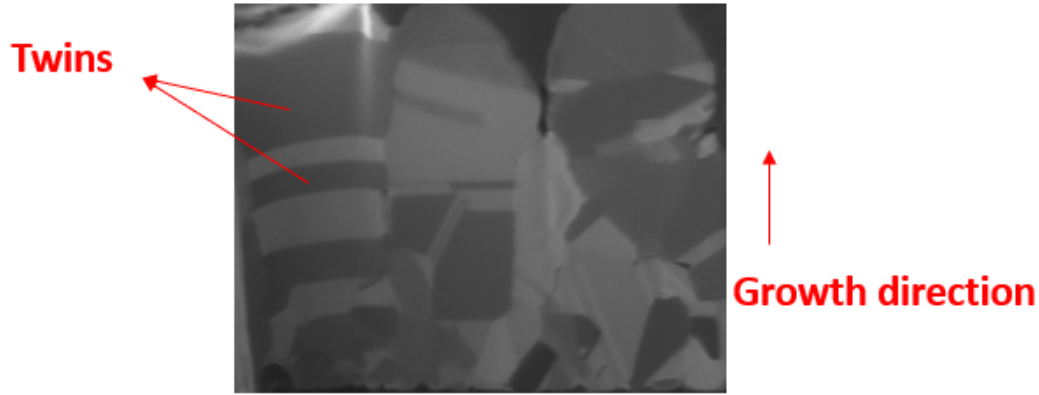
FIGURE 5.13. High magnification image of horizontal twins growing perpendicular to the growth direction.

film was deposited for 7 hrs. The thickness was determined to be 4.1μm measured using SEM. Figure 5.12 shows the twinned Cu film surface before and after FIB milling. In figure 5.12 the top view of a selected region of the film surface is shown. It is clear from this image, the grains have a hexagonal symmetry with step-and-terrace morphology. In figure 5.12b, a strip of Pt is laid on top of the few selected hexagons as a protective layer against the bombarding Ga$^+$ ions. Figure 5.12c shows the cross-sectional FIB milled twinned Cu film. The top Pt and bottom Cu layers are marked. FIB is a great tool to view specimens that exhibit grain orientation contrast. The channelling of the incident ions between the lattice planes of the Cu film gives rise to the grain orientation contrast in FIB measurements[139]. This means that the secondary electrons escaping from grains with different orientations appear in different contrast[139]. Figure 5.12c reveals several grains with a band-like structure running along the entire length of the grains. The step-and-terrace morphology corresponds to the bands appearing in the cross-sectional image in figure 5.12c, suggesting the existence of twin structures. Depending on the deposition conditions two orientations for the twin planes relative to the direction of growth have been reported. Studies have reported twinned Cu to be horizontally oriented or vertically oriented with respect to the growth direction[120]. From figure 5.12c, the twin lamellas are horizontally oriented perpendicular to the growth direction. Different types of TBs and other defects are also

81

visible from the FIB images. In some columnar grains, TBs don't traverse the entire length. Figure 5.13 is a selected region from figure 5.12 showing the horizontal twins growing perpendicular to the growth direction. Hasegawa et.al reported vertical steps interconnecting different TBs in pulsed deposited Cu films. TEM study by them showed that these structures are vertical stacking faults[120].

5.6   Slope analysis on twinned Cu films

The concept of slope analysis is discussed in section 2.8. The same concept can be applied to determine how the local slope θ varies as a function of distance from the centre of the hexagonal structures towards the grain boundary. Most data on twinned Cu is qualitative, but the slope analysis can give a quantitative description of their slope. This is the first time a quantitative study on the slope of the twinned structures has been attempted. To calculate the slope as a function of distance from the centre of hexagons, the Euclidian distance of a point within the hexagon from its centre is calculated and its corresponding slope is acquired. In two dimensions, the distance between two points p with Cartesian coordinates (p_1, p_2) and q with Cartesian coordinates (q_1, q_2) [140] is:

$$d(p,q) = \sqrt{(q_1 - p_1)^2 + (q_2 - p_2)^2} \qquad (5.5)$$

This Euclidian distance will be calculated in the number of pixels from the centre of the hexagon. Figure 5.14a shows a high magnification image of one of the hexagons recognized by an algorithm that can detect the local peak maximum from the AFM image and figure 5.14b shows a complete AFM image with all the hexagons identified marked as (●). Slope analysis will give an insight into the surface morphology of the faceted hexagonal structures. It is useful to compare the variation in slope when the potential is varied. For the slope calculation, two different potentials were considered -650mV and -612mV, as these films exhibited unique hexagonal morphology. From figure 5.7, it is clear that -650mV and -612mV produced compact hexagonal pyramids. The local slope θ of analysis of selected hexagonal pyramids was attempted. Figure 5.15 shows the slope θ v/s distance plot. From figure 5.15, it can be inferred that the maximum slope of -650mV is higher than -612mV. 3D plots of one each of the selected hexagons deposited at -650mV and
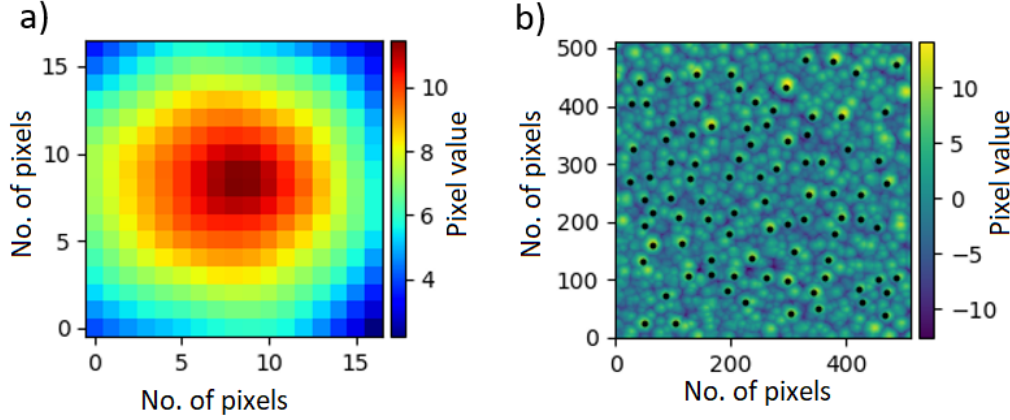
FIGURE 5.14. a) A single hexagon b) All the hexagons identified by the algorithm are marked for slope calculation.

-612mV are given in figure 5.16. It can be seen that the -650mV sample has a steeper surface than the -612mV one. In figure 5.12 faceted hexagons can be seen from the top view.

From figure 5.8, it was clear that -650mV and -612mV have grains of comparable area, with -650mV deposited film having grains slightly bigger than -612mV. The slope analysis suggests that bigger hexagons have steeper or more vertical faces away from the apex than the smaller ones. If the top surface of the pyramids were a separate facet at the centre, the slope at the centre of the feature should be zero. However, there appears to be a non-zero value for the slope, indicating that the hexagons do not have faceted tops. If the hexagons were facetted, the slope should be fixed as a function of distance from the centre. Here the slope seems to be increasing towards the grain boundary away from the centre of the grain.

Slope analysis was also performed on AFM images of samples deposited at different potentials. Figure 5.17 shows the slope distribution for films grown at different potentials. The thickness of all the films was kept $\approx 1.3\mu$m. To study the effect of potential on the grain size variation, parameters like T_{ON}, T_{OFF} and film thickness were fixed. Also increasing the thickness further resulted in rough films which are difficult to image using AFM. So films of certain thickness exhibiting hexagon-like surface morphology were chosen for slope analysis. From figure 5.14, it is clear that the peak values of θ for each plot are shifting towards higher values. The peak value
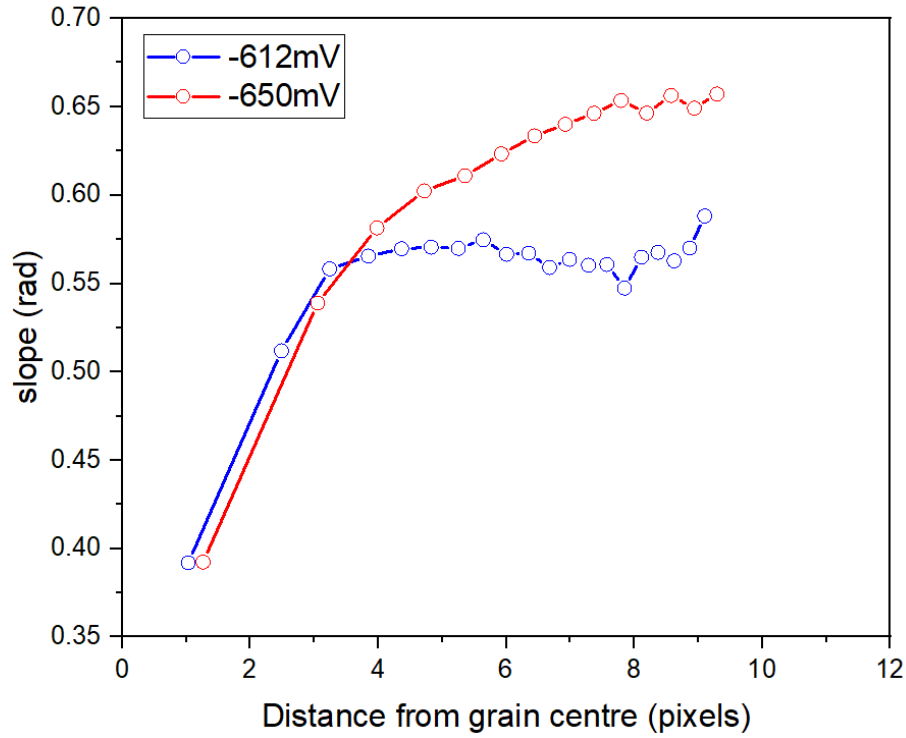
FIGURE 5.15. Local slope θ as a function of distance from the hexagon centre grown at different potentials -612mV and -650mV.

shifted from 0.32rad for -300mV to 0.64rad for -650mV. As the feature size increases, the slope also increases, the increase in grain area or feature size is consistent with table 5.1. Compared to other films the largest grains are seen in films deposited at -650mV and -612mv, showing hexagonal pyramid-like morphology. This difference is also observed in the slope distribution given in figure 5.17. From figure 5.17, the maximum value of the slope of the -650mV sample is larger than the -612mV one, very similar to the result observed in figure 5.15. Here the slope of the -650mV hexagons get larger than the -612mV hexagons as we move away from the centre of the feature. Both -650mV and -612mV have a distinctive slope distribution compared to studies conducted elsewhere[98]. Liu studied the slope distribution of galvanostatically deposited Cu films of various thicknesses[82]. The distribution curves were skewed with smaller peak values for local slope θ similar to the -300mV slope distribution in figure 5.14. The films with hexagonal pyramid-like morphology have higher values for slopes and a different shape which makes them distinguishable from non-twinned Cu films.

a)

-650mV

b)
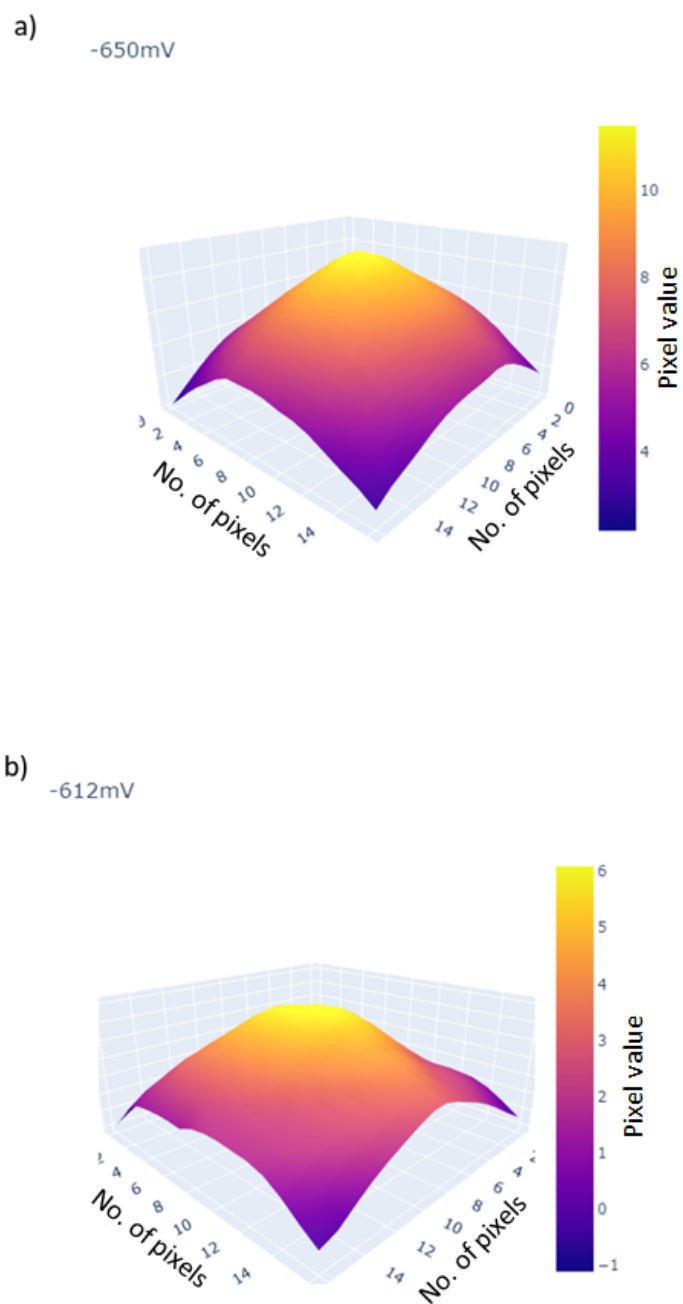
-612mV

FIGURE 5.16. 3D plot of single hexagons identified by the algorithm. These films are grown at a) -650mV b) -612mV.
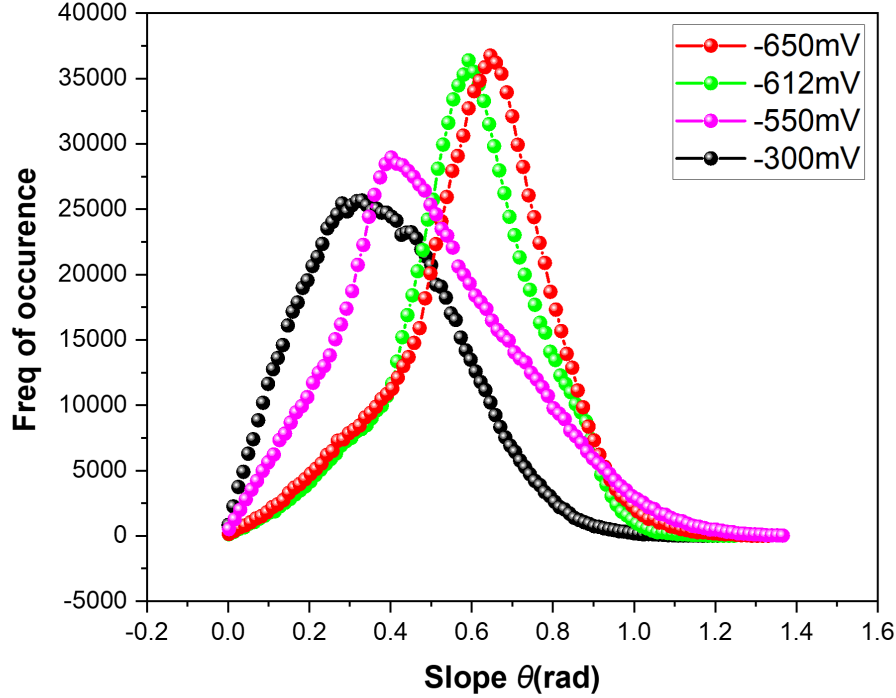
FIGURE 5.17. Local slope θ distribution for Cu films grown at different electrode potentials.

5.7   Hexagon growth mechanism

The high density of twins in Cu is a highly desirable structure as it could be the potential candidate for replacing non-twinned Cu deposits. The mechanism of the formation of twins has been studied by researchers intensively. Two different growth modes have been put forth as the possible mechanism that favours the growth of twins on Cu during PED, the stress relaxation during the T_{OFF} period of PED and screw dislocation-driven growth of Cu.

During electrodeposition, studies have shown that a thin film will go through compression-tension-compression stages[141, 142]. The initial compressive stage comes from the initial nucleation stage of growth due to developing surface stress in newly formed small nuclei. A rapid tensile stage takes place as the nuclei coalesce and form GBs. The thickening of the film generates the final compressive stage. According to first principle energy calculations, when the strain experienced by a thin film reaches a particularly large value, the total energy of the strained

FCC Cu system surpasses the total energy of the strain-free Cu nanotwin system[143], making this system energetically stable compared to the highly strained FCC Cu system. According to stress generation and relaxation theory, during T_{ON} time, applying a large current can produce a large number of nuclei. These nuclei coalesce and generate tensile stress. During the T_{OFF} time, the short-range atomic rearrangement of Cu clusters occurs by recrystallization[144]. Thus TB formation can lead to stress relaxation[144]. No new stress is generated during T_{OFF} time letting the already generated stress relax by forming the twins.

Other studies were able to prepare high density of coherent twins without pulse deposition, eliminating the stress generation and subsequent relaxation mechanism. In these studies, the key was using rotating disc electrodes (RDE) for DC deposition[133, 119]. In RDE, the electrolyte is rotated at the desired speed, and the concentration of redox species is controlled by diffusion up to a distance δ from the electrode surface and further away from the electrode surface is controlled by convection. The thickness of δ is controlled by the rotation rate of the electrode, the thinner the δ, the higher the concentration gradient[145]. The concentration overpotential can develop due to slowness in mass transport. The higher concentration gradient achieved in RDE drives faster mass transport towards the electrode surface, reducing the concentration overpotential. Similarly, in PED the concentration overpotential can be lowered due to the replenishing of the redox species during the T_{OFF} period.

The second mechanism that gives rise to hexagonal copper features could be the screw dislocation-driven growth of Cu. According to BCF(Burton, Cabrera and Frank) theory[146], when a screw dislocation emerges on the surface, self-perpetuating monosteps are present at that point. These steps self-advance by incorporation of atoms. They can wind themselves into a spiral which rotates itself around the dislocation. Several studies have observed the hexagonal pyramid-like growth of Cu and attributed it to spiralling screw dislocations[147, 148]. Screw dislocations has been seen on copper surfaces grown from $CuSO_4$(1mol dm^{-3})+ H2SO4(1 mol dm^{-3}) under pulsed current conditions[145]. A pulsed current study by Damjanovic on copper single crystals exhibited a hexagonal pyramid-like structure on (111) planes[104]. In our studies, it was interesting to see that as the thickness of the pulsed Cu film increased, the hexagonal pyramids exhibit a 'flower-like' morphology. Figure 5.18 shows the SEM images of twinned Cu
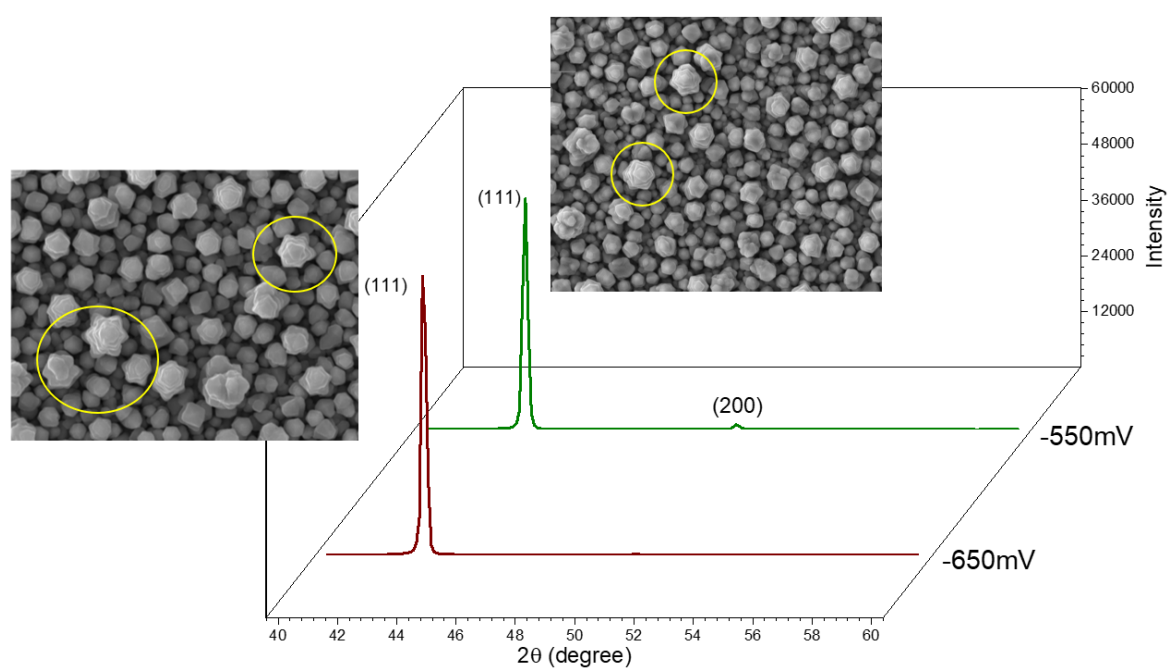
FIGURE 5.18. XRD $\theta - 2\theta$ measurement of Cu films exhibiting 'flower-like' morphology. SEM images of two samples with hexagonal grains showing 'flower-like' morphology marked in yellow circles. The thickness of -550mV film is $\sim 4.1\mu$m and the thickness of -650mV film is $\sim 2.5\mu$m.
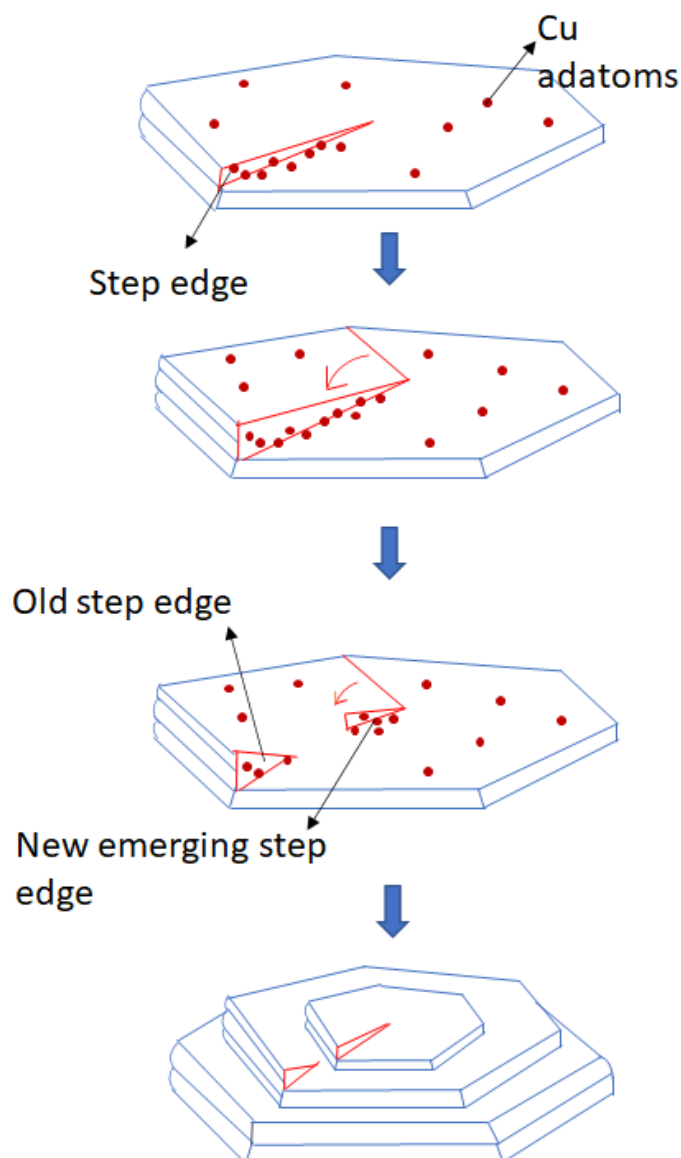
FIGURE 5.19. Schematic illustration of screw-dislocation driven growth forming the 'flower-like' morphology. A new step is formed and propagates, leaving the old step edge stagnant.

film with 'flower-like' morphology.

We propose a growth pattern, where a new screw dislocation develops on the topmost layer from the apex of the pyramid that contained the original screw dislocation. Figure 5.19 shows the illustration of how the 'flower-like' morphology can emerge. This new screw dislocation will have its self-perpetuating steps. XRD results indicate that the films exhibiting hexagonal pyramids and 'flower-like' structures have strong (111) textures as shown in figure 5.19. A screw dislocation

typically appears as the shearing effect of the lattice. Chen et al. describe how a screw dislocation can emerge when two grains meet and one grain is slightly uplifted near their GB, leaving atoms hanging on the uplifted edge[149]. Cu ions can then attach to the uplifted edge and grow to form a second extended layer creating a screw dislocation. The appearance of hexagons rather than irregular shapes is strong evidence of screw dislocation growth.

5.8   Mass transport effects

During our experiment, producing Cu films with hexagonal pyramids was challenging. Only a few Cu films out of hundreds of samples exhibited the desired features. All experiments were repeated using the same parameters and imaged using AFM. This inability to reproduce the results could be narrowed down to the presence of Cu ions in low concentrations in the electrolyte solution.

In electrodeposition, mass transport occurs through three different processes: diffusion, convection and migration. In our case, diffusion of redox-active species towards the electrode surface occurs as a result of a concentration gradient developing near the electrode surface. In PED, a high overpotential is applied during T_{ON} time. Meanwhile, during the T_{OFF} time the concentration gradient relaxes and the concentration of the redox active species is replenished. As discussed in section 4.4, the overpotential can be divided into three components, concentration overpotential, activation overpotential and incorporation overpotential[103]. The concentration overpotential develops when there is a concentration gradient. Since the concentration is replenished in the case of PED during the T_{OFF} period, the concentration overpotential is expected to decrease during the T_{ON} time. In PED, while applying a high overpotential, the electrodeposition may not be limited by mass transport at the very beginning of the pulse but later becomes mass transport limited as the deposition progresses. This can occur due to a decrease in reactant concentration at the electrode surface. During this period the concentration overpotential goes up and the overpotential is used to drive mass transport from the bulk instead of deposition. At the time of conducting our experiment, the reactant was present at a low concentration of 10mM. The high concentration overpotential produced due to the low concentration of ions could be the factor

affecting the reproducibility of certain results during our experiment. To achieve a very high incorporation overpotential during pulsing, the concentration of the reactant must be very high.

5.9 Chapter discussion

Pulsed electrodeposition was employed to deposit Cu films. The applied potentials used for PED varied from -650mV to -300mV. The morphology of the deposits was studied using the AFM and SEM. Careful analysis of AFM images revealed that:

(1) The Cu films exhibit distinctive hexagonal pyramid-like morphology when grown at high overpotentials.

(2) Grain area was calculated using the watershed algorithm. The influence of overpotential was studied on the grain area. It was observed that with increasing overpotential, the grain size also increases.

(3) Local slope analysis was performed on the AFM images of PED samples as well as on selected hexagons in the images separately. This is one way to quantitatively analyze the slope of facetted hexagons giving more insight into their surface morphology. Slope analysis on Cu films deposited at -650mV and -612mV showed a unique curve distribution with slope shifting towards higher values compared to Cu films deposited at lower overpotential. The local slope distribution can be observed in figure 5.17.

Local slope θ as a function of distance from the centre of hexagons revealed that the top surface of hexagons seems not to be facetted and the slope for hexagons formed at -650mV has higher values compared to hexagons formed at -612mV.

For microstructural characterization, XRD and FIB milling were performed on selected samples.

(4) XRD on thin and thick nt-Cu films showed that they have strong (111) texture which is in agreement with other studies. The XRD information of films deposited at different potentials is shown in figure 5.18.

(5) The results from FIB studies as shown in figure 5.12 revealed unique twinned structures with horizontal bands growing perpendicular to the growth direction. These bands could be due to a type of line defect called screw dislocations.

(6) SEM images of thick Cu films each deposited at different electrode potentials revealed hexagonal pyramids as well as a flower-like morphology. We attribute this hexagon formation to screw dislocation-driven growth mechanisms and propose a model for the growth of 'flower-like' grains on the surface as shown in figure 5.19.

The inability to reproduce films with hexagonal pyramids was a challenge in this study. This could be due to the low concentration of the reactant in the electrolyte affecting the mass transport of the reactive species towards the electrode surface. Using higher concentrations of reactant species would help reproduce results with a high density of nanotwins on the Cu surface.

5.10 Chapter summary

In our study, Cu films were electrodeposited by PED with a T_{ON} of 2.5s and T_{OFF} time of 10s. During the T_{OFF} time, the potential was switched to open circuit potential. The surface morphology of the films studied using the AFM revealed hexagonal pyramid-like structures on the Cu film surface. By examining the microstructure using FIB milling the hexagonal pyramids were confirmed as horizontal twins. The influence of overpotential on grain area was studied by pulse depositing Cu films at different electrode potentials. It was shown that high overpotential doesn't necessarily mean smaller grains. Local slope analysis on AFM images gave an insight into how the slope θ curve of films deposited at higher potential is distinguishable from the slope distribution curve of Cu films deposited at lower potentials. XRD as a complement to FIB milling suggested a strong (111) orientation for twinned Cu films. We suggest the growth of twins as a result of emerging screw dislocation and proposed a model for the formation of 'flower-like' morphology observed in thick Cu films.

CONNECTING THE SURFACE MORPHOLOGY AND MICROSTRUCTURE OF CU FILM

This chapter involves looking at the morphology and microstructure of electrodeposited Cu films grown on a microelectrode using AFM and EBSD techniques. The film is grown from a chloride-containing solution. Chloride is an additive used commonly in commercial electrolytes for applications like electroforming and superconformal filling of vias and trenches in the damascene process[150]. Anions like chloride have the ability to affect the kinetics of Cu electrodeposition by enhancing the deposition rate.

Both morphology and microstructure independently play a major role in determining the mechanical, electrical, thermal and magnetic properties of a material[151, 152]. For example, roughness on the interconnect can severely affect their reliability and yield[153]. Similarly, grain size and texture of Cu films can influence the electromigration resistance of interconnects[154]. Despite the significance, the problem of what determines the microstructure and surface morphology of electrodeposited Cu films remains largely unsolved. Few questions like why certain features appear during growth and dominate the topography or why certain grains have faster growth rates than others remain less explored. The key to solving such challenges lies in data linking the final microstructure to the surface structure at intermediate stages of growth since bulk and surface structures are interdependent. It is impossible to try to account for one without

considering the other.

In our study, AFM was used to image the surface of an electrodeposited Cu film on a microelectrode. The film is FIB milled to be able to extract microstructural information using EBSD. A template matching algorithm is developed to compare AFM and EBSD to try and match the crystallographic orientation to the surface features. The orientation of grains at the edge of the microelectrode and the centre is compared and the change in the texture orientation is discussed. The TBs at the edges and centre of the microelectrode are studied using the 'Mtex' Matlab toolbox[155].

6.1   Effect of chloride

The dual damascene process is used to fabricate interconnects by plating metals into trenches and vias. A successful plating involves complete filling of the vias and trenches without any voids or seam[156]. To produce void-free interconnects, chloride is combined with organic compounds like polyethylene glycol(PEG) or polypropylene glycol(PPG) as a suppressor and bis(sodiumsulfopropyl) disulfide(SPS) as an accelerator is used in the superconformal filling mechanism[20].

Anion adsorption on the metal substrate surface depends on the strength of the solvation. Weakly solvated anions like SO_4^-, Cl^-, Br^- and I^- lose their solvation sheaths and can form a chemical bond with the surface of the metal electrode. This is referred to as specific adsorption. With high surface coverage of the adsorbed species, they can form closely packed adlayers on the surface of the electrode. The adlayer formed on the surface can affect Faradaic reactions, influencing the electrochemical processes. Certain anions on the surface can block reaction sites which can lead to a reduction in the reaction rate[157]. Morphological rearrangement can occur by the influence of adlayers on the surface step orientation due to complex formation in the presence of Cu[158]. Chloride is known to affect the deposition\dissolution of Cu.

The reduction reaction during the Cu electrodeposition process has two consecutive steps[159]:

$$Cu^{2+} + e^- \rightarrow Cu^+$$
$$Cu^+ + e^- \rightarrow Cu$$

(6.1)

94

The first step is the slowest hence the rate-determining step. Chloride in millimolar quantity in Cu electrodeposition forms $CuCl_{ads}$, an anion-bridged active surface complex[160, 161, 162]. In the presence of $CuCl_{ads}$ the deposition proceeds by:

$$Cu^{2+} + Cl^-_{ads} + e^- \rightarrow CuCl_{ads}$$
$$CuCl_{ads} + e^- \rightarrow Cu + Cl^-$$

(6.2)
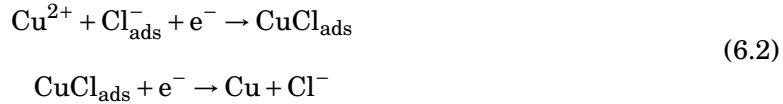
The mechanism in equation 6.1 and the chloride-mediated mechanism in equation 6.2 can occur simultaneously, increasing the overall deposition rate[161]. Chloride has a catalytic effect on the deposition of Cu. Formation of solid CuCl is possible during Cu deposition in the presence of chloride. From many studies, it can be concluded that solid CuCl precipitate formation during Cu deposition happens when the chloride concentration was very high (>1mM)[161, 163, 159]. A concentration of 0.25mM was used in our study. Because of the small quantity of chloride in our solution, it is highly unlikely that solid CuCl was deposited during the experiment.

6.2 Preparation of Cu film for EBSD

The polycrystalline Cu film was deposited from an electrolyte solution of 0.01M $CuSO_4$+0.1M H_2SO_4 + 0.25mM KCl. The film was deposited on an Au square microelectrode of dimension 50x50 μm fabricated using maskless lithography. An electrode potential of -250mV was applied and the deposition was for 10 minutes. Figure 6.1 shows the CV performed on the square microelectrode. From the CV, the potential chosen for electrodeposition is under mixed kinetic diffusion control. As part of the initial study on the influence of potential on film growth, a starting point of -250mV was chosen. A Cu strip served as both a reference and counter electrode.

The thickness of the film was measured to be $\approx$1.2μm by the AFM. The entire surface of the microelectrode was scanned by sequential move by the AFM. Each move scans an area of 20x20 μm generating a high-resolution image of that particular area. The AFM can be made to move in a series of sequential micrometre steps automatically in the x and y directions, followed by a surface scan. This movement can be programmed on the NanoScope software, which drives the AFM controller. Using this mechanism, the entire sample can be imaged without a user having to manually control the system.

95
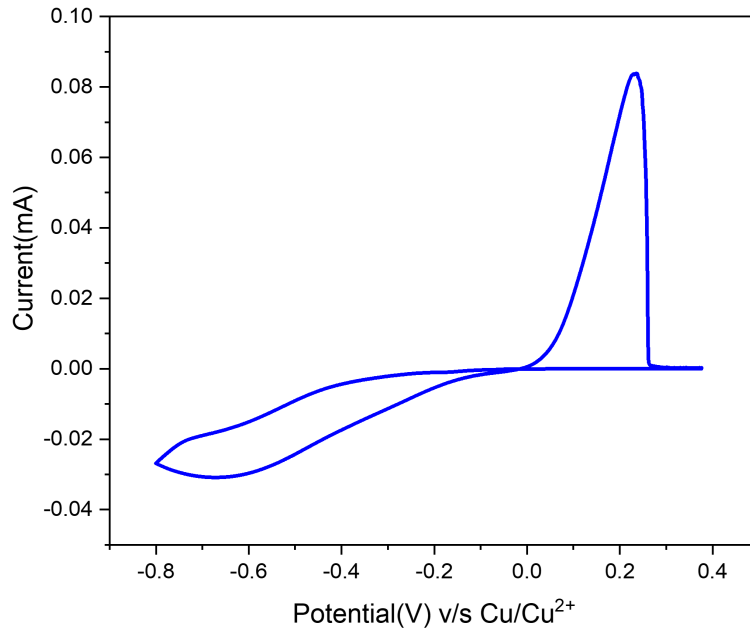
FIGURE 6.1. CV performed on a microelectrode measured at a scan rate of 20mV/s.

Before FIB milling, the photoresist was removed using resist stripper S1165. This process left a mesa of Cu. Then the mesa is FIB milled to a thickness of ≈ 0.45 μm in the in-plane direction with an ion beam current of 460pA. This leaves the top surface of the film milled and prepared for EBSD measurements. Similar to AFM imaging, the EBSD detector will move sequentially along the entire length of the sample generating diffraction patterns that can be used to interpret the crystallographic orientation of each grain. For a surface-sensitive technique like EBSD, having a uniform top layer of the specimen, devoid of contamination and oxidation, is crucial. A rough non-uniform sample surface can block the diffraction signals from the high tilt angle of the incident beam reaching the detector, thereby affecting the quality of EBSD patterns[164]. The sample, prepared on a microelectrode, has more Cu deposits towards the edge compared to its centre. To obtain a flat surface, the sample is FIB milled and prepared for EBSD measurement.

Figure 6.2 is the schematic illustration of the preparation of the Cu film for EBSD using FIB milling.

Figure 6.3 represents the SEM image of the same Cu film before and after FIB milling. In
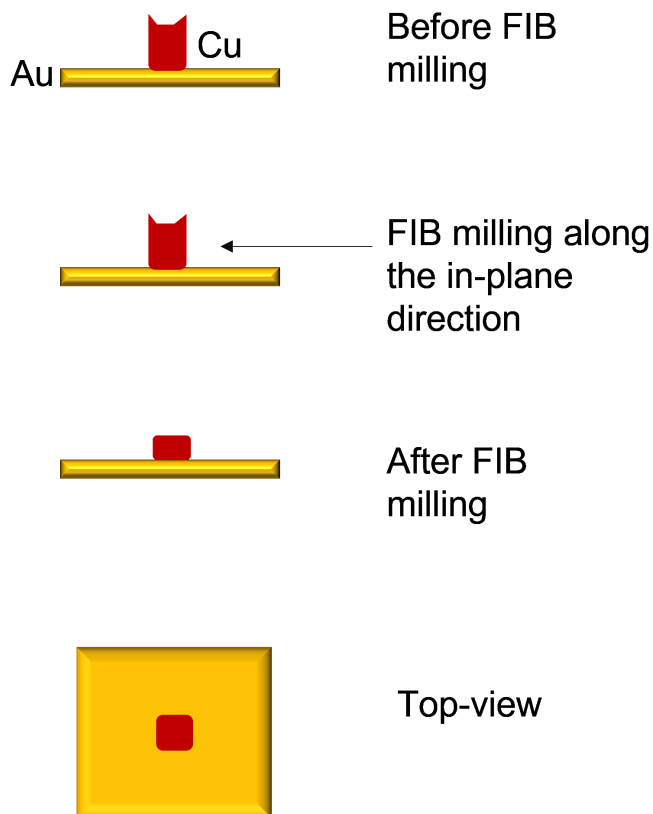
FIGURE 6.2. The schematic illustration of preparation steps of the Cu film for EBSD measurement. The mesa of Cu has a non-uniform thickness at the edges. The sample is FIB milled to produce a flat top surface for EBSD measurements.
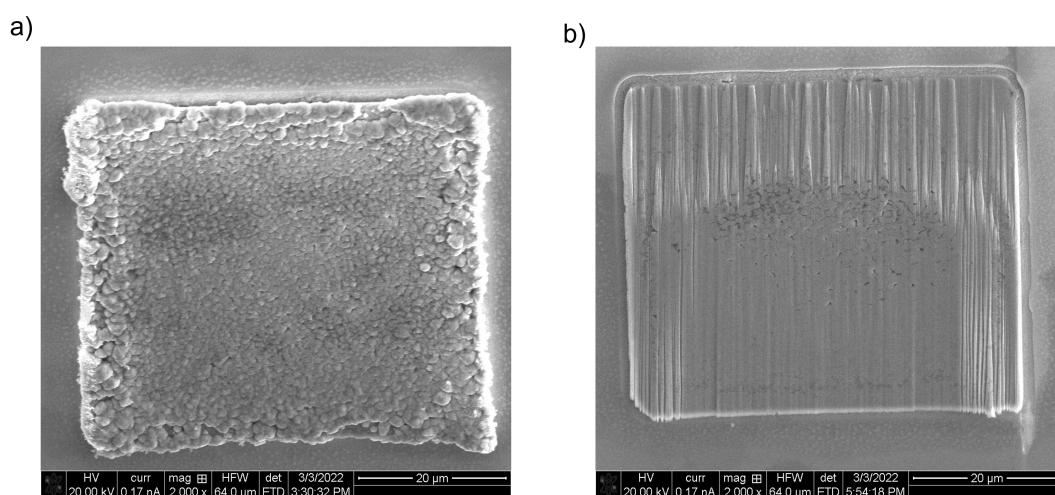
FIGURE 6.3. SEM image of the Cu microelectrode of dimension 50x50μm a) before FIB milling b) after FIB milling. The sample is FIB milled in an in-plane direction for EBSD measurement.
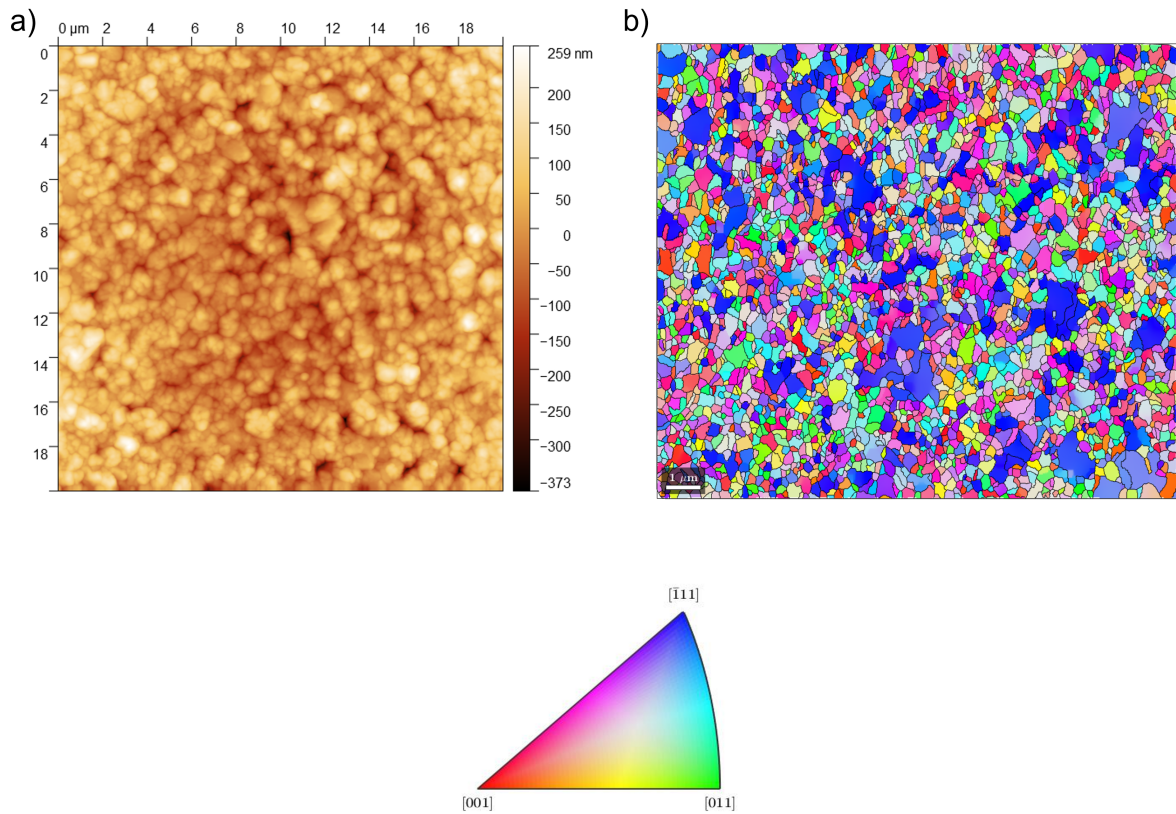
FIGURE 6.4. a) AFM image of a selected region in the microelectrode b) the corresponding EBSD image of crystallographic orientation of the grains of the same region. The IPF map helps to visualize the EBSD image given here.

figure 6.3b, the sample surface exhibits curtaining effects. Artefacts like curtaining can arise from differential sputtering rates due to the local change in surface morphology. It is undesirable and one of the ways to mitigate this problem is by using reduced ion beam current. Figure 6.4 is an example of an AFM image and its corresponding EBSD data. The figure includes the inverse pole figure or IPF map. The IPF map helps to visualize the material according to the colours assigned to the directions. It tells us which plane of the crystal lies parallel to the sample surface.

6.3 Template matching: Comparing surface morphology and crystallographic orientation

The microstructure and morphology of electrodeposited films are key to their performance. The bulk and surface topography are linked together, combining how one is related to the other can give us more insight into several phenomena affecting the final film structure. One way to combine surface and bulk information is by combining the data from the surface imaging technique, AFM with the EBSD data which is capable of delivering microstructural information for a polycrystalline film. Combining AFM and EBSD data will enable us to correlate the surface structure with the microstructure of the same area of the film. Microstructural information at the intermediate stage of the film is linked to the final surface morphology of the film and then we try to link which grain with a particular orientation represents a certain surface feature. This linking of microstructural and surface morphology can be done by scanning the entire surface of the electrodeposited Cu film generating images, then trying to map the same area to the EBSD image which holds the crystallographic orientation data of the same region. The AFM and EBSD generate images and we can try to match the same region in the AFM image to the EBSD or vice versa by a template-matching algorithm.

The advantage of using a template matching algorithm arises when the deposition is carried out on a microelectrode, and its surface is imaged in real-time by the HS-AFM during the film growth. Instead of physically marking the sample, the HS-AFM can capture a sequence of AFM images at regular intervals during the deposition process, providing continuous monitoring of the microelectrode surface throughout growth. Once the deposition is complete, the electrodeposited film can be FIB-milled to different depths. EBSD will then identify the grain orientation at each level exposed by the FIB, creating depth-dependent microstructural information.
From the EBSD data, using the template matching algorithm, we can assign a crystallographic orientation to each part of the HS-AFM images, thereby revealing direct correlations between certain surface features and microstructure. This approach allows for non-destructive and high-resolution investigation of the microstructure during the deposition process.

In the template matching technique, any region of the image can be chosen as a template.

a)

b)
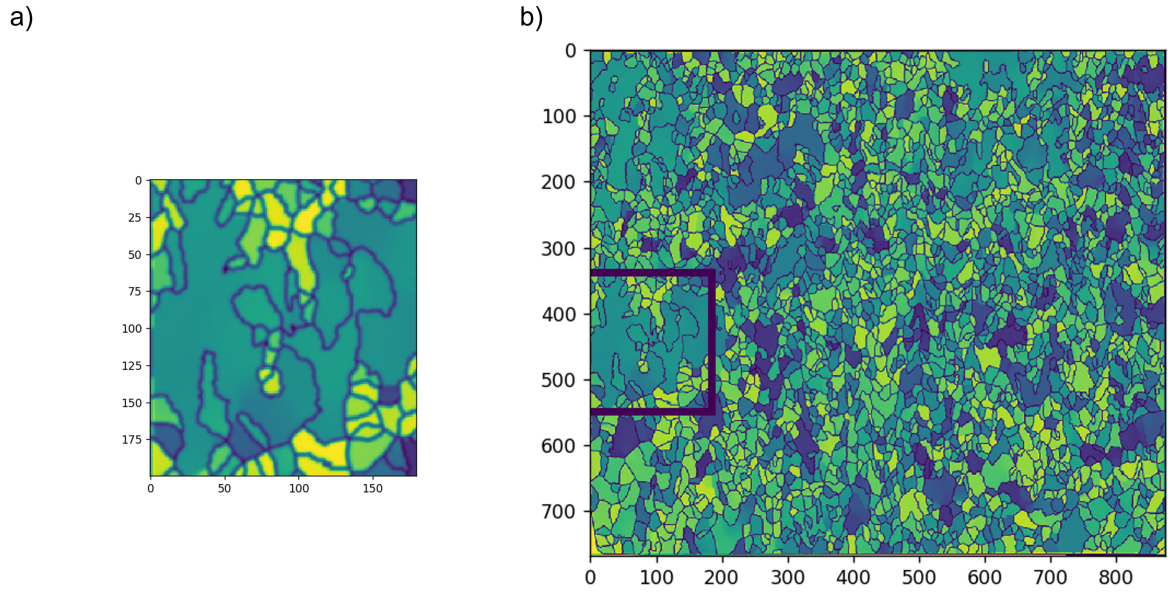
FIGURE 6.5. a) The template chosen to be matched with the EBSD image b) EBSD image after
template matching. The rectangular box represents the area identified as the best match for
the chosen template. The EBSD image is converted to greyscale to eliminate complexities while
computing.

Then the image is rotated at different angles θ. After finding the best angle, the best correlation

coefficient is returned by the algorithm. The rotated image is then changed in magnification to

perform further template matching.

The Pearson correlation coefficient measures the linear correlation between two different sets

of data. For random variables (X, Y), the coefficient ρ is given by:

$$\rho_{X,Y} = \frac{\text{cov}(X,Y)}{\sigma_X \sigma_Y} \tag{6.3}$$

where cov is the covariance. Covariance is the expected value(mean) of the product of their

deviation from their mean values. Covariance determines to what extent two random variables

vary together. Any change in one variable will change the other. For random variables (X, Y)

covariance is given by:

$$\text{cov}(X,Y) = \text{E}[(X - \text{E}[X])(Y - \text{E}[Y])] \tag{6.4}$$

here $E[X]$ and $E[Y]$ represents the mean value of X and Y respectively. σ_X and σ_Y in the
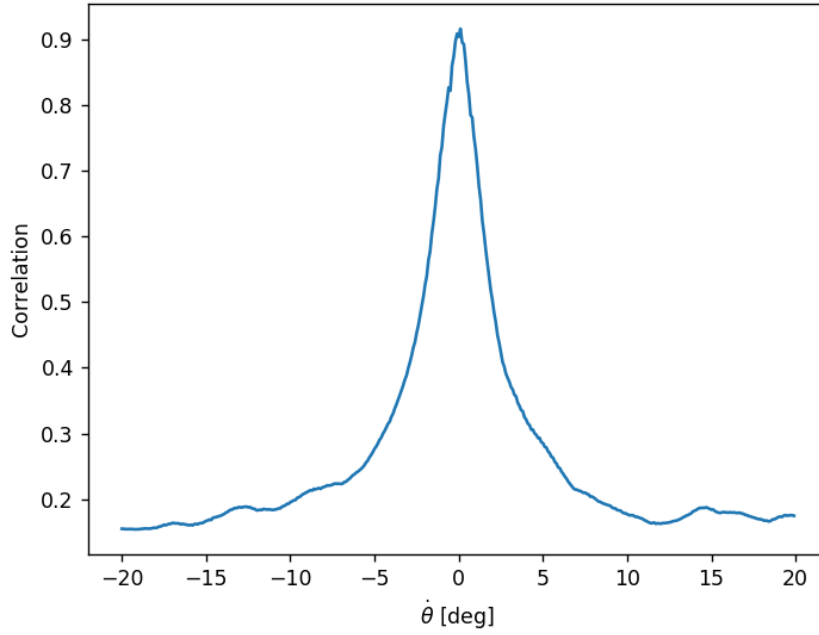
FIGURE 6.6. Correlation v/s rotation angle θ.

a)
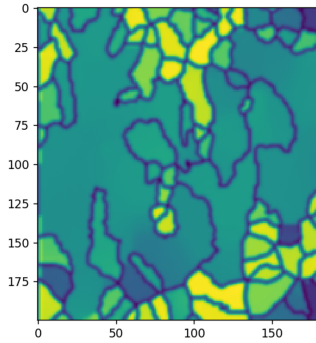
b)
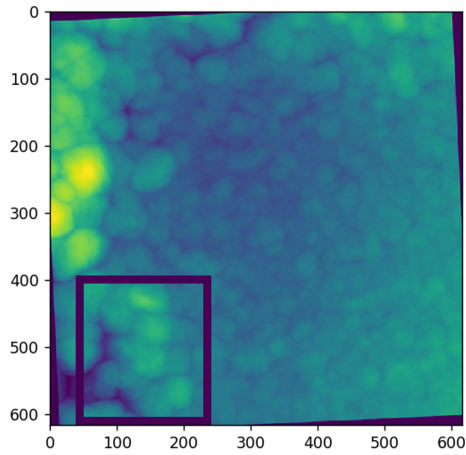
FIGURE 6.7. a) Chosen template from an EBSD image b) the region identified by the algorithm in the AFM image marked inside the box.

equation 6.3 are the standard deviations of X and Y respectively.

A correlation value of '1' means X and Y are fully correlated. Figure 6.5 represents an

a)   b)
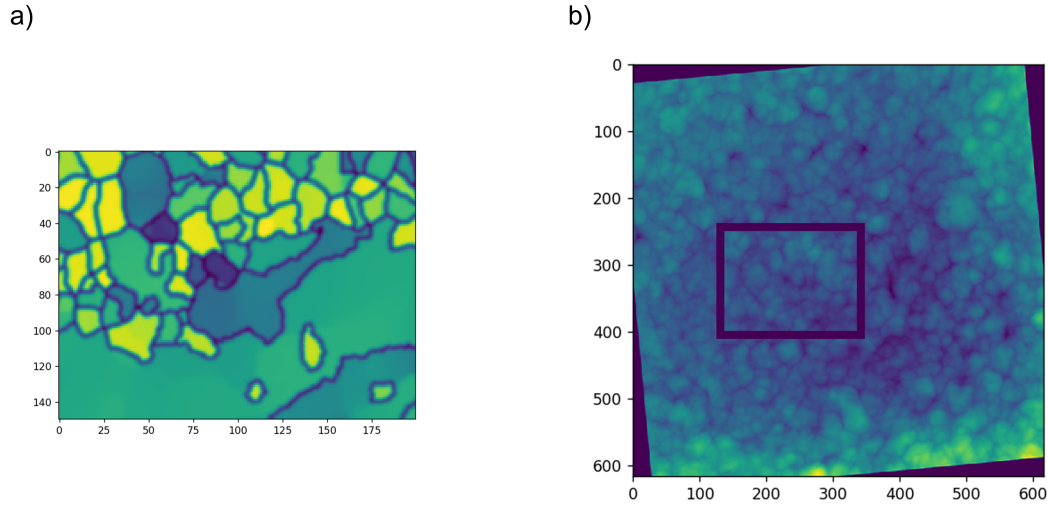
FIGURE 6.8. Example of template matching a) Chosen template from an EBSD image b) the region identified by the algorithm in the AFM image marked inside the box.

example of template matching. Here the template is a particular region of the EBSD image. Then the template is matched to the same EBSD image shown in figure 6.5b. A box is drawn around the region in the image where the algorithm was able to match the template.

Figure 6.6 shows the correlation value v/s the rotated angle θ of the image in figure 6.5. As we can see from the figure 6.6, it is evident that the algorithm was able to match the template to the image. From figure 6.6 it is evident that the correlation is almost '1' indicating that the template and the region matched are fully correlated.

The same procedure as described above is repeated. Now the template is taken from the EBSD image and is attempted to match with the AFM image. Here, the AFM image is the one that undergoes changes in rotation and magnification. Figure 6.7 is an example of template matching. A region of interest from the EBSD image is chosen for the template and this template is matched to the same area in the AFM image. Figure 6.8 is also another example.

From Figure 6.9a and b, it can be noted that the correlation value is not close to '1' but much less. This indicates the algorithm fails to match the EBSD template to the exact region of the AFM image.

While performing FIB milling on the sample, the thickness of the mesa of Cu was milled down

a)

b)
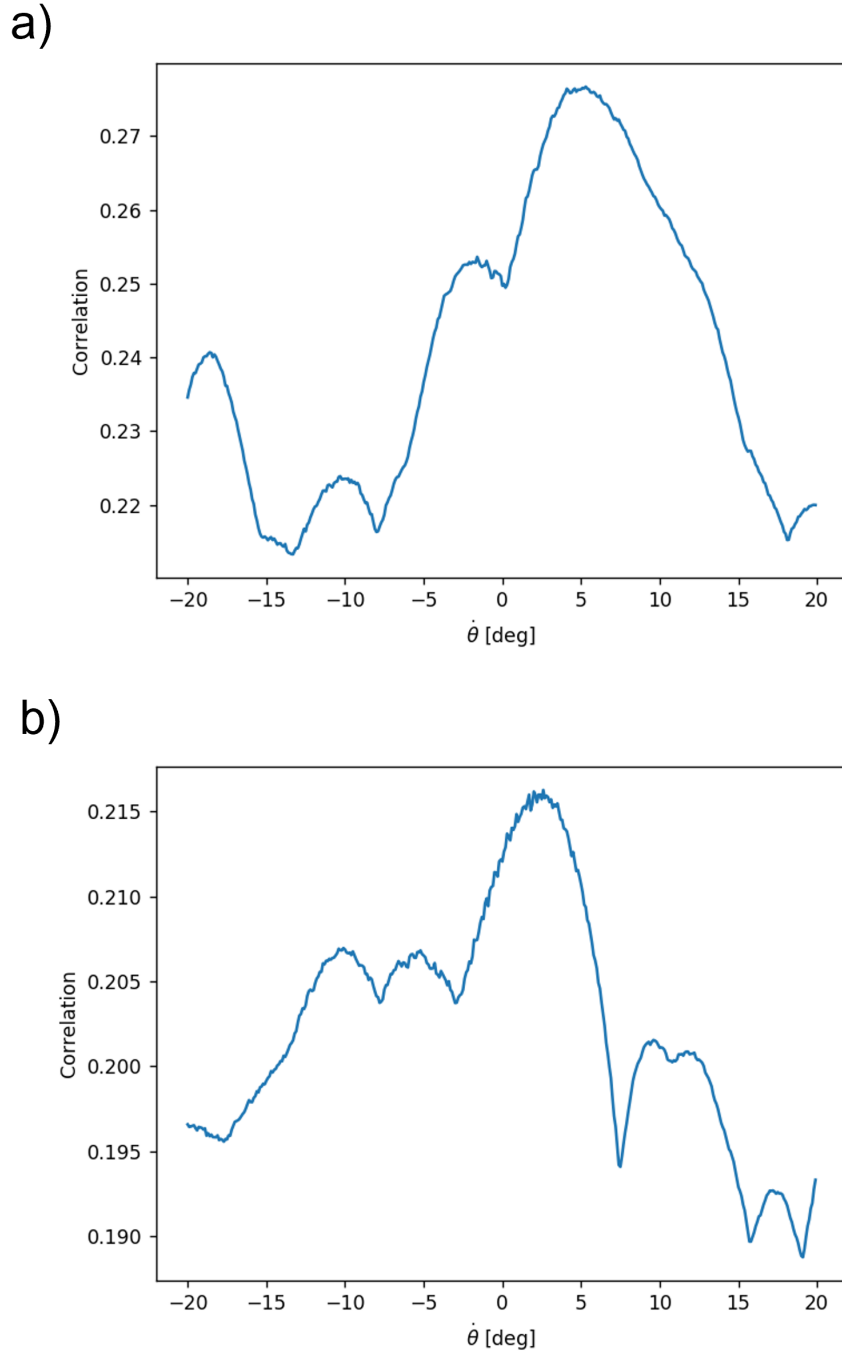
FIGURE 6.9. a) Correlation v/s the rotation angle θ plots of figure 6.7 b) figure 6.8.

to half of its thickness. Then EBSD was performed on the Cu sample with half of its thickness reduced. In the case of AFM, the top surface of the Cu film was scanned before preparing the sample for FIB milling. Comparing the microstructure at half thickness to the top morphology

gives a poor match. The region or grains around the middle of the thickness of the Cu film might not represent the topography, Grains could be smaller or larger or might stop growing by the time the film reaches its full thickness. This means that the microstructure is changing with thickness: the film is not purely columnar. In order to obtain fully correlated template matching, the FIB milling must be performed closer to the top surface removing only a few 'nm' in thickness. Then the FIB milled surface will represent the top surface prior to FIB milling and a successful template matching with the AFM images is likely to be possible.

The FIB milling on the square microelectrode removed excess thickness from the copper film, which likely resulted in the failure of the template matching of AFM images to the EBSD images. The in-plane milling was performed on the sample for the first time. Considering the time scale to prepare the sample and redo the FIB milling, reattempting the experiment was limited due to time constraints for the completion of this work. In future studies, careful measures need to be taken to ensure that the sample is milled to the desired thickness.

6.4 Crystallographic orientation of grains at the centre and edge of the microelectrode

The electrodeposition of the Cu film was carried out on a microelectrode of diameter 50μm. Looking at the AFM image of the entire microelectrode after deposition, it can be observed that there is a significant height difference between the deposit at the centre of the microelectrode compared to the edges. Figure 6.10 shows the AFM image of the microelectrode and its 3D view. It is clear from figure 6.10b that the edges are much taller than the centre, indicating a faster growth at the edges.

Macroelectrodes or planar electrodes are characterized by their large size, ranging from millimetres to centimetres. The diffusion layer at a planar electrode is flat due to its size, and the diffusion towards these electrodes is considered 'linear,' as illustrated in figure 6.11a. On the other hand, in the case of a microelectrode, due to its specific geometry, the diffusion layer exhibits curvature, and the diffusion has a radial component. The diffusion has a radial component towards the edges[84]. This enhanced diffusion, known as the 'edge effect,' causes a faster growth

FIGURE 6.10. a) AFM image of the Cu film deposited on the microelectrode b) 3D-view of the Cu film deposited on the microelectrode. The thickness of the film is higher at the edges.

rate at the edges. Figure 6.11b shows the diffusion flux towards a UME, which has a curved shape and is not always perpendicular to the UME surface.

The crystallographic orientation at the centre and the edge of the microelectrode are compared to the EBSD data of these regions. Figure 6.12 shows the inverse pole figure of the selected regions from the centre and the edges of the microelectrode. Inverse pole figures are the 2D representation of orientations[155]. The orientations are plotted with crystal directions as the axes. z is the sample normal. Figure 6.12a represents selected regions from the centre. It can
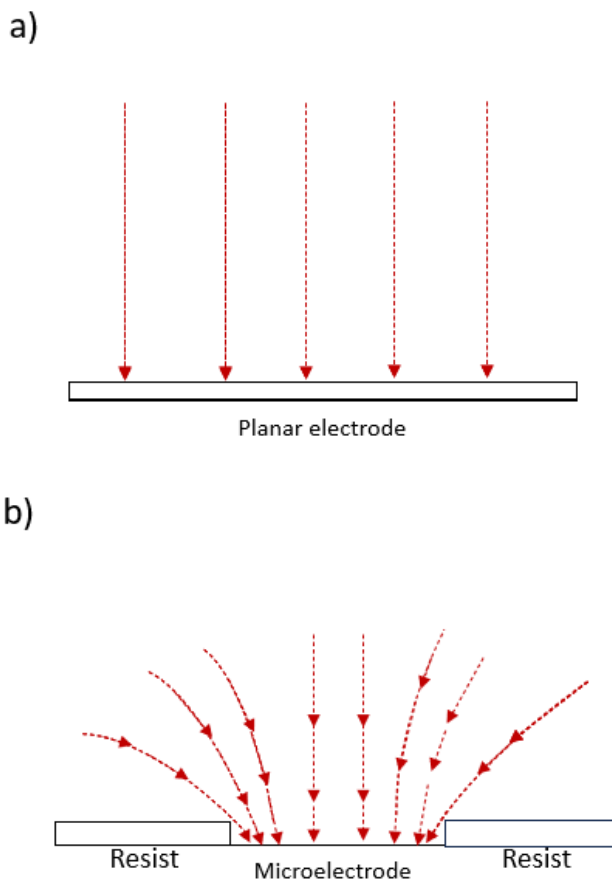
FIGURE 6.11. a) The movement of ion flux towards a planar electrode b) the movement of ion flux towards the centre and the edges of the square microelectrode. The current is greater towards the edges than the centre.

be seen that the grains in this region prefer <111> out-of-plane direction or have strong (111) orientation. Figure 6.12b represents selected regions from the edge of the microelectrode. It shows a strong (111), (110) texture along with a weak (100) texture. A change of texture from (111) to (110) and (100) is observed.

Chan et.al claims that (111) or (110) orientation can be controlled by varying the concentration of chloride in the electrolyte[165]. They observed a change from random texture to increased (110) texture for DC electrodeposited films as the chloride concentration changed from chloride-free to a controlled amount of chloride. They found that the film starts to develop a strong (110) texture as the chloride concentration increases with increasing film thickness. According to their studies, with increasing thickness, increasing strain energy develops and (110) planes are favoured as
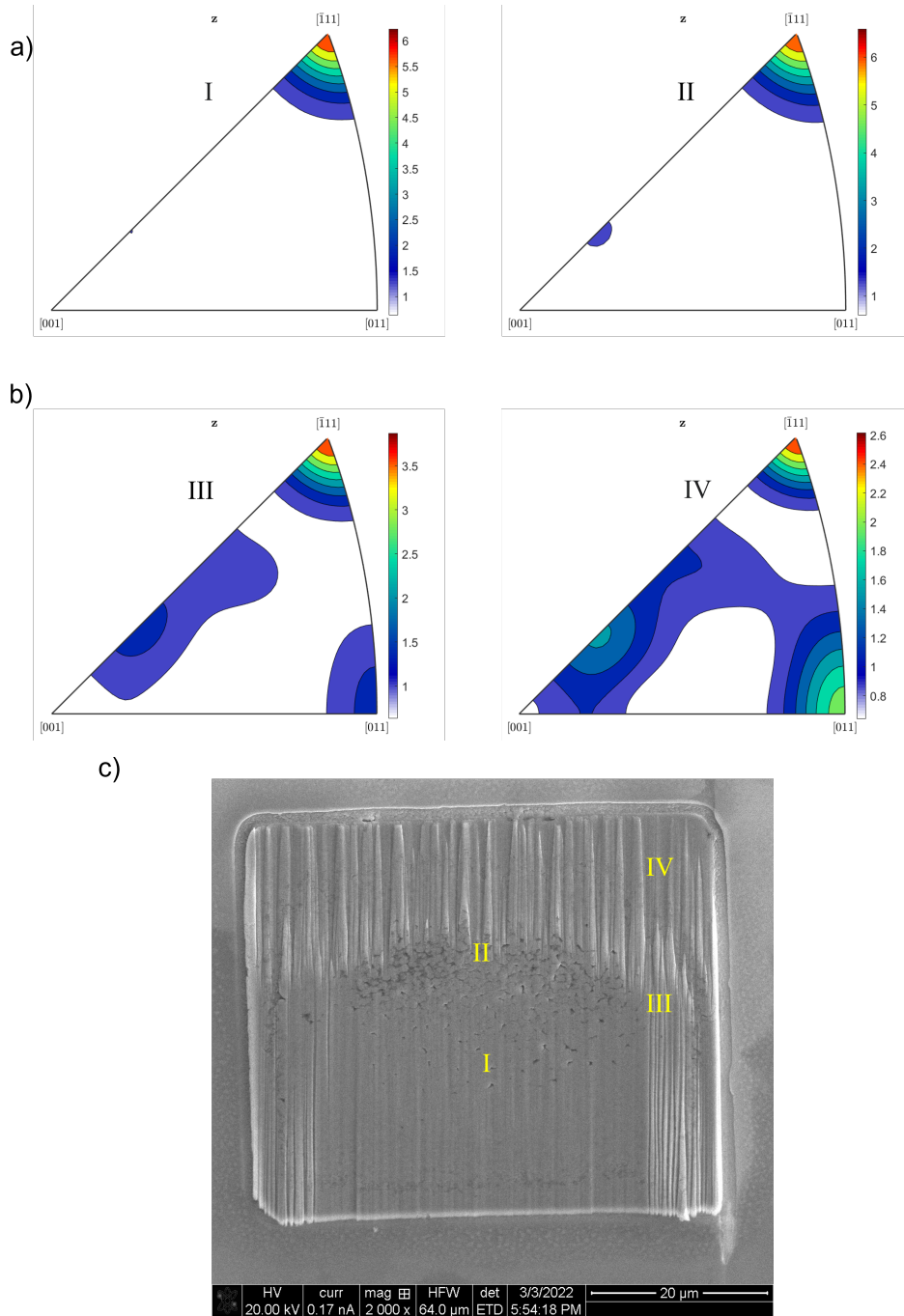
FIGURE 6.12. Inverse pole figure of selected regions of the microelectrode a) the centre and b) the edges c) SEM image of the microelectrode with regions marked representing maps in 6.12a and b.

they have a greater ability to accommodate the strains compared to the (111) planes.

Kremmer et.al observed a variation in the texture of the electrodeposited Cu films when the applied potential is varied[138]. The potentials were classified into three regions. Region one is

charge-controlled (lower overpotential), region two is diffusion-controlled (high overpotential) and third is the region where the electrodeposition is accompanied by hydrogen evolution. The preferred orientation transformed from {111} in region one to {110} in the second region to {100} in region three, so the applied potential is influencing the crystallographic texture of their films.

In our studies, both the concentrations of chloride and the electrode potential remain the same. The variable here is the thickness of the Cu deposit as the film grows at different rates at the centre and the edge. From XRD measurements Vasiljevic et. al. observed a transition of {111} texture to {220} as the thickness of the Cu film grown in the presence of chloride increased[162]. They claim that this could be the result of repeated twinning.

In this study, it is observed from figure 6.12 that a change in texture is evident when we compare the centre and the edges of the microelectrode. From figure 6.10, it is clear that the thickness around the edge is significantly higher than the central region of the square microelectrode. The textural changes could be due to the mechanism of repeated twinning. Twinning is mostly seen in grains that have a preferred orientation that drives the growth direction not perpendicular to the surface of the film. Later changes to preferred orientation via twinning[166].

According to the studies conducted on Ag by Pangarov and Velinov, twinning is a secondary process that occurs later during the growth process. The repeated twinned structure encountered in their studies has a five-fold symmetry[106]. The twinning of this crystal is characterized by a wedge-like 'seam' and has (110) planes parallel to the substrate. The 'seam' is a region of great activity due to the presence of defects like dislocations. This could explain why the texture changes to (110) from (111). The growth sites encourage adatom incorporation to these imperfections present on the five-fold twin structures promoting the growth of (110) textured crystals. It is interesting to see that the texture of the grains at the edge and centre is different even when the Cu film is milled to half of its thickness. Even in the intermediate stages of the thickness, the textural difference is present. This is not enough to conclude that the texture of the film depends only on the thickness. The mass transport towards the edge of the microelectrode was also altered due to the geometry of the microelectrode as shown in figure 6.11.

 The twinning nature of the crystals in the edge and the centre of the microelectrode is evaluated
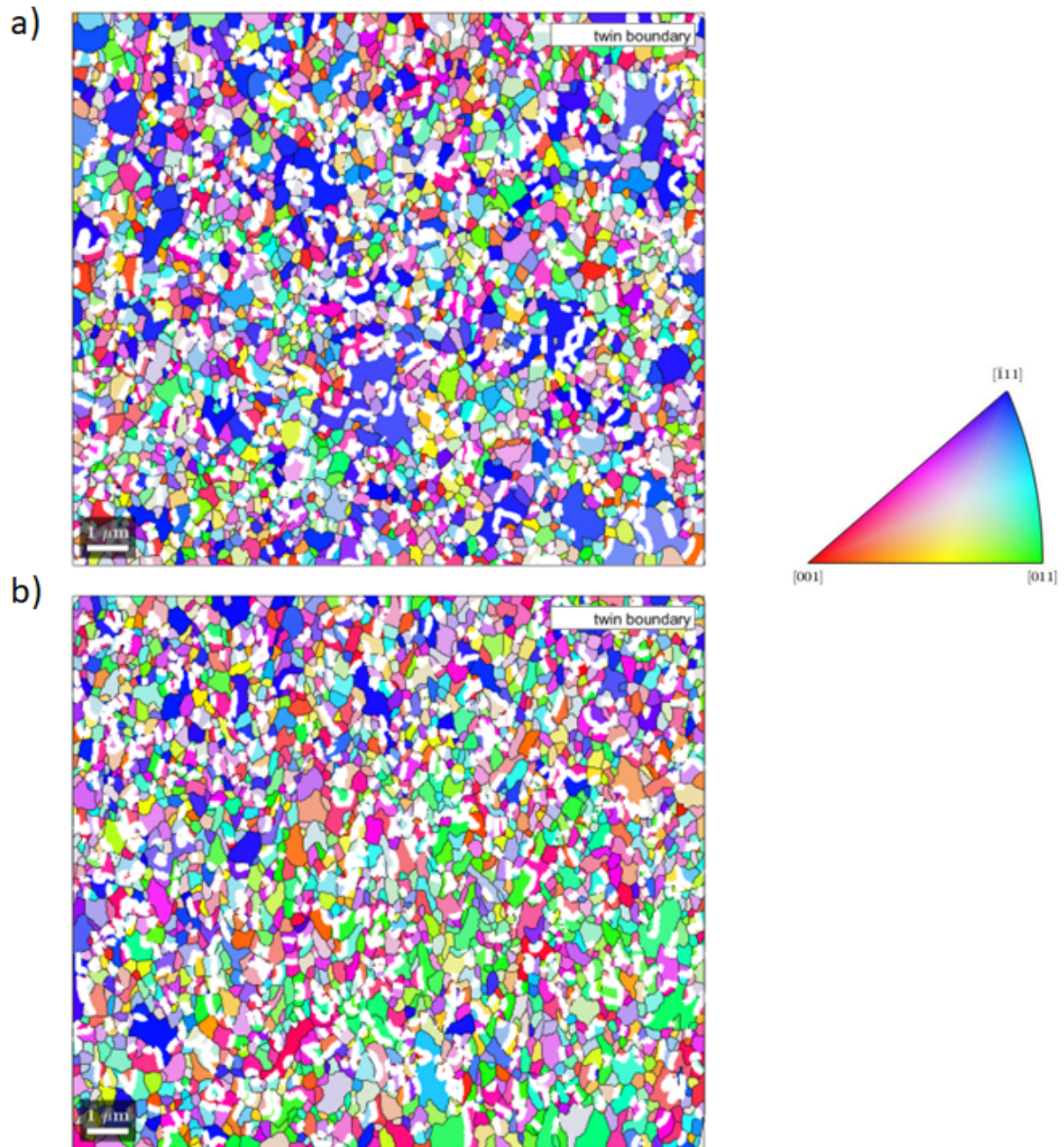
FIGURE 6.13. Twin boundary analysis on the microelectrode a) centre b) edge. The twin boundaries are marked in white lines.

from EBSD data. The same regions used in figure 6.12 are chosen to determine the twinning present in the crystal. Figure 6.13 shows the twin boundaries identified by 'Mtex'. Both regions exhibit twin boundaries rotated about the (111) plane, with an angle of rotation of 60°. No

conclusion can be drawn from the analysis of twin boundaries present at the edges and the centre. Growth twins are common in FCC crystals like Cu, Au and Ag[167]. According to Pangarov and Velinov, the twinning can take place in {111} plane which is observed from our studies[106].

6.5 Chapter discussion

Electrodeposited Cu film from chloride-controlled electrolyte was grown on lithographically patterned microelectrode of side $50\mu m$. The surface topography of the sample was imaged by the AFM. For microstructural information, the sample was FIB milled followed by EBSD measurements. The studies revealed:

1) The morphological features were attempted to be tied to the microstructural data using a template-matching algorithm. The surface topography was matched to the crystallographic orientation by matching a template of EBSD data to AFM and evaluating the correlation coefficient. This is observed in figures 6.7,6.8,6.9. In order to obtain maximum correlation the Cu film should only be milled by a few nanometers. This was not followed in our sample preparation which explains the lower correlation value.

2) The thickness of the Cu film varies across the microelectrode. The film is thicker towards the edges compared to the centre. The orientation of the film has slight variation when comparing the centre and the edge. While the centre has a dominant (111) texture, the edges exhibit a dominant (111) texture along with (110) and (100). The textural change in the film can be seen in figure 6.12 The textural changes could be due to the present five-fold symmetry twins. These structures possess growth sites which promote faster growth.

3) Twinning analysis was performed on the EBSD data from the centre and edges. Both areas contain twinning and twin rotated about (111) plane with an angle of 60°as shown in figure 6.13.

6.6 Chapter summary

The morphology and microstructure of an electrodeposited Cu film are studied using the AFM and EBSD techniques. The film was grown on a lithographically patterned microelectrode of dimension $50\mu m$. A template-matching algorithm was developed to match surface morphological

features to their crystallographic orientation. The FIB milled microelectrode was used to extract crystallographic orientation using the EBSD measurements. The orientation analysis on the centre and the edge region of the microelectrode revealed different textures. We suggest the mechanism of twinning as the cause of textural change. It could be due to the presence of the fivefold twins which holds imperfections and dislocations. Growth twins were present both in the centre and the edge region of the microelectrode with rotation about the (111) plane and with a rotation angle of 60°.

CONCLUSIONS AND FUTURE WORKS

Morphological and microstructural data for polycrystalline Cu films were successfully obtained using surface imaging and diffraction techniques. Electrodeposited Cu films were imaged using HS-AFM, AFM and SEM. Details about grain orientations and grain boundaries were extracted using FIB, XRD and EBSD.

In-situ HS-AFM which is capable of generating a high-resolution video of a surface while scanning was used to study the surface evolution of a Cu film in real time. The experiment was performed on a microelectrode, scanning the same area to observe the changes in the film surface as it grows. The study focused on understanding how a Cu film surface coarsens with thickness and what phenomena drive the surface to coarsen. The growth pattern observed on the surface includes accelerated local growth of certain grains compared to their neighbours. Grains at various locations in the film exhibited overgrowth, one grain growing over the other. A growth mechanism was proposed to explain how surface coarsening would take place. The growth mechanism involves accelerated growth of certain grains combined with overgrowth.

The AFM images contain local surface topographical information, i.e. the surface height. Quantitative analysis was performed on the images generated by the HS-AFM. Scaling analysis revealed anomalous scaling behaviour of the Cu film. Local slope analysis shows that the slope

increases with the increasing thickness of the film. Accelerated local growth could be due to the presence of certain microstructural features like half-crystal sites like a five-fold twin which promote faster growth. The microstructural information needs to be extracted using a diffraction technique like EBSD. This is attempted in chapter 6.

Tip-enhanced growth was observed during the HS-AFM measurement. A faster growth rate was observed where the tip was scanning. This tip-enhanced growth could be due to the disruption of an oxygen adlayer formed on top of the Cu film.

Pulsed electrodeposition was used to produce Cu films with hexagonal pyramid-like morphology. Previous work showed films with this characteristic morphology are highly 'twinned'. Twinned Cu films are very desired structures because of their superior mechanical and electrical properties. The effect of electrode potential on grain size revealed that the grain area increases with increasing overpotential. This was investigated by calculating grain area from the AFM images using the watershed segmentation algorithm. Detailed slope analysis for hexagonal features produced by pulsed electrodeposition at different overpotentials showed that hexagonal pyramids formed at -650mV have larger slopes compared to -612mV. This is the first quantitative AFM study of the morphology of these features, though they have been observed in previous work. Local slope analysis performed on complete AFM images of Cu films grown at different potentials showed a distinctive slope distribution for Cu films having hexagonal morphology. The cross-sectional FIB milling on the Cu film confirmed that it contained twins with horizontal lamellae. This indicates that the twins are growing perpendicular to the growth direction of the film. XRD measurement revealed (111) texture for the film. Two different mechanisms could cause the twinning and formation of hexagonal pyramids, stress relaxation during the 'OFF' period during pulsing or screw dislocation-driven growth model. We believe that screw dislocations are driving the growth of the hexagonal structures. For the observed 'flower-like' morphology, a newly emerging screw dislocation on an existing spiralling screw dislocation could result in forming a special structure.

It was difficult to reproduce certain results during pulsed deposition. This could be due to the relatively low concentration of Cu ions in the electrolyte. The overpotential applied in low concen-

tration electrolyte drives mass transport instead of electrodeposition, affecting the reproducibility.

For connecting the surface and the bulk of a film, the morphology and the microstructure need to be correlated. We performed the correlation by implementing a template-matching algorithm. This involves matching a template from an EBSD image to an AFM image. EBSD has the crystallographic orientation information and AFM has the surface topography. Even though the template matching algorithm worked, its ability to match the EBSD template to a region on the AFM image was limited. The issue mainly arose as the FIB milling performed on the mesa of Cu prepared from a microelectrode removed too great a thickness. It is very difficult to compare the top surface details to features in the intermediate thickness of the film if the grain cross-section changes.

The edge and the central regions of the microelectrode exhibited different crystallographic orientations. The orientation changed from (111) to (110) near the edges. Many studies argued that the concentration of chloride or potential can contribute to this. While these parameters remained the same for our experiment, the thickness was different near the edge. Edges of higher thickness could carry special five-fold twinning structures with an enhanced supply of growth sites for accommodating adatoms. Earlier studies on five-fold twins reveal 110 orientations. Stacking fault twins are observed on the edge and central region of the microelectrode. This is very common in FCC crystals.

For future work, the reproducibility of the pulsed electrodeposition needs to be improved. The same experiment as described in Chapter 5 should be repeated with a higher concentration of ionic species in the electrolyte solution (> 0.1M). Transmission Electron Microscopy(TEM) is a powerful tool to produce high-resolution images. FIB-TEM can be used for the preparation and imaging of the twinned Cu, to understand the origin of the hexagonal pyramids. TEM might be capable of imaging the origins of screw dislocations, and the spacing between any nanotwins. It is important to study the twin spacing as it is known to affect the mechanical properties of a material. It would be interesting to see if varying the electrode potential can vary the twin spacing.

Additives capable of attaching to defects like screw dislocation could give insight into whether the twins are generated by spiralling screw dislocations or not. These additives will block any growth sites preventing the unique screw dislocation growth process.

For calculating the slope of hexagonal features there is a need to identify which grains are hexagonal or not. This involves identifying a region of interest by eye. It would be faster and more efficient to train a machine learning algorithm to identify these features on the images. This requires a large number of data sets. Once the algorithm is developed, the process of identifying the features from the image becomes faster and easier.

In the case of the template matching algorithm, it would likely be successful if the sample is only lightly milled/polished so that the EBSD surface grains and the AFM grains look identical so that they can be mapped to each other. It would be interesting to look at a cross-sectional FIB image of the entire microelectrode to see how the grains look and how they structurally differ at the edges and the centre. This would also give us an idea of why the orientation change is happening in these regions.

The HS-AFM can be used to obtain high-resolution surface topography, while FIB milling can be used to section the resulting film to characterize the grain structure at different depths by EBSD. Thus combining HS-AFM and EBSD data will enable us to correlate surface structural evolution with the post-deposition microstructure of the same area of the film. The ideal sample must be prepared from a microelectrode. This could open key aspects of electrodeposition to quantitative studies, like determining the relationship between growth rate and crystallographic orientation and understanding preferential nucleation at surface defects.

Polycrystalline films experience stress from their early stages to later growth stages. It is important to study the structural changes related to changes in stress in a film. Stress can limit the adhesion of the thin film to the substrate or change its magnetic properties by magnetostriction. The films electrodeposited on the cantilever of the AFM generate stress causing it to bend and deflect the incident laser beam which is recorded by the position-sensitive detector. The change in in-situ stress during growth interruption and film growth can thus be studied using the AFM.

115

APPENDIX A

A.1 List of publications and presentations

Aswathi Koorikkat, Oliver Payton, Loren Picco, and Walther Schwarzacher. *Imaging the surface of a polycrystalline electrodeposited cu film in real time using in situ high-speed afm*. Journal of the Electrochemical Society, 167(16):162510, 2020.

Aswathi Koorikkat, Oliver Payton, Loren Picco, and Walther Schwarzacher. Oral presentation. *Investigating the surface and microstructure of electrodeposited Cu films*. Great Western Electrochemistry Meeting, University of Bath, 2022, UK.

Aswathi Koorikkat, Oliver Payton, Loren Picco, and Walther Schwarzacher. Poster presentation (virtual poster). *Investigating the surface of a polycrystalline electrodeposited Cu film using In situ High-Speed AFM*. Interdisciplinary Surface Science Conference (ISSC-23) 2021, UK

Aswathi Koorikkat and Walther Schwarzacher. Poster presentation. *Connecting morphology and microstructure: the physics of polycrystalline electrodeposited films*. Great Western Electrochemistry Meeting University of Bath, 2019, UK.

[1] Panos C Andricacos. Copper on-chip interconnections: A breakthrough in electrodeposition to make better chips. *The Electrochemical Society Interface*, 8(1):32, 1999.

[2] Thomas P Moffat, Daniel Wheeler, Monica D Edelstein, and Daniel Josell. Superconformal film growth: Mechanism and quantification. *IBM Journal of Research and Development*, 49(1):19–36, 2005.

[3] SM Sze. Devices,". *Semiconductor Physics and technology*, 1985.

[4] Simon Min Sze et al. *Semiconductor sensors*. John Wiley & Sons, 1994.

[5] ME Cowher and TO Sedgwick. Chemical vapor deposited polycrystalline silicon. *Journal of the Electrochemical Society*, 119(11):1565, 1972.

[6] Myungchan Kang and Andrew A Gewirth. Influence of additives on copper electrodeposition on physical vapor deposited (pvd) copper substrates. *Journal of the Electrochemical Society*, 150(6):C426, 2003.

[7] J Musil and J Vlček. Magnetron sputtering of films with controlled texture and grain size. *Materials chemistry and physics*, 54(1-3):116–122, 1998.

[8] Tuomo Suntola. Atomic layer epitaxy. *Materials Science Reports*, 4(5):261–312, 1989.

[9] FY Yang, Kai Liu, Kimin Hong, DH Reich, PC Searson, and CL Chien. Large magnetoresistance of electrodeposited single-crystal bismuth thin films. *Science*, 284(5418):1335–1337, 1999.

[10] V Dhanasekaran, T Mahalingam, R Chandramohan, Jin-Koo Rhee, and JP Chu. Electrochemical deposition and characterization of cupric oxide thin films. *Thin Solid Films*, 520(21):6608–6613, 2012.

[11] Thou-Jen Whang, Mu-Tao Hsieh, and Ya-Chun Kao. Studies of single-step electrodeposition of cuinse2 thin films with sodium citrate as a complexing agent. *Applied Surface Science*, 257(5):1457–1462, 2010.

[12] Darko Grujicic and Batric Pesic. Electrodeposition of copper: the nucleation mechanisms. *Electrochimica acta*, 47(18):2901–2912, 2002.

[13] H Natter and R Hempelmann. Nanocrystalline copper by pulsed electrodeposition: the effects of organic additives, bath temperature, and ph. *The Journal of Physical Chemistry*, 100(50):19525–19532, 1996.

[14] Matthew J Siegfried and Kyoung-Shin Choi. Elucidating the effect of additives on the growth and stability of cu2o surfaces via shape transformation of pre-grown crystals. *Journal of the American Chemical Society*, 128(32):10356–10357, 2006.

[15] K Attenborough, R Hart, Steve J Lane, M Alper, and W Schwarzacher. Magnetoresistance in electrodeposited ni-fe-cu/cu multilayers. *Journal of magnetism and magnetic materials*, 148(1-2):335–336, 1995.

[16] Uwe Erb, Karl T Aust, and Gino Palumbo. Electrodeposited nanocrystalline metals, alloys, and composites. In *Nanostructured materials*, pages 235–292. Elsevier, 2007.

[17] R Akolkar. Current status and advances in damascene electrodeposition. 2018.

[18] Copper Interconnects. The evolution of microprocessors, 2012.

[19] Karl Doblhofer, Sabine Wasle, David M Soares, Konrad G Weil, and Gerhard Ertl. An eqcm study of the electrochemical copper (ii)/copper (i)/copper system in the presence of peg and chloride ions. *Journal of the Electrochemical Society*, 150(10):C657, 2003.

[20] Phillipe M Vereecken, Robert A Binstead, Hariklia Deligianni, and Panayotis C Andricacos. The chemistry of additives in damascene copper plating. *IBM Journal of Research and Development*, 49(1):3–18, 2005.

[21] Ying Jin, Yanfei Sui, Lei Wen, Fangmiao Ye, Ming Sun, and Qingmei Wang. Competitive adsorption of peg and sps on copper surface in acidic electrolyte containing cl-. *Journal of The Electrochemical Society*, 160(1):D20, 2012.

[22] TP Moffat, D Wheeler, WH Huber, and D Josell. Superconformal electrodeposition of copper. *Electrochemical and Solid-State Letters*, 4(4):C26, 2001.

[23] Ya-Bing Li, Wei Wang, and Yong-Lei Li. Adsorption behavior and related mechanism of janus green b during copper via-filling process. *Journal of The Electrochemical Society*, 156(4):D119, 2009.

[24] Shelly Miyasato. Tech brief: Elements of electroplating, 2018.

[25] Qi Xie, Xin-Ping Qu, Jing-Jing Tan, Yu-Long Jiang, Mi Zhou, Tao Chen, and Guo-Ping Ru. Superior thermal stability of ta/tan bi-layer structure for copper metallization. *Applied Surface Science*, 253(3):1666–1672, 2006.

[26] RK Singh Raman, P Chakraborty Banerjee, Derrek E Lobo, Hemtej Gullapalli, Madusha Sumandasa, Ashwin Kumar, Lokesh Choudhary, Rachel Tkacz, Pulickel M Ajayan, and Mainak Majumder. Protecting copper from electrochemical degradation by graphene coating. *Carbon*, 50(11):4040–4045, 2012.

[27] Jing Zhang, Yingchao Yang, and Jun Lou. Investigation of hexagonal boron nitride as an atomically thin corrosion passivation coating in aqueous solution. *Nanotechnology*, 27(36):364004, 2016.

[28] Mordechay Schlesinger and Milan Paunovic. *Modern electroplating*. John Wiley & Sons, 2011.

[29] Hanna Bishara, Subin Lee, Tobias Brink, Matteo Ghidelli, and Gerhard Dehm. Understanding grain boundary electrical resistivity in cu: the effect of boundary structure. *ACS nano*, 15(10):16607–16615, 2021.

[30] CL Briant and SK Banerji. Intergranularfailure in steel: the role of grain-boundary composition. *International metals reviews*, 23(1):164–199, 1978.

[31] JW Gibbs. Collected works, 1, footnote on p. 325, 1878.

[32] Melvin Avrami. Granulation, phase change, and microstructure kinetics of phase change. iii. *The Journal of chemical physics*, 9(2):177–184, 1941.

[33] IN Stranski and L v Krastanow. Sitzungsber. akad. wiss. wien, math. *Naturwiss. Kl., Abt. B*, 2(146):797, 1938.

[34] F. C. Frank and J. H. van der Merwe. One-dimensional dislocations. iii. influence of the second harmonic term in the potential representation, on the properties of the model. *Proceedings of the Royal Society of London. Series A, Mathematical and Physical Sciences*, 200(1060):125–134, 1949.

[35] M Volmer. eber die molekulabscheidung an kristallen und die bravaissehe hegel. *Physik. Z*, 22:646, 1921.

[36] Martin Volmer and A Weber. Keimbildung in übersättigten gebilden. *Zeitschrift für physikalische Chemie*, 119(1):277–301, 1926.

[37] Tibor Erdey-Grúz and Max Volmer. Zur frage der elektrolytischen metallüberspannung. *Zeitschrift für Physikalische Chemie*, 157(1):165–181, 1931.

[38] Tibor Erdey-Grúz and Max Volmer. Zur theorie der wasserstoff überspannun. *Zeitschrift für physikalische Chemie*, 150(1):203–213, 1930.

[39] E Budevski, G Staikov, and WJ Lorenz. Electrocrystallization: Nucleation and growth phenomena. *Electrochimica Acta*, 45(15-16):2559–2574, 2000.

[40] John O'M Bockris, Brian E Conway, and Ralph E White. *Modern Aspects of Electrochemistry: Volume 24*, volume 24. Springer Science & Business Media, 2012.

[41] N Pangarov. Jo'm. bockris, ga razumney, fundamental aspects of electrocrystallization, 1968.

[42] JW Diggle, AR Despic, and JO'M Bockris. The mechanism of the dendritic electrocrystallization of zinc. *Journal of The Electrochemical Society*, 116(11):1503, 1969.

[43] Henrik L Andersen, Benjamin A Frandsen, Haraldur P Gunnlaugsson, Mads RV Jørgensen, Simon JL Billinge, KM Jensen, and Mogens Christensen. Local and long-range atomic/magnetic structure of non-stoichiometric spinel iron oxide nanocrystallites. *IUCrJ*, 8(1):33–45, 2021.

[44] A Van der Drift. Evolutionary selection, a principle governing growth orientation in vapour-deposited layers. *Philips Res. Rep*, 22(3):267, 1967.

[45] Jiajun Chen, Enbo Zhu, Juan Liu, Shuai Zhang, Zhaoyang Lin, Xiangfeng Duan, Hendrik Heinz, Yu Huang, and James J De Yoreo. Building two-dimensional materials one row at a time: Avoiding the nucleation barrier. *Science*, 362(6419):1135–1139, 2018.

[46] Benoit Cormary, Tao Li, Nikos Liakakos, Laurent Peres, Pier-Francesco Fazzini, Thomas Blon, Marc Respaud, A Jeremy Kropf, Bruno Chaudret, Jeffrey T Miller, et al. Concerted growth and ordering of cobalt nanorod arrays as revealed by tandem in situ saxs-xas studies. *Journal of the American Chemical Society*, 138(27):8422–8431, 2016.

[47] Abhinav Bhandari, Sean J Hearne, Brian W Sheldon, and Sumit K Soni. Microstructural origins of saccharin-induced stress reduction in electrodeposited ni. *Journal of the Electrochemical Society*, 156(8):D279, 2009.

[48] Carl V Thompson. Structure evolution during processing of polycrystalline films. *Annual Review of Materials Research*, 30:159, 2000.

[49] Allen J Bard, Larry R Faulkner, and Henry S White. *Electrochemical methods: fundamentals and applications*. John Wiley & Sons, 2022.

[50] Anthony C Fisher. *Electrode dynamics*, volume 1. Oxford University Press Oxford, 1996.

[51] Christopher Brett and Ana Maria Oliveira Brett. *Electrochemistry: principles, methods, and applications*. Number 544.6 BRE. 1993.

[52] Noémie Elgrishi, Kelley J Rountree, Brian D McCarthy, Eric S Rountree, Thomas T Eisenhart, and Jillian L Dempsey. A practical beginner's guide to cyclic voltammetry. *Journal of chemical education*, 95(2):197–206, 2018.

[53] Wolfgang Schmickler and Elizabeth Santos. *Interfacial electrochemistry*. Springer Science & Business Media, 2010.

[54] Alfred Stett, Ulrich Egert, Elke Guenther, Frank Hofmann, Thomas Meyer, Wilfried Nisch, and Hugo Haemmerle. Biological application of microelectrode arrays in drug discovery and basic research. *Analytical and bioanalytical chemistry*, 377:486–495, 2003.

[55] R Mark Wightman. Probing cellular chemistry in biological systems with microelectrodes. *Science*, 311(5767):1570–1574, 2006.

[56] Encarnación Torralba, Eduardo Laborda, Angela Molina, Christine Cachet-Vivier, and Stéphane Bastide. Insights into the voltammetry of cavity microelectrodes filled with metal powders: The value of square wave voltammetry. *ChemElectroChem*, 8(4):735–744, 2021.

[57] Damien WM Arrigan. Nanoelectrodes, nanoelectrode arrays and their applications. *Analyst*, 129(12):1157–1165, 2004.

[58] László Péter. *Electrochemical Methods of Nanostructure Preparation*. Springer, 2021.

[59] Wenxin Huang, Jun Li, and Yunhe Xu. Nucleation/growth mechanisms and morphological evolution of porous mno2 coating deposited on graphite for supercapacitor. *Materials*, 10(10):1205, 2017.

[60] Benjamin Scharifker and Graham Hills. Theoretical and experimental studies of multiple nucleation. *Electrochimica acta*, 28(7):879–889, 1983.

[61] S Boudinar, N Benbrahim, B Benfedda, A Kadri, and L Hamadou. Electrochemical nucleation and optical characterization of highly oriented bi clusters on cu substrate. *Thin Solid Films*, 684:68–77, 2019.

[62] M Rezaei, M Ghorbani, and A Dolati. Electrochemical investigation of electrodeposited fe–pd alloy thin films. *Electrochimica Acta*, 56(1):483–490, 2010.

[63] Andrea Elizabeth Alvarez and Daniel Ricardo Salinas. Formation of cu/pd bimetallic crystals by electrochemical deposition. *Electrochimica acta*, 55(11):3714–3720, 2010.

[64] D Siopa and A Gomes. Nucleation and growth of zno nanorod arrays onto flexible substrates. *Journal of The Electrochemical Society*, 160(10):D476, 2013.

[65] M Jayakumar, KA Venkatesan, and TG Srinivasan. Electrochemical behavior of fission palladium in 1-butyl-3-methylimidazolium chloride. *Electrochimica acta*, 52(24):7121–7127, 2007.

[66] M Jayakumar, KA Venkatesan, TG Srinivasan, and PR Vasudeva Rao. Electrochemical behavior of ruthenium (iii), rhodium (iii) and palladium (ii) in 1-butyl-3-methylimidazolium chloride ionic liquid. *Electrochimica Acta*, 54(26):6747–6755, 2009.

[67] Young-Seon Ko and Young-Uk Kwon. Electrochemical deposition of platinum on fluorine-doped tin oxide: The nucleation mechanisms. *Electrochimica acta*, 55(24):7276–7281, 2010.

[68] Luc Heerman and Anthony Tarallo. Theory of the chronoamperometric transient for electrochemical nucleation with diffusion-controlled growth. *Journal of Electroanalytical chemistry*, 470(1):70–76, 1999.

[69] WW i Mullins. Metal surfaces: structure, energetics and kinetics. *American Society for Metals, Metals Park, Ohio*, pages 17–66, 1963.

[70] Gregory S Rohrer. Grain boundary energy anisotropy: a review. *Journal of materials science*, 46:5881–5895, 2011.

[71] Y-P Zhao, RM Gamache, G-C Wang, T-M Lu, G Palasantzas, and J Th M De Hosson. Effect of surface roughness on magnetic domain wall thickness, domain size, and coercivity. *Journal of Applied Physics*, 89(2):1325–1330, 2001.

[72] S Vilain, J Ebothe, and M Troyon. Surface roughness and composition effects on the magnetic properties of electrodeposited ni- co alloys. *Journal of magnetism and magnetic materials*, 157:274–275, 1996.

[73] W Schwarzacher. Kinetic roughening of electrodeposited films. *Journal of Physics: Condensed Matter*, 16(26):R859, 2004.

[74] Fereydoon Family and Tamas Vicsek. Scaling of the active zone in the eden process on percolation networks and the ballistic deposition model. *Journal of Physics A: Mathematical and General*, 18(2):L75, 1985.

[75] Y-L He, H-N Yang, T-M Lu, and GC Wang. Measurements of dynamic scaling from epitaxial growth front: Fe film on fe (001). *Physical review letters*, 69(26):3770, 1992.

[76] Georgios Palasantzas and J Krim. Scanning tunneling microscopy study of the thick film limit of kinetic roughening. *Physical review letters*, 73(26):3564, 1994.

[77] M Schroeder, M Siegert, DE Wolf, JD Shore, and M Plischke. Scaling of growing surfaces with large local slopes. *EPL (Europhysics Letters)*, 24(7):563, 1993.

[78] S Das Sarma, SV Ghaisas, and JM Kim. Kinetic super-roughening and anomalous dynamic scaling in nonequilibrium growth models. *Physical Review E*, 49(1):122, 1994.

[79] Antonio Brú, Juan Manuel Pastor, Isabel Fernaud, Isabel Brú, Sonia Melle, and Carolina Berenguer. Super-rough dynamics on tumor growth. *Physical Review Letters*, 81(18):4008, 1998.

[80] S Huo and W Schwarzacher. Anomalous scaling of the surface width during cu electrodeposition. *Physical review letters*, 86(2):256, 2001.

[81] Y-P Zhao, JB Fortin, G Bonvallet, G-C Wang, and T-M Lu. Kinetic roughening in polymer film growth by vapor deposition. *Physical review letters*, 85(15):3229, 2000.

[82] Lihu Liu and W Schwarzacher. Slope analysis and scaling analysis of electrodeposited thin films. *Electrochemistry communications*, 29:52–54, 2013.

[83] Ewen O. Blair. *The Optimisation and Characterisation of Durable Microelectrodes for Electroanalysis in Molten Salt*. Phd thesis, The University of Edinburgh, Edinburgh, Scotland, November 2017.

[84] Martin C Henstridge and Richard G Compton. Mass transport to micro-and nanoelectrodes and their arrays: a review. *The Chemical Record*, 12(1):63–71, 2012.

[85] Oliver D Payton, Loren Picco, and Thomas Bligh Scott. High-speed atomic force microscopy for materials science. *International Materials Reviews*, 61(8):473–494, 2016.

[86] FS Russell-Pavier, Loren Picco, JCC Day, NR Shatil, A Yacoot, and OD Payton. 'hi-fi afm': high-speed contact mode atomic force microscopy with optical pickups. *Measurement Science and Technology*, 29(10):105902, 2018.

[87] Georg Schitter, Karl J Astrom, Barry E DeMartini, Philipp J Thurner, Kimberly L Turner, and Paul K Hansma. Design and modeling of a high-speed afm-scanner. *IEEE Transactions on Control Systems Technology*, 15(5):906–915, 2007.

[88] Stacy Moore. *A Study of Stress Corrosion Cracking by High-Speed Atomic Force Microscopy*. Phd thesis, University of Bristol, Bristol, UK, March 2021.

[89] Covalent metrology services. The 3 sem signals you need to know to optimize your sem analysis, 2021. [Online; accessed 05-june-2023].

[90] Antonis Nanakoudis. Sem: Types of electrons and the information they provide, 2019. [Online; accessed 05-June-2023].

[91] Ebsd: Electron backscatter diffraction. `https://www.ebsd.com/`. Accessed: 2022-12-16.

[92] An introduction to ebsd. `https://www.azom.com/article.aspx?ArticleID=11770`. Accessed: 2022-12-16.

[93] Yuriy I Yanson and Marcel J Rost. Structural accelerating effect of chloride on copper electrodeposition. *Angewandte Chemie International Edition*, 52(9):2454–2458, 2013.

[94] MJ Rost. In situ real-time observation of thin film deposition: roughening, zeno effect, grain boundary crossing barrier, and steering. *Physical review letters*, 99(26):266101, 2007.

[95] Jayme S Keist, Christine A Orme, Paul K Wright, and James W Evans. An in situ afm study of the evolution of surface roughness for zinc electrodeposition within an imidazolium based ionic liquid electrolyte. *Electrochimica Acta*, 152:161–171, 2015.

[96] Taiki Yoshioka, Hisayoshi Matsushima, and Mikito Ueda. In situ observation of cu electrodeposition and dissolution on au (100) by high-speed atomic force microscopy. *Electrochemistry Communications*, 92:29–32, 2018.

[97] Taiki Yoshioka, Hisayoshi Matsushima, and Mikito Ueda. In situ observation of cu electrodeposition and dissolution behavior on au (111) by high speed afm. *Electrochimica Acta*, 302:422–427, 2019.

[98] Aswathi Koorikkat, Oliver Payton, Loren Picco, and Walther Schwarzacher. Imaging the surface of a polycrystalline electrodeposited cu film in real time using in situ high-speed afm. *Journal of the Electrochemical Society*, 167(16):162510, 2020.

[99] Robert J Forster. Microelectrodes: new dimensions in electrochemistry. *Chemical Society Reviews*, 23(4):289–297, 1994.

[100] AllenJ Bard. *Standard potentials in aqueous solution*. Routledge, 2017.

[101] TI Quickenden and Qingzhong Xu. Toward a reliable value for the diffusion coefficient of cupric ion in aqueous solution. *Journal of the Electrochemical Society*, 143(4):1248, 1996.

[102] Rei Esaki, Yohei Yasuda, Norito Kotani, Hisayoshi Matsushima, and Mikito Ueda. High speed atomic force microscope observation of polyethylene glycol adsorption on au (100). *Journal of The Electrochemical Society*, 169(8):082512, 2022.

[103] Klaus J Vetter. *Electrochemical kinetics: theoretical aspects*. Elsevier, 2013.

[104] A Damjanovic. On the mechanism of metal electrocrystallization. *Plating*, 52:1017–1026, 1965.

[105] John O'M Bockris and Amulya KN Reddy. *Modern electrochemistry 2B: electrodics in chemistry, engineering, biology and environmental science*, volume 2. Springer Science & Business Media, 1998.

[106] N Pangarov and V Velinov. Preferred orientation and morphology of twinned crystals by electrocrystallization of silver. *Electrochimica Acta*, 13(7):1641–1646, 1968.

[107] Chun-Cheng Lin and Chi-Chang Hu. The ultrahigh-rate growth of nanotwinned copper induced by thiol organic additives. *Journal of The Electrochemical Society*, 167(8):082505, 2020.

[108] John R LaGraff and Andrew A Gewirth. Nanometer-scale mechanism for the constructive modification of cu single crystals and alkanethiol passivated au (111) with an atomic force microscope. *The Journal of Physical Chemistry*, 99(24):10009–10018, 1995.

[109] John R LaGraff and Andrew A Gewirth. Enhanced electrochemical deposition with an atomic force microscope. *The Journal of Physical Chemistry*, 98(44):11246–11250, 1994.

[110] Zhiming Li, Konda Gokuldoss Pradeep, Yun Deng, Dierk Raabe, and Cemal Cem Tasan. Metastable high-entropy dual-phase alloys overcome the strength–ductility trade-off. *Nature*, 534(7606):227–230, 2016.

[111] YT Zhu, XZ Liao, and XL Wu. Deformation twinning in nanocrystalline materials. *Progress in Materials Science*, 57(1):1–62, 2012.

[112] Prateek Uttam, Vanish Kumar, Ki-Hun Kim, and Akash Deep. Nanotwinning: Generation, properties, and application. *Materials & Design*, 192:108752, 2020.

[113] Ke Lu, Lei Lu, and S Suresh. Strengthening materials by engineering coherent internal boundaries at the nanoscale. *science*, 324(5925):349–352, 2009.

[114] L Lu, R Schwaiger, ZW Shan, M Dao, K Lu, and S Suresh. Nano-sized twins induce high rate sensitivity of flow stress in pure copper. *Acta materialia*, 53(7):2169–2179, 2005.

[115] Lei Lu, Xianhua Chen, Xiaoxu Huang, and K Lu. Revealing the maximum strength in nanotwinned copper. *Science*, 323(5914):607–610, 2009.

[116] Lei Lu, Yongfeng Shen, Xianhua Chen, Lihua Qian, and Ke Lu. Ultrahigh strength and high electrical conductivity in copper. *Science*, 304(5669):422–426, 2004.

[117] AP Sutton and RW Balluffi. Interfaces in crystalline materials (clarendon, oxford). 1995.

[118] Kuan-Chia Chen, Wen-Wei Wu, Chien-Neng Liao, Lih-Juann Chen, and King-Ning Tu. Observation of atomic diffusion at twin-modified grain boundaries in copper. *Science*, 321(5892):1066–1069, 2008.

[119] Hsiang-Yao Hsiao, Chien-Min Liu, Han-wen Lin, Tao-Chi Liu, Chia-Ling Lu, Yi-Sa Huang, Chih Chen, and King-Ning Tu. Unidirectional growth of microbumps on (111)-oriented and nanotwinned copper. *Science*, 336(6084):1007–1010, 2012.

[120] Madoka Hasegawa, Maxime Mieszala, Yucheng Zhang, Rolf Erni, Johann Michler, and Laetitia Philippe. Orientation-controlled nanotwinned copper prepared by electrodeposition. *Electrochimica Acta*, 178:458–467, 2015.

[121] MS Chandrasekar and Malathy Pushpavanam. Pulse and pulse reverse plating—conceptual, advantages and applications. *Electrochimica Acta*, 53(8):3313–3322, 2008.

[122] N Ibl. Some theoretical aspects of pulse electrolysis. *Surface Technology*, 10(2):81–104, 1980.

[123] S Roy. Mass transfer considerations during pulse plating. *Transactions of the IMF*, 86(2):87–91, 2008.

[124] S Yoshimura, S Chida, E Sato, and N Kubota. Pulsed current electrodeposition of palladium. *Metal finishing*, 84(10):39–42, 1986.

[125] Y Fukumoto, Y Kawashima, K Handa, and Y Hayashi. Pulsed current electrodeposition of palladium. *Metal finishing*, 82(9):77–80, 1984.

[126] J Cl Puippe et al. The morphology of pulse-plated deposits. 1980.

[127] Trevor Pearson and Keith Dennis. Effect of pulsed current on the properties of electrodeposited chromium. *Plating and surface finishing*, 76(11):64–69, 1989.

[128] M Jose and NV Parthasaradhy. Investigations on cr plating baths(conventional, high sulphate and srhs baths). *Galvanotechnik*, 63(6):523–533.

[129] T Pearson and JK Dennis. Facts and fiction about pulse plating. *Transactions of the IMF*, 69(3):75–79, 1991.

[130] Watershed segmentation. `https://scikit-image.org/docs/stable/auto_examples/segmentation/plot_watershed.html`. Accessed: 2022-12-16.

[131] Iouri M Soukhov and M Kelbert. Probability and statistics by example: Volume i. basic probability and statistics. 2005.

[132] Guan-Tai Lui, Delphic Chen, and Jui-Chao Kuo. Ebsd characterization of twinned copper using pulsed electrodeposition. *Journal of Physics D: Applied Physics*, 42(21):215410, 2009.

[133] Ziming Xue, Zengwei Zhu, Xiaofei Zhan, Xiaofei Xu, Chunjian Shen, Anxin Li, and Di Zhu. Manipulating the microstructure of cu from direct current electrodeposition without additives to overcome the strength-ductility trade-off. *Materials Science and Engineering: A*, 849:143499, 2022.

[134] Milan Paunovic and Mordechay Schlesinger. *Fundamentals of electrochemical deposition*. john wiley & sons, 2006.

[135] C Savall, A Godon, Jordi Creus, and X Feaugas. Influence of deposition parameters on microstructure and contamination of electrodeposited nickel coatings from additive-free sulphamate bath. *Surface and Coatings Technology*, 206(21):4394–4402, 2012.

[136] Ge Yi and Walther Schwarzacher. Single crystal superconductor nanowires by electrodeposition. *Applied physics letters*, 74(12):1746–1748, 1999.

[137] Jean-Claude Puippe and Steiger Galvanotechnique SA. Qualitative approach to pulse plating. In *Theory and Practice of Pulse Plating*. American Electroplaters' Society Orlando, FL, USA, 1986.

[138] K Kremmer, O Yezerska, G Schreiber, M Masimov, V Klemm, M Schneider, and D Rafaja. Interplay between the deposition mode and microstructure in electrochemically deposited cu thin films. *Thin Solid Films*, 515(17):6698–6706, 2007.

[139] Sead Canovic, Torbjörn Jonsson, and Mats Halvarsson. Grain contrast imaging in fib and sem. In *Journal of Physics: Conference Series*, volume 126, page 012054. IOP Publishing, 2008.

[140] David Cohen. Precalculus: A problems-oriented approach , cengage learning. Technical report, ISBN 978-0-534-40212-9, 2004.

[141] S Ahmed, TT Ahmed, M O'Grady, S Nakahara, and DN Buckley. Investigation of stress and morphology in electrodeposited copper nanofilms by cantilever beam method and in situ electrochemical atomic force microscopy. *Journal of Applied Physics*, 103(7):073506, 2008.

[142] OE Kongstein, U Bertocci, and GR Stafford. In situ stress measurements during copper electrodeposition on (111)-textured au. *Journal of the Electrochemical Society*, 152(3):C116, 2005.

[143] Di Xu, Wei Lek Kwan, Kai Chen, Xi Zhang, Vidvuds Ozoliņš, and King-Ning Tu. Nanotwin formation in copper thin films by stress/strain relaxation in pulse electrodeposition. *Applied Physics Letters*, 91(25):254105, 2007.

[144] Di Xu, Vinay Sriram, Vidvuds Ozolins, Jenn-Ming Yang, King-Ning Tu, Gery R Stafford, and Carlos Beauchamp. In situ measurements of stress evolution for nanotwin formation during pulse electrodeposition of copper. *Journal of Applied Physics*, 105(2):023521, 2009.

[145] Derek Pletcher, R Greff, R Peat, LM Peter, and J Robinson. *Instrumental methods in electrochemistry*. Elsevier, 2001.

[146] W-K_ Burton, N Cabrera, and FC Frank. The growth of crystals and the equilibrium structure of their surfaces. *Philosophical Transactions of the Royal Society of London. Series A, Mathematical and Physical Sciences*, 243(866):299–358, 1951.

[147] Joachim Krug. Spiral growth, two-dimensional nucleation, and the ehrlich-schwoebel effect. *arXiv preprint arXiv:0709.2049*, 2007.

[148] Xiaofei Zhan, Jian Lian, Hongjun Li, Xiubin Wang, Jiaan Zhou, Khuong Trieu, and Xinping Zhang. Preparation of highly (111) textured nanotwinned copper by medium-frequency pulsed electrodeposition in an additive-free electrolyte. *Electrochimica Acta*, 365:137391, 2021.

[149] Liang Chen, Bilu Liu, Ahmad N Abbas, Yuqiang Ma, Xin Fang, Yihang Liu, and Chongwu Zhou. Screw-dislocation-driven growth of two-dimensional few-layer and pyramid-like wse2 by sulfur-assisted chemical vapor deposition. *Acs Nano*, 8(11):11543–11551, 2014.

[150] Thomas P Moffat, JE Bonevich, WH Huber, A Stanishevsky, DR Kelly, GR Stafford, and D Josell. Superconformal electrodeposition of copper in 500–90 nm features. *Journal of The Electrochemical Society*, 147(12):4524, 2000.

[151] A Godon, Jordi Creus, S Cohendoz, E Conforto, X Feaugas, P Girault, and C Savall. Effects of grain orientation on the hall–petch relationship in electrodeposited nickel with nanocrystalline grains. *Scripta Materialia*, 62(6):403, 2010.

[152] S Mehrizi, M Heydarzadeh Sohi, and SA Seyyed Ebrahimi. Study of microstructure and magnetic properties of electrodeposited nanocrystalline cofenicu thin films. *Surface and Coatings Technology*, 205(20):4757–4763, 2011.

[153] Rajendra M Patrikar, Chong Yi Dong, and Wenjun Zhuang. Modelling interconnects with surface roughness. *Microelectronics Journal*, 33(11):929–934, 2002.

[154] Haebum Lee, S Simon Wong, and Sergey D Lopatin. Correlation of stress and texture evolution during self-and thermal annealing of electroplated cu films. *Journal of Applied Physics*, 93(7):3796–3804, 2003.

[155] F Bachmann, Ralf Hielscher, and Helmut Schaeben. Texture analysis with mtex–free and open source software toolbox. In *Solid state phenomena*, volume 160, pages 63–68. Trans Tech Publ, 2010.

[156] Panayotis C Andricacos, Cyprian Uzoh, John O Dukovic, Jean Horkans, and Hariklia Deligianni. Damascene copper electroplating for chip interconnections. *IBM Journal of Research and Development*, 42(5):567–574, 1998.

[157] Olaf M Magnussen. Ordered anion adlayers on metal electrode surfaces. *Chemical reviews*, 102(3):679–726, 2002.

[158] TP Moffat. Stm study of the influence of adsorption on step dynamics. *MRS Online Proceedings Library (OPL)*, 451, 1996.

[159] W Shao, G Pattanaik, and G Zangari. Influence of chloride anions on the mechanism of copper electrodeposition from acidic sulfate electrolytes. *Journal of The Electrochemical Society*, 154(4):D201, 2007.

[160] Karl Doblhofer, Sabine Wasle, David M Soares, Konrad G Weil, Gisela Weinberg, and Gerhard Ertl. The influence of halide ions on the kinetics of electrochemical copper (ii) reduction. *Zeitschrift für Physikalische Chemie*, 217(5):479–492, 2003.

[161] David M Soares, Sabine Wasle, Konrad G Weil, and Karl Doblhofer. Copper ion reduction catalyzed by chloride ions. *Journal of Electroanalytical Chemistry*, 532(1-2):353–358, 2002.

[162] N Vasiljevic, M Wood, PJ Heard, and W Schwarzacher. The influence of specific anion adsorption on the surface roughness of electrodeposited polycrystalline cu films. *Journal of the Electrochemical Society*, 157(4):D193, 2010.

[163] Hong Zhao, Jinho Chang, Aliaksei Boika, and Allen J Bard. Electrochemistry of high concentration copper chloride complexes. *Analytical chemistry*, 85(16):7696–7703, 2013.

[164] Matthew M Nowell, Ronald A Witt, and Brian W True. Ebsd sample preparation: techniques, tips, and tricks. *Microscopy Today*, 13(4):44–49, 2005.

[165] Tsung-Cheng Chan, Yu-Lun Chueh, and Chien-Neng Liao. Manipulating the crystallographic texture of nanotwinned cu films by electrodeposition. *Crystal growth & design*, 11(11):4970–4974, 2011.

[166] Rolf Weil. The structures of electrodeposits and the properties that depend on them. *Annual Review of Materials Science*, 19(1):165–182, 1989.

[167] Irene J Beyerlein, Xinghang Zhang, Amit Misra, et al. Growth twins and deformation twins in metals. *Annu. Rev. Mater. Res*, 44(1):329–363, 2014.